การเตรียมชั้นไทเทเนียมไดออกไซด์สำหรับเซลล์แสงอาทิตย์ชนิดไวสีย้อม

นายธนชัย พลเคน

วิทยานิพนธ์นี้เป็นส่วนหนึ่งของการศึกษาตามหลักสูตรปริญญาวิทยาศาสตรมหาบัณฑิต
สาขาวิชาฟิสิกส์ ภาควิชาฟิสิกส์
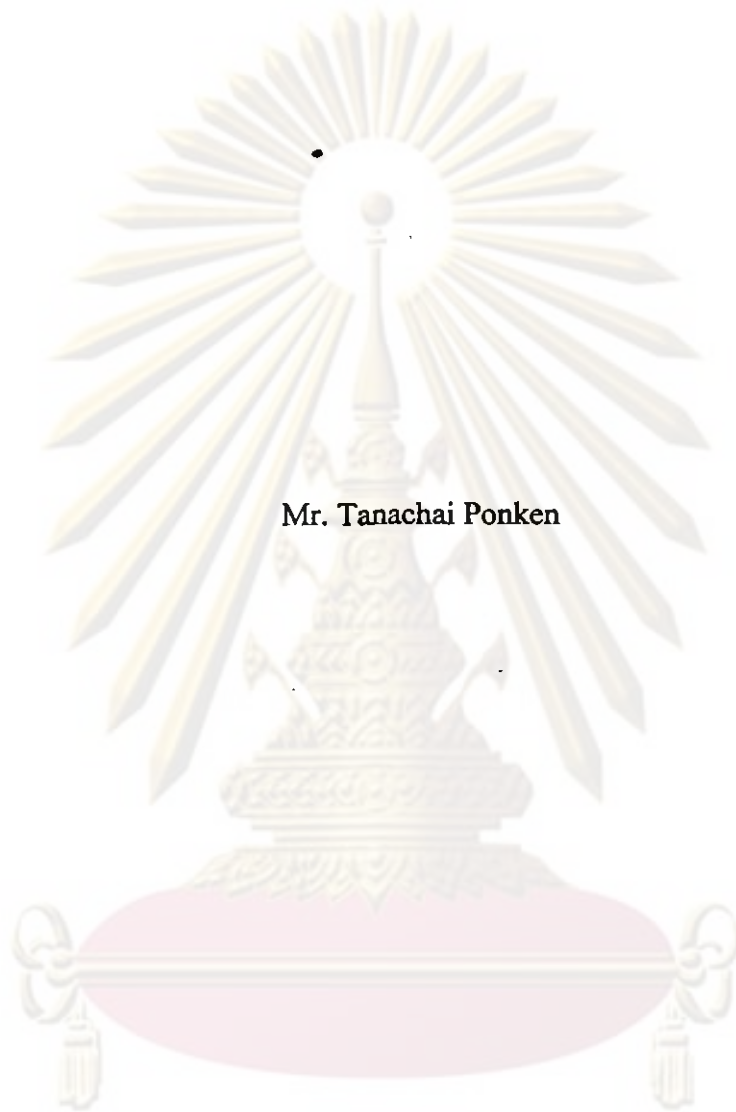คณะวิทยาศาสตร์ จุฬาลงกรณ์มหาวิทยาลัย
ปีการศึกษา 2552

PREPARATION OF TiO2 LAYER FOR DYE-SENSITIZED SOLAR CELLS

Mr. Tanachai Ponken

A Thesis Submitted in Partial Fulfillment of the Requirements
for the Degree of Master of Science Program in Physics
Department of Physics
Faculty of Science
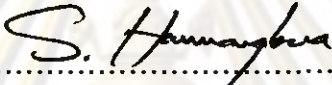Chulalongkorn University
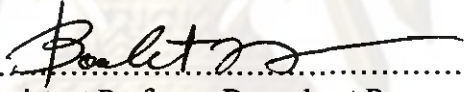Academic Year 2009
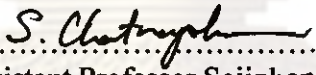Copyright of Chulalongkorn University

521708

Thesis Title	Preparation of TiO$_2$ Layer for Dye-sensitized Solar Cells
By	Mr. Tanachai Ponken
Field of Study	Physics
Thesis Advisor	Assistant Professor Sojiphong Chatraphorn, Ph.D.
Thesis Co-advisor	Chanwit Chityuttakan, Ph.D.

Accepted by the Faculty Science, Chulalongkorn University in Partial Fulfillment of the Requirements for the Master's Degree

....Dean of the Faculty of Science

(Professor Supot Hannongbua , Dr.rer.net.)

THESIS COMMITTEE

.... Chairman
(Assistant Professor Boonchoat Paosawatyanyong, Ph.D.)

.... Thesis Advisor
(Assistant Professor Sojiphong Chatraphorn, Ph.D.)

.... Thesis Co-advisor
(Chanwit Chityuttakan, Ph.D.)

.... Examiner
(Assistant Professor Nakorn Phaisangittisakul , Ph.D.)

.... External Examiner
(Panita Chinvetkitvanich , Ph.D.)

ธนชัย พลเคน : การเตรียมชั้นไทเทเนียมไดออกไซด์สำหรับเซลล์แสงอาทิตย์ชนิดไวสีย้อม
(PREPARATION OF TiO2 FOR DYE-SENSITIZED
SOLAR CELLS) อ.ที่ปรึกษาวิทยานิพนธ์หลัก: ผศ.ดร.โศจิพงศ์ ฉัตราภรณ์, อ.ที่
ปรึกษาวิทยานิพนธ์ร่วม: ดร. ชาญวิทย์ จิตยุทธการ, 94 หน้า.

เงื่อนไขที่เหมาะสมสำหรับการปลูกชั้นไทเทเนียมไดออกไซด์ด้วยวิธีการพ่นเคลือบถูก
ศึกษาสำหรับการประยุกต์ของเซลล์แสงอาทิตย์ชนิดไวสีย้อม ชั้นไทเทเนียมไดออกไซด์ถูกเตรียม
ด้วยวิธีพ่นเคลือบบนแผ่นรองรับซิงค์ออกไซด์เจืออะลูมินัมบนกระจกขนาด 3 x 3 ตาราง
เซนติเมตร สารแขวนลอยไทเทเนียมไดออกไซด์ถูกเตรียมโดยการบดผงไทเทเนียมไดออกไซด์
ในอะซิทิวอะซิโตและน้ำปราศจากไอออน สารแขวนลอยไทเทเนียมไดออกไซด์ถูกพ่นลงบนแผ่น
รองรับซิงค์ออกไซด์เจืออะลูมินัมบนกระจกซึ่งมีส่วนประกอบชั้นยับยั้งไทเทเนียมไดออกไซด์บาง
มาก แผ่นรองรับในงานนี้ถูกหมุนด้วยความเร็วรอบ 1800 รอบต่อนาที ก่อนทำการพ่นที่
อุณหภูมิห้อง ตัวอย่างไทเทเนียมไดออกไซด์ที่ปลูกถูกเผาที่ 450 องศาเซลเซียส ใน 1 ชั่วโมง ใน
บรรยากาศ เครื่องมือในการวิเคราะห์เช่น เทคนิคการเลี้ยวเบนของรังสีเอกซ์ เครื่องตรวจวัดการ
ดูดกลืนแสง กล้องจุลทรรศน์แบบใช้แรงของอะตอม ถูกใช้ในการตรวจสอบการเคลือบไทเทเนียม
ไดออกไซด์สำหรับสมบัติเชิงโครงสร้าง เชิงแสง และพื้นผิวหน้าตามลำดับ ขั้วไฟฟ้าตรงข้ามสำหรับ
เซลล์แสงอาทิตย์ชนิดไวสีย้อมในงานนี้ถูกเตรียมจากการเคลือบเซลล์ไฟฟ้าเคมีของแพลทินัมบน
แผ่นรองรับซิงค์ออกไซด์เจืออะลูมินัมบนกระจก สารสีย้อม Ruthenium 535 bis-TBA ถูกใช้เป็น
สารไวแสง ประสิทธิภาพการเปลี่ยนแสงโฟตอนเป็นกระแสของเซลล์ถูกวิเคราะห์ภายใต้รังสี
มาตรฐาน AM 1.5 ความเข้มแสงเท่ากับ 100 มิลลิวัตต์ต่อตารางเซนติเมตร ประสิทธิภาพสูงสุด
ของเซลล์แสงอาทิตย์ชนิดไวสีย้อมถูกเตรียมมาจาก ชั้นป้องกันการลัดวงจรไทเทเนียมไดออกไซด์
หนาประมาณ 25 นาโนเมตร ความหนาของชั้นไทเทเนียมไดออกไซด์ประมาณ 13 ไมโครเมตร
และไทเทเนียมไดออกไซด์ชนิด Degussa P25 จะมีค่า ความหนาแน่นของกระแส (J_{sc}) เท่ากับ
0.368 มิลลิแอมแปร์ต่อตารางเซนติเมตร ความต่างศักย์ (V_{oc}) ประมาณ 730 มิลลิโวลต์ ค่าฟิล
แฟคเตอร์ (FF) 0.59 และประสิทธิภาพของเซลล์ 0.158%

ภาควิชา พิสิกส์	ลายมือชื่อนิสิต	พลเคน
สาขาวิชา พิสิกส์	ลายมือชื่อ อ.ที่ปรึกษาวิทยานิพนธ์หลัก	
ปีการศึกษา 2552	ลายมือชื่อ อ.ที่ปรึกษาวิทยานิพนธ์ร่วม	

4972312623   : MAJOR PHYSICS

KEYWORDS: SPRAY COATING TiO2 LAYER / TiO$_2$-BLOCKING-LAYER / DYE-SENSITIZED SOLAR CELLS

TANACHAI PONKEN: PREPARATION OF TITANIUM DIOXIDE LAYER FOR DYE-SENSITIZED SOLAR CELLS. THESIS ADVISOR: ASST.PROF. SOJIPHONG CHATRAPHORN, Ph.D., THESIS CO-ADVISOR: CHANWIT CHITYUTTAKAN, Ph.D., 94 pp.

The suitable conditions for the formation of TiO$_2$ layer by spray coating technique were investigated for the application of dye-sensitized solar cell. TiO$_2$ layers were prepared by spray coating technique on 3x3 cm^2 ZnO(Al)/SLG substrates. The TiO$_2$ colloidal solution was prepared from ground TiO$_2$ powder in acetylacetone and deionized water. The TiO$_2$ colloidal solution was sprayed on ZnO(Al)/SLG substrate consisting of a very thin sputtered TiO$_2$ blocking layer. The substrates used in this work were spun at 1800 rpm prior to spraying at room temperature. The as-grown TiO$_2$ samples were annealed at 450°C for 1 hour in atmosphere. The characterization tools such as XRD, UV-VIS spectrometer and AFM were used to verify the deposited TiO$_2$ films for its structural, optical and surface properties, respectively. The counter electrode for the dye-sensitized solar cells in this work was prepared from the electrochemical deposition of Pt on the ZnO(Al)/SLG substrate. The ruthenium 535 bis-TBA dye was used as the sensitizer. The photo-to-current conversion efficiency of the cells was characterized under standard AM 1.5 radiation (100 mW/cm^2). The highest efficiency of DSSC was prepared from the TiO$_2$-blocking-layer (thick ~25 nm), thickness of TiO$_2$ layer ~13 μm and Degussa TiO$_2$ P25 which value short circuit current density (J_{sc}) of approximately 0.368 mA/cm^2, open-circuit voltage (V_{oc}) of approximately 730 mV, Fill Factor (FF) 0.59 and efficiency (η) of approximately 0.158%.

Department : Physics   Student's Signature _Tanachai Ponken_

Field of Study : Physics   Advisor's Signature _S. Chatyph_

Academic Year : 2009   Co-Advisor's Signature _Chanwit Chityuttakan_

Acknowledgements

Contents

List of Tables

Page

List of Figures

List of Symbols and Abbreviations

Symbols

α	Absorption coefficient
e_o	Elementary charge
E	Energy
$\vec{E}$	Electrical field
E_C	Conduction band energy
E_F	Fermi energy
E_F^n	The quasi-Fermi of electron
E_g	Forbidden energy gap
$E_{\mathbf{Re}dox}$	Redox energy
$E_{\mathbf{Re}dox}^o$	Standard redox potential
E_V	Valence band energy
$f(E)$	Fermi-Dirac function
FF	Fill factor
h	Planck's constant
$\hbar$	Planck's constant/2π
I	Electrical current
I^-	Iodide ion
I_3^-	Tri-iodide ion

I_L	Light-generated current
I_M	Maximum current (of solar cells)
I_o	Initial current
I_{SC}	Short circuit current
$\vec{J}$	Current density
$J_{\mathbf{max}}$	Maximum current density
J_{SC}	Short circuit current density
k_B	Boltzmann's constant
k_{inj}	The rate constant for electron injection
m	Number of transferred electron
m_e^*	Electron effective mass
m_h^*	Hole effective mass
n	Electron density
n_o	Equilibrium electron or hole density
n_i	Intrinsic electron or hole density
N	Charge carrier density
N_A	Acceptor density
N_D	Donor density
N_C	Conduction band density of state function
N_e	Electron density

[N(E)]	Number of states per unit volume
N_p	Hole density
N_V	Valence band density of state function
Ox	Oxidized species
$[Ox]$	Oxidized species concentration
P_{in}	Incident power
P_M	Maximum power output (of solar cells)
p_o	Equilibrium hole density
q	Charge on the electron
R	Reflectance, Reflectivity, Gas constant
R_S	Series resistance
R_{SH}	Shunt resistance
S^o	Ground state
S^*	Excited state
S^+	Oxidized state
T	Transmittance, Transmissivity, Absolute temperature
U	Electrode potential of the semiconductor
U_{fb}	Flat-band potential
V	Electrical voltage
V_B	Amount of band bending in the depletion layer
V_H	Helmholtz layer potential drop

V_{max}	Maximum voltage
V_{OC}	Open circuit voltage
w	Depletion layer width
x	Stoichiometric coefficient of oxidation reaction
z	Number of charge
σ	Electrical conductivity
μ_e	Electron mobility
μ_p	Hole mobility
ε	Dielectric constant
ε_o	Permittivity of free space
ϕ_{El}	Work function of electrolyte
ϕ_{inj}	Quantum yield of charge injection
ϕ_{SC}	Work function of semiconductor
χ	Electron affinity
η_E	Electrochemical potential
μ	Chemical potential
φ	Electrical potential
υ	Light frequency
η	Solar cell conversion efficiency
Γ	Number of modes of sensitizer per square centimeter
τ	Excited state lifetime

Ω	Ohm
λ	Wavelength
β	Full width at half maximum
θ	X-ray diffraction angle
Z_{rms}	Root-mean-square roughness

Abbreviations

AM 1.5	Standard terrestrial solar spectrum "Air Mass 1.5"
AFM	Atomic force microscopy
BKD	Backscatter Kikuchi diffraction
DI	De-ionized water
DOS	Density of state
DSSC	Dye-sensitized solar cell
E	Energy
EBSD	Electron backscatter diffraction
Eff.	Efficiency
EVA	Ethylene-viny acetate
FWHM	Full width at half maximum
HOMO	Highest occupied molecular orbital
I-V	Current versus voltage [curve]
IPCE	The incident photo-to-current conversion efficiency
LHE	Light harvesting efficiency

LUMO	Lowest unoccupied molecular orbital
NIR	Near infrared
PEC	Photo-electrochemical
PV	Photovoltaic
PVA	Polyvinylacetate
Red	Reduced species
RF	Radio frequency (for sputtering process)
RPM, rpm	Rotate per minutes
S	Sensitizer
sccm	Standard cubic centimeters per minutes
SCE	Standard calomel electrode
SEM	Scanning electron microscopy
SLG	Soda-lime glass
TBA	Tetra-butylammonium
TCO	Transparent conducting oxide
USA	United State of America
W	Watt
XRD	X-ray diffraction

CHAPTER I

INTRODUCTION

The many problems facing mankind, those concerning the availability and distribution of energy will ultimately be the most important. As fossil fuel becomes depleted, people will turn more and more to alternative sources and eventually depend on energy technologies based on nuclear fusion, nuclear fission and solar energy. Nuclear energy also relies on finite resources and involves significant problems. The worldwide quest for clean and renewable energy source has encouraged large research activities and developments in the area of photovoltaic applications, and also organic based solar cells. A dye-sensitized solar cell (DSSC) is the latest revolution in solar energy conversion device after 40 years of the invention of silicon solar cell [1]. The working mechanisms of DSSC are based on photo-electrochemical reactions. Specific advantages of the DSSC are the easiness in fabrication, low-cost, more environmental friendly and photo-voltage is significantly less sensitive to light intensity variation than that of conventional solar cells. Typically, a dye-sensitized solar cell (DSSC) is composed of two surfaces of transparent conductor, one of which a few micrometers thick film of wide band gap semiconductor has been deposited as a self-connected network of nano-sized particles, with a network of similarly or larger-sized self-connected pores in between the particles. The semiconductor that is most widely used is the anatase form of TiO_2. Onto the semiconductor dye molecules are chemisorbed, forming closed to a monolayer. This dye-semiconductor assembly is in contact with a redox electrolyte that serves to close the electrical circuit with the second transparent conducting electrode (counter electrode). A catalyst is deposited on the counter electrode to facilitate the redox reaction that has to occur on it in order to close the electrical circuit. The TiO_2 nanocrystalline is a wide band gap semiconductor therefore the most photon energies pass through the film and are absorbed by dye. Thus, photogenerated carriers and transport are well separated. Because of this spatial and material (phase) separation, the chances of recombination can be drastically reduced. Electrons can spend long periods of time in the semiconductor film without

recombination. This is somewhat simplistic in the sense that the electrons can be re-injected into the electrolyte and recombined in this way, however, also that pathway involves two phases and is much less probable than direct electron-hole recombination. Oxide semiconducting materials have good stability under irradiation in solution. However, stable oxide semiconductors cannot absorb visible light because they have relatively wide band gap. Sensitization of wide band gap oxide semiconductor materials, such as TiO_2, ZnO and SnO_2, with photosensitizers, such as organic dyes, that can absorb visible light has been extensively studied in relation to the development of photography technology since the late nineteenth century. In the sensitization process, photosensitizers adsorbed onto the semiconductor surface absorb visible light and excited electrons are injected into the conduction band of the semiconductor electrodes.

Gerischer and Tributsch studied a ZnO electrode sensitized by organic dyes including rose bengal, fluorescein and rhodamine B [2]. In early studies, however, singlecrystal and polycrystal materials, which cannot adsorb a large amount of dye, were used for the photoelectrode, which resulted in low light-harvesting efficiency (LHE) and, consequently, low photon-to-current conversion efficiencies. Additionally, the organic dyes that were used had a narrow absorption range in visible light, which also contributed to low solar cell performance, researchers used two approaches: developing photoelectrodes with larger surface areas that could adsorb larger amount of dye and synthesizing dyes with broader absorption ranges. Significant improvements in the performance of a dye-sensitized solar cell (DSSC, or Grätzel cell) have been mainly due to the development of high-performance nanoporous TiO_2 thin film electrodes that have a large surface area capable of new Ru-complex photosensitizers capable of absorbing in the wide visible and near-IR region from 400 to 800 or 900 nm.

At present, various wide band gap semiconductor materials are used for fabricating a working electrode such as TiO_2, ZnO, SnO_2 and Nb_2O_5. Titanium dioxide (TiO_2) quickly becomes the semiconductor of choice for the photoelectrode on account of its many advantages for sensitized photochemistry and photoelectron chemistry: it is a low-cost, widely available, non-toxic and biocompatible material, and even used in healthcare products as well as industrial applications which only

TiO_2 can achieve the highest efficiency. There are various techniques in preparing the TiO_2 electrode such as sputtering, thermal evaporation, doctor blading, screen printing, electrophoretic and electrospining. Recently, DSSC reported by O'Regan and Grätzel have been an intensive research topic since the discovery in 1991 [3]. Among different types of DSSCs, liquid type electrolyte base on iodide/tri-iodide redox (I^-/I_3^-) redox couple system is used in high performance DSSCs which shows efficiency higher than 10% [4]. They achieved a solar energy efficiency (η) of 7.1% under AM 1.5 irradiation using a DSSC consisting of a nanocrystalline TiO_2 thin film electrode by screen-printing technique [5,6]. Therefore, alternative embodiment of the DSSC concept is the replacement of the redox electrolyte with a solid-state hole conductor, which may be either inorganic or organic, thereby avoiding the use of a redox electrolyte. Such solid-state sensitized heterojunctions can be regarded as functional intermediate between redox electrolyte and semiconductor. The DSSCs using liquid type electrolyte do not have sufficient stability for long term use due to the leakage of electrolyte, evaporation of solvent and sublimation of iodine. Several attempts have been made to replace the liquid electrolyte by a p-type semiconductors or organic hole transport materials. However, the conversion efficiency of these devices was relatively low particularly under high light irradiance due to high frequency of charge recombination from TiO_2 to hole transport materials or poor electronic contact between dye molecules and the hole transport materials accompanied by incomplete penetration of solid hole transport materials in the void of the nanoporous TiO_2 electrodes.

Until the announcement, M. Grätzel and coworkers at the Swiss Federal Institute of Technology (EPFL) have made a breakthrough in preparing efficient dye-sensitized cells. High surface area TiO_2 semiconductor electrode, with a microporous morphology, have been sensitized with different Ru(bpy)-complexes which is using in high performance DSSCs which shows efficiency higher than 10% (Grätzel, 2001) under AM 1.5 irradiation using a DSSC consisting of a nanocrystalline TiO_2 thin film electrode by doctor blading technique having a nanoporous structure with large surface area.

Presently, research in Thailand has been made by Dr. Wirat Jarernboon at Khon Kean University (KKU). There are various techniques in preparing the TiO_2

electrode such as TiO$_2$ nanofibers from electrospining technique, nanocrystalline-TiO$_2$ powders using biosynthetic simple method, nanocrystalline TiO$_2$ paste and nanoporous-TiO$_2$ films using screen printing technique. For the screen printing technique, the highest efficiency of the liquid type DSSC of about 6.67% was observed at the transparent layer thickness was 20.2 μm, N719 dye. They achieved a solar energy efficiency (η) of 5 to 6.67% under AM 1.5 irradiation [7].

Although, the TiO$_2$ layer prepared from techniques such as doctor blading, screen-printing, spin coating and electrospining effect to the highest efficiency. The quality of the cell cannot be controlled because the cell efficiency depends on the skill of the operators.

In this thesis, other than the choice used in the DSSCs, TiO$_2$ plays the important role to the efficiency of the cells. The phase of TiO$_2$ used in DSSCs is anatase with the tetragonal structure as shown in Fig. 1.1. TiO$_2$ is chosen because it can be fabricated with porosity which can increase the effective surface area to about 1000 times, still show high transparency and highest mobility of anatase phase. Thus, the sensitized can hold onto the surface area of TiO$_2$ layer. The efficiency of the DSSCs is believed to be dependent on the increasing surface area of TiO$_2$ layer.

There are various techniques for preparing the TiO$_2$ layer, such as spray coating and sputtering techniques. Advantages of spray coating technique are: (1) thickness, (2) uniform of TiO$_2$ cluster can be controlled and (3) save more TiO$_2$
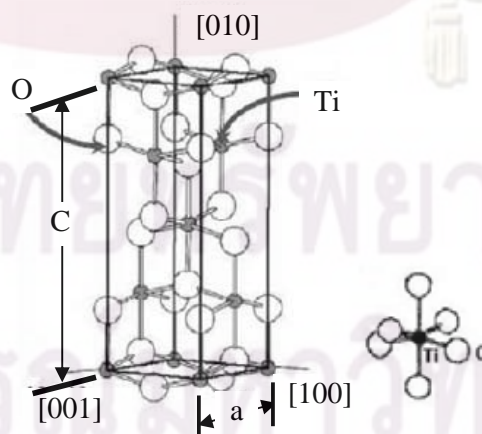
Figure 1.1: Structure of anatase TiO$_2$ phase [JCPDS:21-1272].

Table 1.1: Typical physical and mechanical properties of TiO$_2$.

Property	Value
Density	3.84 g.cm^{-3}
Resistivity (25°C)	10^{12} ohm.cm
Resistivity (700°C)	2.5x10^{4} ohm.cm
Refractive Index	2.49 (anatase)
Structure (anatase)	Tetragonal

material. Furthermore, everybody having no knowledge about DSSCs can fabricate the good DSSCs. Then, the obtained TiO$_2$ layer with the good physical properties is suitable for DSSCs fabrication. The structural and optical properties of the TiO$_2$ layer were characterized by X-ray diffraction (XRD) and optical transmission, respectively. Its surface morphology was analyzed by the atomic fore microscopy (AFM) and scanning electron microscopy (SEM). Finally, the efficiency of dye-sensitized solar cells was measured by using the I-V characterization.

Objectives of the thesis:

1) To search for appropriate condition and compare the TiO$_2$ layer by spray coating and sputtering techniques,

2) To study the physical properties of TiO$_2$ layer prepared by spray coating and sputtering techniques that suitable for dye-sensitized solar cells,

3) To compare the preparation of TiO$_2$ colloidal solution from different sizes of TiO$_2$ powder.

The procedures of the work are:

1) study the dye-sensitized solar cells and principle of dye-sensitized solar cells,

2) design the spray coating system and fabricate TiO$_2$ layers,

3) prepare the ZnO(Al) electrode on soda-lime glass (SLG) substrate which serves as the front and back TCOs by sputtering technique for dye-sensitized solar cells,

4) prepare the TiO_2 target for the TiO_2-blocking-layer on ZnO(Al)/SLG substrate by sputtering technique,

5) prepare the TiO_2 colloidal solution for spray coating technique,

6) prepare the TiO_2 layer on TiO_2-blocking-layer/ZnO(Al)/SLG substrate for the working electrode of dye-sensitized solar cells,

7) prepare the counter electrode with Pt coated on ZnO(Al)/SLG substrate by electrochemical technique for dye-sensitized solar cells,

8) fabricate the dye-sensitized solar cells,

9) measure the efficiency of the dye-sensitized solar cells by I-V characterization.

This thesis is divided into three major parts. In the first part, the introduction of dye-sensitized solar cells, the theoretical background and the fundamental concepts such as basic background of metal versus semiconductor, the semiconductor-electrolyte interface, the electrochemical potential, mechanism of dye-sensitized solar cells, charge-transfer kinetics, electron injection from dye to TiO_2, charge recombination, regeneration of the oxidized photosensitizers, recombination between injected electrons and tri-iodide ions, dye molecules and properties of Ru complex photosensitizer. The second part, the preparation of the TiO_2 absorber layer for dye-sensitized solar cells by spray coating and sputtering technique, the effectiveness of the TiO_2 blocking-layer bear upon the efficiencies of the dye-sensitized solar cells, the type of TiO_2 powder bear upon the efficiencies of dye-sensitized solar cells. In the last part, the results and discussion of the deposited films consisting of analysis of their optical, structural, morphology properties and I-V characterization. Finally, conclusions of the preparation the TiO_2 absorber layer and each layer for dye-sensitized solar cells and efficiency of dye-sensitized solar cells from spray coating and sputtering techniques are described.

CHAPTER II

THEORETICAL BACKGROUND

In this chapter, the theoretical aspect that involves the basic background of metal versus semiconductor, the semiconductor-electrolyte interface, the electrochemical potential, the mechanism of dye-sensitized solar cells, charge-transfer kinetics, electron injection from dye to TiO_2, charge recombination, regeneration of the oxidized photosensitizers, recombination between injected electrons and tri-iodide ions, dye molecules and properties of Ru complex photosensitizer will be discussed.

2.1 Basic Background of Metal versus Semiconductor

One important way of representing the band structure of solid is simple the plot of energies of the band states versus the number of state per unit volume [$N(E)$] or known as the density of states (DOS). The plot of E versus DOS for the cases of metal, insulator and semiconductor are shown in Fig. 2.1. The metals are formed when the band states are partially filled or when a filled energy band overlaps with one or more empty bands to produce a new band that is also incompletely filled with electrons. In the presence of an electric field, the unfilled band states can accept field-accelerate electrons and permit electron drift to occur, thereby producing electrical conductivity.

If the band are full, but the forbidden energy gap E_g between the highest filled band (the valence band) and the first empty band (the conduction band) is small enough to permit electrons to be transferred from the valence band to the conduction band by thermal excitation, the material is a semiconductor. The transfer of electrons from the filled valence band to the empty conduction band produces positive charges the negative charges are called holes and electrons, respectively. Both types of the charge carriers can move in their respective band, but electron flow and hole flow are according to the following expression:

(a) Partially filled band

(b) Overlapping bands

DOS

DOS

Large gap

Small gap

(c) Filled band   Empty band

(d) Filled band   Empty band
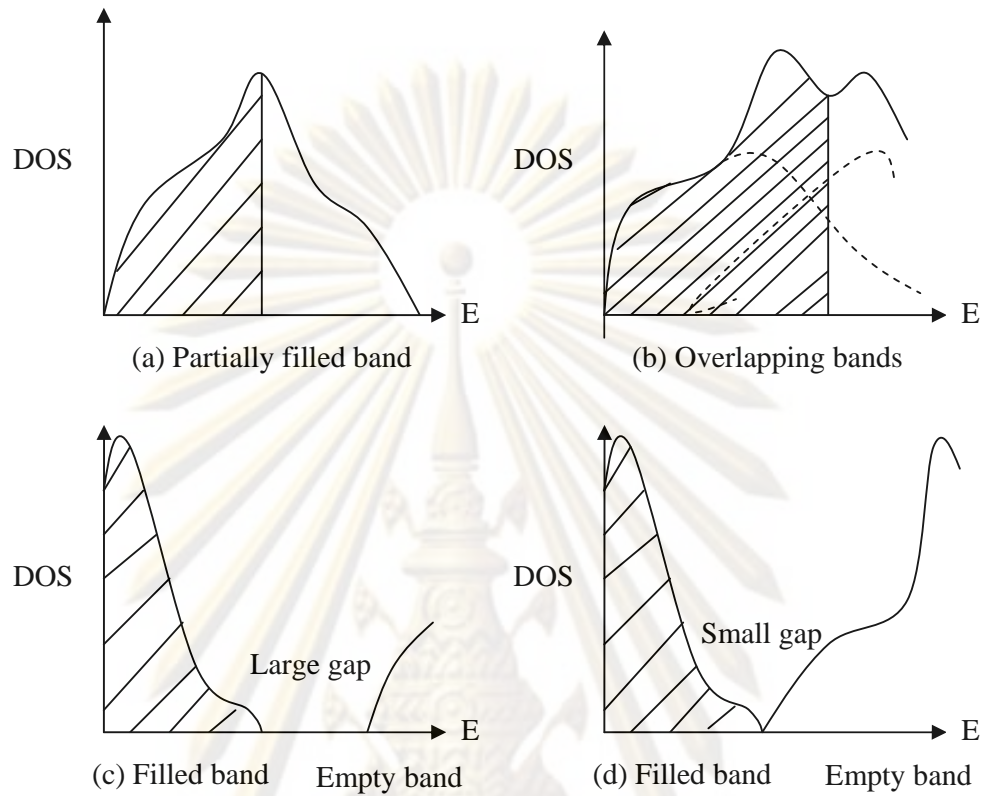
Figure 2.1: Distinction between metals (a) and (b), insulators (c) and semiconductor (d) as evident from the differences in their DOS versus energy plots.

$$\vec{J} = \sigma\vec{E} , \qquad\qquad (2.1)$$

$$\sigma = N_e q \mu_e + N_p q \mu_p , \qquad\qquad (2.2)$$

where $\vec{J}$ is the current density, $\vec{E}$ is the electric field, σ is the electrical conductivity, N_e is the electron density, N_p is the hole density, μ_e is the electron mobility and μ_p is the hole mobility.

Population of the conduction band by thermal activation from the valence band was produced equal numbers of electrons and holes. Such semiconductors are celled intrinsic semiconductors, for examples, Ge (E_g=0.67 eV), InAs (E_g=0.33 eV) and PbS (E_g=0.35 eV). The conduction and valence bands can also be populated with electrons or holes to produce electrical conductivity by adding dopants to the semiconductor. These dopants are atomic species that contain either more or fewer

electrons than the normal atomic species in the crystal; their incorporation into the lattice results in the dopants either donating their extra electrons to the conduction band or removing electrons from the valence band. In both cases these processes occur so that the dopants are like the normal atoms of the lattice in terms of total valence electrons. The electron-donating dopants (called donors) produce mobile electrons in the conduction band. For this case, negative charges become the dominant charge carrier and semiconductors doped this way are called n-type. The electron-deficient dopants (called acceptors) will accept electrons from the valence band, leaving behind positive charges. These positive charges in the valence band are called holes; positive holes will be the dominant charge carrier. These semiconductors are called extrinsic semiconductors and they have larger band gaps, the dopants form energy levels in the forbidden gap. If the energy levels of the donors and acceptors lie near the conduction and valence edges, respectively, they are called shallow dopants. The shallow dopants can create mobile charges by thermal activation processes, known as ionization. However, some dopants can create levels deep in the band gap, far removed from the conduction or valence band edges. Such levels are called deep levels; they are usually produced by interstitial dopants and by crystal dislocation and /or defects. Deep and shallow levels have quite different effects on the properties of semiconductors. For example, deep levels are frequently involved as carrier traps and recombination centers that can control the photoluminescent and transport properties of the semiconductor. Finally, if the bands are full and the energy gap to the next highest empty is large, thermal activation of electrons across the band can not occur. Such materials are insulators. Nevertheless, some insulator can still be made conductive via doping with shallow dopants. Examples are TiO_2 (E_g=3.2 eV), SiC (E_g=3.1 eV), ZnS (E_g=3.6 eV) and diamond (E_g=5.3 eV).

It is common to represent the energy band picture of semiconductor and insulators by very simplified diagram as shown in Fig. 2.2. The conduction and valence bands are represented by parallel lines separated by the band gap; dopants levels in the band gap are indicated by dashed lines.

At thermal equilibrium, the population of electrons and holes in the conduction and valence band is described by the Fermi-Direc distribution function
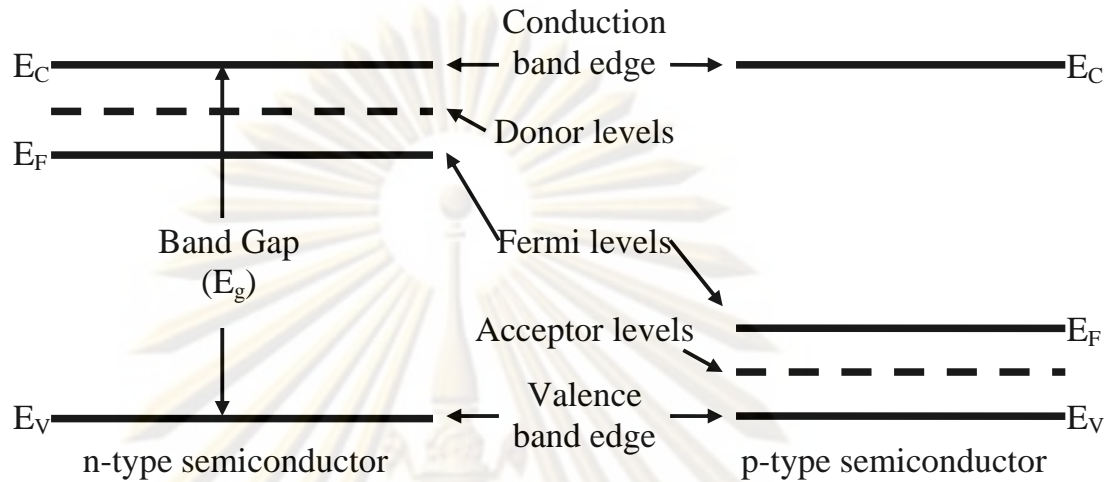
Figure 2.2: Simplified energy band diagram for semiconductors.

$f(E)$ and the density of states function, $N_E(E)$ for the conduction band and $N_V(E)$ for the valence band. The Fermi-Direc function is given by (2.3)

$$f(E) = \frac{1}{1 + \exp(E - E_F)/k_B T} \qquad (2.3)$$

where E_F is the Fermi energy (or called the Fermi level), k_B is the Boltzmann constant and T is the absolute temperature. E_F is the energy level for which the occupational probability for an electron is equal to the chemical of the system.

2.2   The Semiconductor – Electrolyte Interface

All phenomena associated with photoelectrochemical systems are based on the formation of a semiconductor-electrolyte junction when an appropriate semiconductor is immersed in an appropriate electrolyte. The junction is characterized by the presence of a space charge layer in the semiconductor adjacent to the interface with the electrolyte. A space charge layer generally develops in a semiconductor upon contact and equilibration with a second phase whenever the initial chemical potential of electrons is different for the two phases. For semiconductor, the chemical potential of electrons is given by the Fermi level in the semiconductor. For liquid electrolytes,

it is determined by the redox potential of the redox couples present in the electrolyte. These redox potentials are also identified with the Fermi level of the electrolyte.

If the initial Fermi level in an n-type semiconductor is above the initial Fermi level in the electrolyte (or any second phase), then equilibration of the two Fermi levels (or chemical potentials) occurs by transfer of electrons from the semiconductor to the electrolyte. This produces a positive space charge layer in the semiconductor (also called a depletion layer since the region is depleted of majority charge carrier). As a result, the conduction and valence band edges are bent such that a potential barrier is established against further electron transfer into the electrolyte (see Fig. 2.3). The inverse but analogous situation occurs with p-type semiconductors having an initial Fermi level below that of the electrolyte. A negative space charge or depletion layer is formed in the semiconductor, with the valence and conduction bands bending to produce a potential barrier against father positive hole transfer into the electrolyte. The width of the depletion layer w is given by

$$w = \left(\frac{2\varepsilon\varepsilon_o V_B}{qN} \right)^{1/2}, \tag{2.4}$$

where V_B is the amount of band bending in the depletion layer, N is the charge carrier density in the semiconductor, q is the electron charge, ε is the dielectric constant of the semiconductor and ε_o is the permittivity of free space. In semiconductors, w can be quite large depending upon the conductivity and the band bending; in typical cases it ranges from 100 Å to several microns. This is in contrast to metal electrodes, where the space charge layer is infinitesimally small and charge induced in the electrode essentially resides at the surface.

A charged layer also exists in the electrolyte adjacent to the interface with the solid electrode-the well-known Helmholtz layer. This layer consists of charged ions from the electrolyte adsorbed on the solid electrode surface; these ions are of opposite sign to the charge induced in the solid electrode. The wide of the Helmholtz layer is generally of the order of a few angstroms. The potential drop across the Helmholtz layer depends upon the specific ionic equilibrium at the surface.
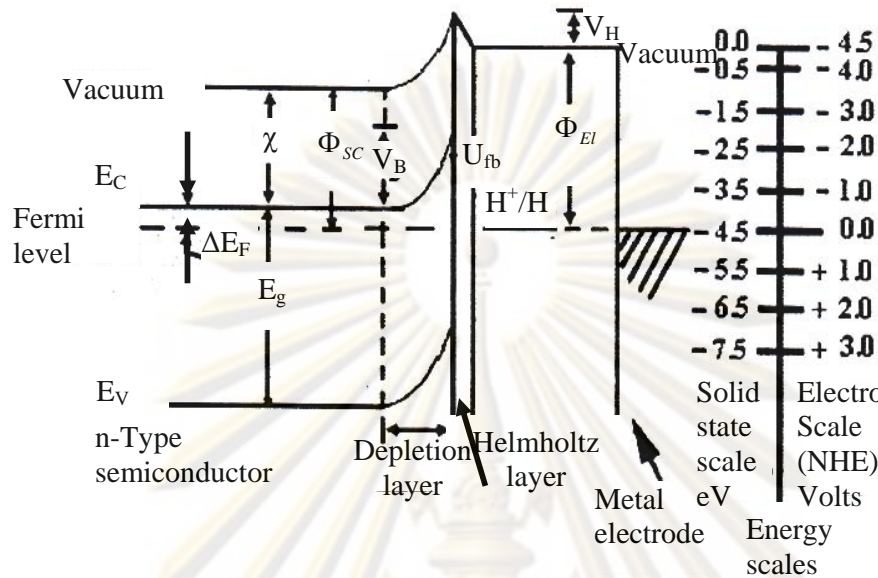
Figure 2.3: Energy levels diagram for semiconductor-electrolyte junction showing the relationships between the electrolyte redox couple (H^+/H_2), the Helmholtz layer potential drop (V_H), and the semiconductor band gap (E_g), electron affinity (χ), work function (Φ_{SC}), band bending (V_B), and flat-band potential (U_{fb}). The electrochemical and solid sate energy scales are shown for comparison. Φ_{El} is the electrochemical and solid state energy scales are shown for comparison. Φ_{El} is the electrolyte work function [8].

A very important consequence of the presence of the Helmholtz layer for semiconductor electrodes is that it markedly affects the band bending that develops in the semiconductor when it equilibrates with the electrolyte. Without the Helmholtz layer, the band bending would simply be expected to equal the difference in initial Fermi levels between the two phases (i.e. the difference between their respective work functions). However, the potential drop across the Helmholtz layer modifies the net band bending as shown in Fig. 2.3. This effect is similar to the well-known situation in Schottky junctions, where the potential barrier and band bending are usually strongly influenced by the presence of semiconductor surface state.

In Fig. 2.3, the energy scales commonly used in solid state physics and in electrochemical are shown for comparison. In the former, the zero reference points is vacuum, while in the later it is the standard redox potential of the hydrogen ion-

hydrogen (H^+/H_2) redox couple. It has been shown that these scales are related in that the effective work function or Fermi level for the standard H^+/H_2 redox couple at equilibrium is -4.5 eV with respect to vacuum. Hence, using this scheme, the energy levels corresponding to any given redox couple can be related to the energy levels of the valence and conduction bands of the semiconductor electrode. To make the connection between the energy levels of the electrolyte and the semiconductor it is necessary to introduce the flat-band potential U_{fb}, as a critical parameter characterizing the semiconductor electrode. The flat-band potential is the electrode potential at which the semiconductor bands are flat; it is measured with respect to a reference electrode, usually either the normal H^+/H_2 redox potential (NHE) or the standard calomel electrode (SCE). Hence, the band bending is given by

$$V_B = U - U_{fb} \qquad (2.5)$$

where U is the electrode potential (Fermi levels) of the semiconductor. At equilibrium in the dark, U is identical with the potential of the redox couple in the electrolyte. The effect of the Helmholtz layer on the semiconductor band bending is contained within the flat-band potential. This important parameter is the property both of the bulk semiconductor and the electrolyte, as seen from the following relationship:

$$U_{fb}(NHE) = (\chi + \Delta E_F + V_H) - 4.5 = (\phi_{SC} + V_H) - 4.5 \qquad (2.6)$$

where χ is the electron affinity of the semiconductor, (ϕ_{SC} is the work function of the semiconductor, ΔE_F is the difference between the Fermi level and majority carrier band edge of the: semiconductor, V_H is the potential drop across the Helmholtz layer, and 4.5 is the scale factor relating the H^+/H_2 redox level to vacuum.

Because of the high charge density and small width of the Helmholtz layer, V_H is constant with applied electrode potential and with charge transfer across the semiconductor-electrolyte interface; essentially all of any externally applied voltage appears across the depletion layer in the semiconductor. Consequently, at a given electrolyte composition the band edges of the semiconductor at the surface are fixed with respect to the redox potential (Fermi level) of the electrolyte, and independent of an applied voltage across the semiconductor-electrolyte interface. These energetic

relationships are determined by the flat-band potential of the semiconductor. Of course, if the composition of the electrolye is varied such that the equilibrium distribution of ions adsorbed on the semiconductor surface is affected, then V_H, and therefore U_{fb}, can charge. For many semiconductor in aqueous solutions, H^+ and OH^- are the dominant adsorbed species, and therefore V_H, and U_{fb} charge systematically with pH.

2.3 Mechanism of Dye-sensitized Solar Cell

2.3.1 Primary processes

Dye-sensitized solar cells differ from the conventional semiconductor devices. The operating principle of the DSSCs is shown in Fig. 2.4. Attached to the surface of the nanocrystalline TiO_2 layer is a monolayer of the charge transferring dye that they separate the function of light absorption from charge carrier transport. In the case of an n-type semiconductor (e.g. TiO_2), photocurrent is generated when a photon is absorption spectrum into the visible at the TiO_2 / electrolyte interface and an electron is injected into the conduction band. The original state of the dye is subsequently restored by electron donation from the electrolyte-usually containing redox system such as the iodide/triiodide couple. The regeneration of the sensitizer by the iodide intercepts the recapture of the conduction band electron by the oxidized dye. The iodide is regenerated in turn by the reduction of triiodide at the platinized counter electrode. Regeneration of iodide ions, which are oxidized in this reaction to triiodide, is achieved at a platinized counter electrode, Eqs. (2.7) - (2.12) [9]:

$$TiO_2/S + h\upsilon \rightarrow TiO_2/S^* \tag{2.7}$$

$$TiO_2/S^* \rightarrow TiO_2/S^+ + e^- \tag{2.8}$$

$$TiO_2/S^+ + e^- \rightarrow TiO_2/S \tag{2.9}$$

$$TiO_2/S^+ + \frac{3}{2}I^- \rightarrow TiO_2/S + \frac{1}{2}I_3^- \tag{2.10}$$

$$\frac{1}{2}I_3^- + e^- \rightarrow \frac{3}{2}I^- \tag{2.11}$$

$$I_3^- + 2e^- \rightarrow 3I^- \qquad\qquad (2.12)$$
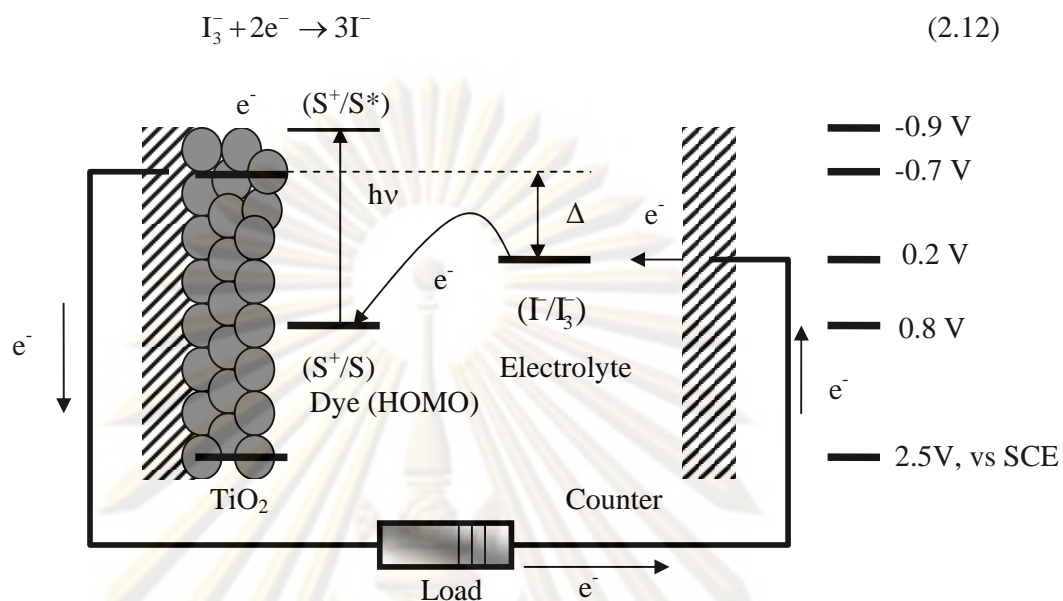
Figure 2.4: Principle of operation and energy level scheme of the dye-sensitized solar cell (DSSC) photoexcitation of the sensitizer (S) is followed by electron into the conduction band of the mesoporous oxide semiconductor. The dye molecule is regenerated by the redox system, which itself is regenerated at the counter electrode by electrons passed through the load. Potential are referred to the standard calomel electrode (SCE).
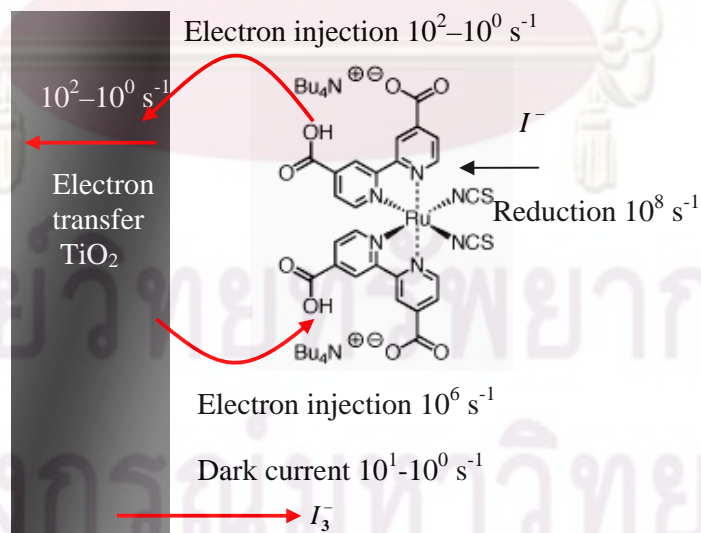
Figure 2.5: Schematic diagram of electron-transfer processes in DSSC.

The circuit is completed via electron migration through the external load. Overall, the device generates electric power from light without suffering any permanent chemical transformation.

2.4 Charge – Transfer Kinetics

2.4.1 Electron injection process

The electron-transfer kinetics in the DSSC, known as a schematic diagram in Fig. 2.5, has been under intensive investigation. Time-resolved laser spectroscopy measurements are used to study one of the most important primary processes, electron injection from photosensitizers into the conduction band of semiconductor [10]. The electron-transfer rate from the photosensitizer into the semiconductor depends largely on the configuration of the adsorbed photosensitizer material on the semiconductor surface and the energy gap between the lower unoccupied molecular orbital (LUMO) level of the photosensitizer and the conduction band level of the semiconductor. For dye N719 example, the rate constant for electron for electron injection, k_{inj} is given by Fermi's golden rule expression

$$k_{inj} = \left(\frac{4\pi^2}{h} \right) |V|^2 \rho(E) \qquad (2.13)$$

where V is the electronic coupling between the photosensitizer and the semiconductor, ρ is the density-of-state of the conduction band and h is the Planck constant. The value of V is attributed to overlap between the wave function of the excited states of the photosensitizer and the conduction band, and it depends largely on the distance between the adsorbed photosensitizer material and the semiconductor surface. In DSSC, the photosensitizer is strongly adsorbed on the semiconductor surface with carboxyl groups as the anchor, resulting in very large V between the π^* orbital of the excited state of the photosensitizer and the conduction band of TiO$_2$, which consists of the unoccupied $3d$ orbital of Ti^{+4}. In addition, the conduction band of the semiconductor has a continuous and relatively large density-of-state. Thus, electron is injected from the photosensitizer to the ground state (i.e. relation via the emission lifetime). For example, it has been observed that electron injection from N3 dye into

TiO_2 occurs on the order of femtoseconds as measure by the time-resolved laser spectroscopy [11]. This ultra-fast rate of electron injection contributes to the high energy-conversion efficiencies of the DSSC. In addition, the rate constant for electron injection depends largely on the semiconductor materials employed. A slower electron injection rate was observed with counmarin dyes and N3 dye injection into ZnO compared to the TiO_2 system [12, 13]. The different rate constant may be cause by difference in the electronic coupling between the π^* orbital of the dye and the expecting orbital in ZnO and TiO_2 and/or their density-of-states. The states near the conduction-band edge of ZnO consist of the *4s* orbitals of Zn^+, while those of TiO_2 consist of the *3d* orbitals of Ti^{+4}, which may result in the observed difference in their electronic coupling with the π^* orbital of the dye.

2.4.2 Charge recombination

The charge-recombination process between injected electron and oxidized dyes must be much slower than electron transfer from I^- ion into oxidized dyes (i.e. regeneration of dyes) to accomplish effective charge separation. It was reported that charge recombination between injection electrons on TiO_2 and cations of N719 dye occurs on the order of microseconds to millisecond, in contrast with ultrafast electron injection. The much slower charge recombination compared to electron injection leads to effective charge separation and consequently high cell performance. Charge recombination in the N719 dye/ TiO_2 system is considered that long-distance electrons transfer the bipyridyl ligand to TiO_2. Thus, it is considered that long-distance electron transfer from TiO_2 to the Ru metal center leads to a much smaller electron-transfer rate.

2.4.3 Regeneration of the oxidized photosensitizers

Electron transfer from the I^- ion into oxidized photosensitizers (cations), or regeneration of photosensitizers, is one of the primary processes need to achieve effective charge separation. The kinetics of this reaction has also been investigated by time-resoled laser spectroscopy [14]. The electron-transfer rate from the I^- ion into cations of the N719 dye was estimated to be 100 ns [14]. This reaction rate is much faster than that for charge recombination between injected electron s and dye cation.

Thus, fast regeneration of the oxidized photosensitizers also contributes to the accomplishment of effective charge separation.

2.4.4 Recombination between injected electrons and tri-iodide ions

Recombination of injection elecrons with tri-iondide ions (I_3^-) on a semiconductor as shown in Fig. 2.5, corresponding to dark current, is one of the processes in a DSSC (reaction (2.14)).

$$I_3^- + 2e^-(TiO_2) \rightarrow 3I^-$$
(2.14)

This reaction can also occur on the SnO$_2$ surface because the nanocrystalline TiO$_2$ does not completely cover the TiO$_2$ surface because of the high surface area of the TiO$_2$ relative to the SnO$_2$. This reaction contributes to the loss of photovoltaic (PV) performance in a DSSC analogous to the forward-bias injection of holes and electrons in a p-n junction. The V_{oc} in DSSC is obtained using the injection current, I_{inj}, as respresented by the following equation, as well as p-n junction solar cells:

$$V_{oc} = \frac{kT}{q} \ln\left(\frac{I_{inj}}{I_o} + 1\right)$$
(2.15)

where k is the Boltzmann constant, q is the magnitude of the electron charge, T is the absolute temperature and I_o is the dark current. I_{inj} and I_o are represented by the following equations:

$$I_{inj} = q\eta\Phi_o$$
(2.16)

$$I_o = qn_o k_{et}[I_3^-]$$
(2.17)

where η is the quantum yield for photo-generated electrons, Φ_o is the incident photon flux, n_o is the electron density on the conduction band of the semiconductor in the dark, k_{et} is the rate constant for recombination, reaction (2.14), and $[I_3^-]$ is the concentration of oxidized redox mediator, I_3^-, in the solution. From equations (2.16) to (2.17), it obtains the following equation:

$$V_{oc} = \frac{kT}{q}\ln\left(\frac{\eta\Phi_o}{n_o k_{et}\left[I_3^-\right]} + 1\right) \qquad (2.18)$$

Usually, $\eta\Phi_o >> n_o k_{et}\left[I_3^-\right]$ and equation (2.18) is simplified as follows:

$$V_{oc} = \frac{kT}{q}\ln\left(\frac{\eta\Phi_o}{n_o k_{et}\left[I_3^-\right]}\right) \qquad (2.19)$$

Dark current is considered to occur at the TiO_2/electrolyte interface where the photosensitizers are not adsorbed. To suppress dark current, pyridine derivatives such as tert-butylammonium (TBA) have been employed as coadsorbates on the TiO_2 surface, resulting in the improvement of photovoltage. TBA is considered to adsorb on the uncovered TiO_2 surface. Figure 2.5 shows the current-voltage characteristics of the N719 dye-sensitized TiO_2 solar cell under illumination and darkness, using electrolyte with and without TBA. This clearly indicates that TBA suppresses dark current, resulting in the improvement of V_{oc}. Decrease of the conduction-band level of TiO_2 owing to adsorption of TBA, which has basic property, leading to suppression of the electron injection from the dye.

2.5   Dye molecules

Ru complex photosensitizer (N719 dye)

The Ru complex photosensitizer, which contributes the primary steps of photon absorption and the consequent electron injection, is adsorbed onto the TiO_2 surface. The chemical structure of typical Ru complex photosensitizers developed by Grätzel's group is shown in Fig. 2.6 (TBA is tetrabutylammonium cation, $(C_4H_9)_4N^+$), and Fig. 2.7 shows absorption properties of the complexes in solution. The y-axis is represented by absorbance (A). The cis-bis(4,4´-dicarboxy-2,2´-bipyridine) dithiocyanato ruthenium (II) ($RuL_2(NCS)_2$ complex), which is referred to as N719 dye (or red dye), can adsorb over a wide range of the visible regions from 400 to 800 nm. The trithiocyanato 4,4´4´´-tricarboxy-2.2´:6´,2´´-terpyridine ruthenium (II) (black dye) ($RuL´(NCS)_3$ complex), absorbs in the near-IR region up to 900 nm.
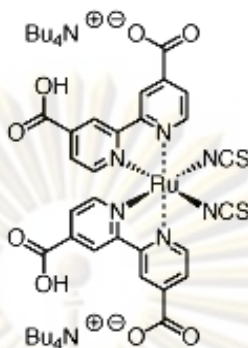
Figure 2.6: Molecular structures of typical Ru complex photosensitizers [15].

Absorption by these dyes in the visible and near-IR regions is attributed to the metal-to-ligand charge-transfer (MLCT) transition. The highest occupied molecular orbital (HOMO) and the lowest unoccupied molecular orbital (LUMO) are mainly derived from the d-orbitals of the Ru metal and the π^* orbital of the ligand, respectively. The NCS ligand shifts the HOMO level negatively, leading to a red shift in the absorption property of the complex, and also contributes electron acceptance from reduced redox ions (I^-). These Ru complex have carboxyl groups to anchor to the TiO_2 surface. Anchoring causes a large electronic interaction between the ligand and the conduction band of TiO_2, resulting in effective electron injection from Ru complex into the TiO_2. The Ru complex is absorbed on the TiO_2 surface via either carboxylate bidentate coordination or ester bonding (-C(=O)O-) as measured by FT-IR absorbed on the (101) surface of TiO_2. The coverage of the TiO_2 surface with the N719 dye reaches near 100% as derived from the surface area of TiO_2 and the amount of the dye.
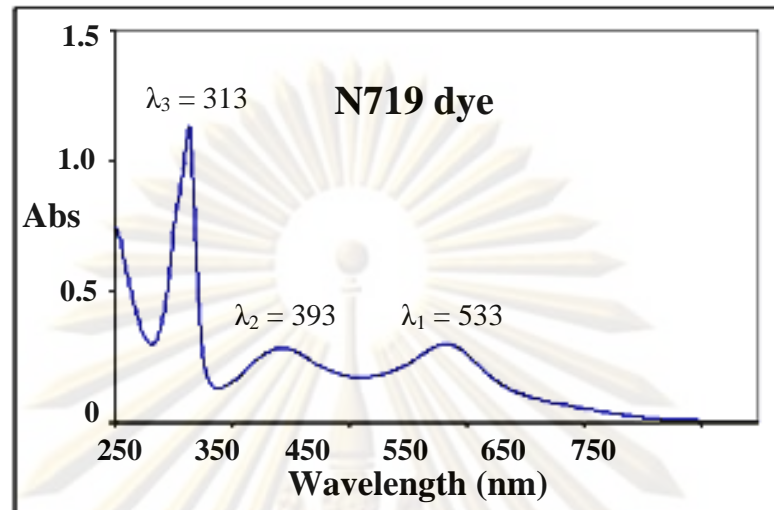
Figure 2.7: Absorption spectra of N719 dye represented by absorbance and light-harvesting efficiency [16].

CHAPTER III

ANALYTICAL METHODS OF THIN FILMS

Theoretical backgrounds involved in the analysis of the TiO_2 films are described in this chapter. The deposited films are analyzed for their optical, structural, morphology properties and I-V curve characteristics. The optical properties, such as transmission can be determined from the optical transmission measurement. The result from the optical measurement can be used to determine the energy band gap and thickness of the film using the interference from the transmission spectrum. The structure properties in terms of crystalline and crystallite size of thin films are characterized by X-ray diffraction (XRD) method. The morphology properties of thin films are characterized by Atomic Force Microscopy (AFM) and Scanning Electron Microscopic (SEM). Finally, the efficiency of cells is measured by I-V curve method.

3.1 Optical Analysis

3.1.1 Optical Method for Measuring Film Thickness

The measurement of the thickness of transparent thin films using transmitted light is a well-established technique [17]. Such optical technique for the determination of thin film characteristics involves the interaction of the film with electromagnetic irradiation. It can be said that this technique is relatively easy, nondestructive with high accuracy of measurement. In addition, the optical technique can be used to determine the optical constants such as the refractive index and absorption coefficient.
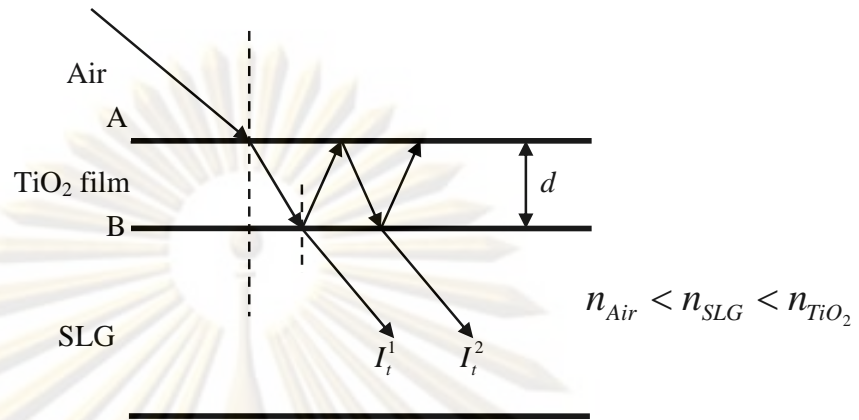
Figure 3.1: Interference caused by light traveling different paths though a film.

A schematic diagram of the transmitted light with multiple internal reflections through a transparent thin film such as TiO_2 thin film is shown in Fig. 3.1. The TiO_2 film was deposited on a transparent substrate such as a soda-lime glass (SLG). Consider the TiO_2 film of a uniform thickness d and an index of refraction n_{TiO_2}. Assume that the light rays traveling in air nearly normal to the surface of the film. It is a fundamental property of optics that the light pass thought an interface between materials of different indices will be divided into transmitted and reflected components. To determine whether the reflected or transmitted rays interfere constructively or destructively, we first note the following face

     - A wave traveling from a medium of index of refraction n_1 toward a medium of index of retraction n_2 undergoes a 180º phase change upon refraction when $n_2 > n_1$ and undergoes no phase change if $n_2 < n_1$.

     - The wavelength of light λ_n in a medium whose refraction index (n) is

$$\lambda_n = \frac{\lambda}{n}, \tag{3.1}$$

where λ is the wavelength of the light in free space. Let us apply these rules to the film in Fig 3.1, where $n_{TiO_2} > n_{Air}$. The transmitted ray 1, I_t^1, which is transmitted from the lower film surface (B) undergoes no phase change with respect to the incident wave. The transmitted ray 2, I_t^2, which is reflected from the upper film surface (A)

undergoes no change because it is reflect from a medium (air) that has a lower index of refraction. Therefore, I_t^2 is in phase with I_t^2. However, I_t^2 travels an extra distance of *2d* before the waves recombine under the surface B. If *2d* equals to integral number of wavelength, then they recombine in phase and the result is a constructive interference. In general, the condition for light transmitted thought a film, a maximum in intensity, T_{Max} will occur when

$$2d = m\lambda_n,$$
(3.2)

where *m* is a non-negative integer (*m*=0,1,2,…). Because $\lambda_n = \lambda/n$, so we can write Eq. 3.2 as

$$2nd = m\lambda.$$
(3.3)

If the extra distance *2d* traveled by I_t^2, corresponds to the half-integral multiple of the wavelength λ_n, then the two waves combine out of phase and the result is destructive interference (minimum intensity). The general equation for destructive interference, T_{Max} is

$$2nd = \left(m + \frac{1}{2}\right)\lambda.$$
(3.4)

Equation 3.3 can be used to determine the film thickness thought the relationship

$$d = \frac{m\lambda_0}{2n} = \frac{(m+1)\lambda_1}{2n} = \frac{(m+i)\lambda_i}{2n},$$
(3.5)

or $m=i\lambda_i/[\lambda_0 - \lambda_i]$, where *i* is the number of complete cycles from λ_0 and λ_i. For one cycles *i=1*, and

$$d = \frac{1}{2n(1/\lambda_1 - 1/\lambda_0)} = \frac{1}{2n\Delta(1/\lambda)},$$
(3.6)
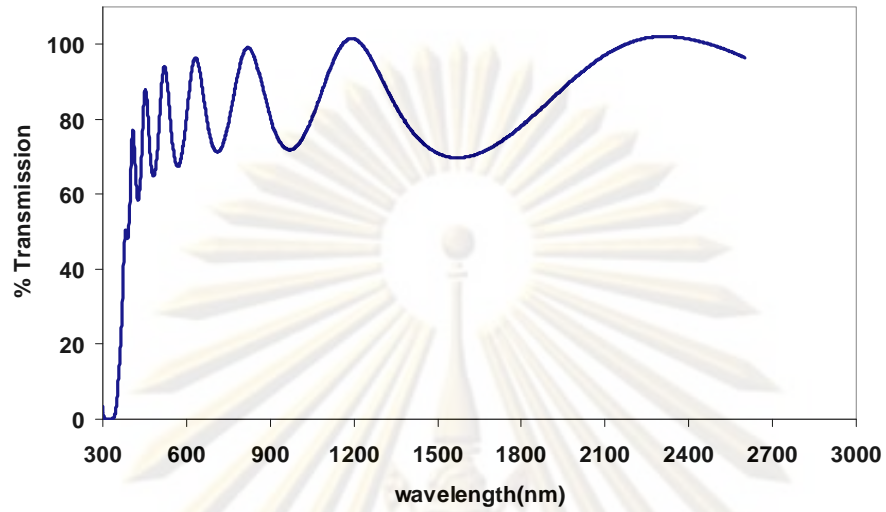
Figure 3.2: Two maxima or minima of the oscillatory transitions curve.
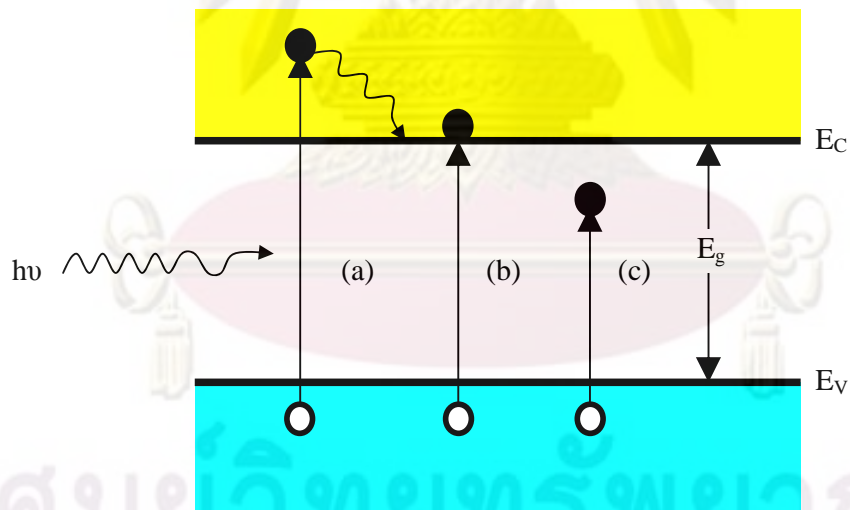
Figure 3.3: Optical absorption for (a) hυ > E_g, (b) hυ = E_g and (c) hυ < E_g.

where $1/\lambda$ is the wave number and $\Delta(1/\lambda)$ is the wave number interval between two maxima and minima of the oscillatory transmission curve as indicated in Fig. 3.2.

3.1.2 Optical Absorption [18]

Figure 3.3 describes basic transitions in a semiconductor. When the semiconductor is illuminated, photons are absorbed to create electron-hole pairs. In the case (a), the photon energy $h\upsilon$ is greater than E_g, an electron-hole pairs is generated and the excess energy, $(h\upsilon - E_g)$, is dissipated as heat, while there is no heat dissipation in (b). Both processes are called intrinsic transitions or band-to-band transition. On the other hand, for $h\upsilon$ less than E_g, a photon will be absorbed only if there are available energy states in the forbidden gap due to the physical defects as shown in Fig. 3.3 (c), and is called extrinsic transition. For reverse situation, an electron at the conduction band edge recombines with a hole at the valence band edge resulting in the emission of a photon with energy equal to that of the energy difference.

Now, let us assume that a semiconductor is illuminated by light source with intensity I_0. As the light travels through the semiconductor, the transmitted light I_t is decreased due to the absorption process in the sample. Typically, the absorption is expressed in terms of an absorption coefficient, α which is defined as the relative rate of decrease in light intensity along its propagation path:

$$\alpha = -\frac{1}{I(x)}\frac{dI(x)}{dx}.$$ (3.7)

The negative sign indicates decreasing intensity of light due to the absorption. The solution of Eq. 3.7 with the boundary condition $I(x) = I_0$ at $x = 0$ is

$$I(x) = I_0 e^{-\alpha x}.$$ (3.8)

The intensity that exits from the other side of the semiconductor at $x = d$ (Fig. 3.4) is

$$I(d) = I_0 e^{-\alpha d},$$ (3.9)

where α is related to the extinction coefficient k by

$$\alpha = \frac{4\pi k}{\lambda},$$ (3.10)

where λ is the wavelength of the light in vacuum.

The fundamental absorption refers to band-to-band (intrinsic) transition, which manifests itself by a rapid in absorption, can be used to determine the energy gap, E_g, of the semiconductor. The band-to-band transition can be divided into the following. Allowed direct transitions, [19]

$$\alpha h\upsilon = A^{'}(h\upsilon - E_g)^{1/2},$$ (3.11)

where A' is constant, $h\upsilon$ and E_g being expressed in eV.

Forbidden direct transition, [20]

$$\alpha h\upsilon = A^{*}(h\upsilon - E_g)^{3/2},$$ (3.12)

where A^{*} is constant.

For the TiO$_2$ film, the band-to-band transition is the allowed direct transition. The electrons are excited from the valence band to the conduction model of TiO$_2$ thin film.
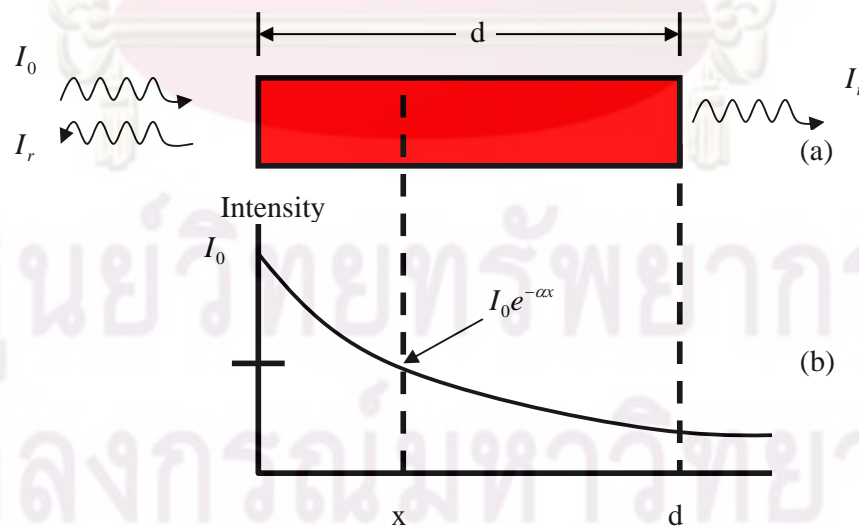
Figure 3.4: Optical absorption: (a) Semiconductor under illumination, (b) Exponential decay of light intensity.

3.1.3 Transmission

Consider a normal incidence, as shown in Fig. 3.5, the transmission T and the reflection R can be expressed in terms of the intensity of incident light I_o, the intensity of transmitted light I_t and the intensity of reflected light I_r as the followings [20];

$$T = \frac{I_t}{I_0} = \frac{(1-R)^2 e^{-\alpha d}}{(1-R)e^{-2\alpha d}},$$ (3.13)

$$R = \frac{I_t}{I_0} = \frac{(n-1)^2 + k^2}{(n+1)^2 + k^2}.$$ (3.14)

Semiconductors are generally transparent to the photon with energies less than the energies gap and product αd is large, one can neglect the second term in the denominator, then

$$T \approx (1-R)^2 e^{-\alpha d}.$$ (3.15)

If R and d are known, α can be obtained from Eq. 3.15. If R is not known, one can measure the transmission of two samples having difference thickness d_1 and d_2. Then α is obtained from

$$\frac{T_1}{T_2} \approx e^{\alpha(d_2 - d_1)}.$$ (3.16)

Note that since $T_1 = I_{t1}/I_o$ and $T_2 = I_{t2}/I_o$, then it is not necessary to know I_o in using Eq. 3.16 because one can replace T_1/T_2 by I_{t1}/I_{t2}.
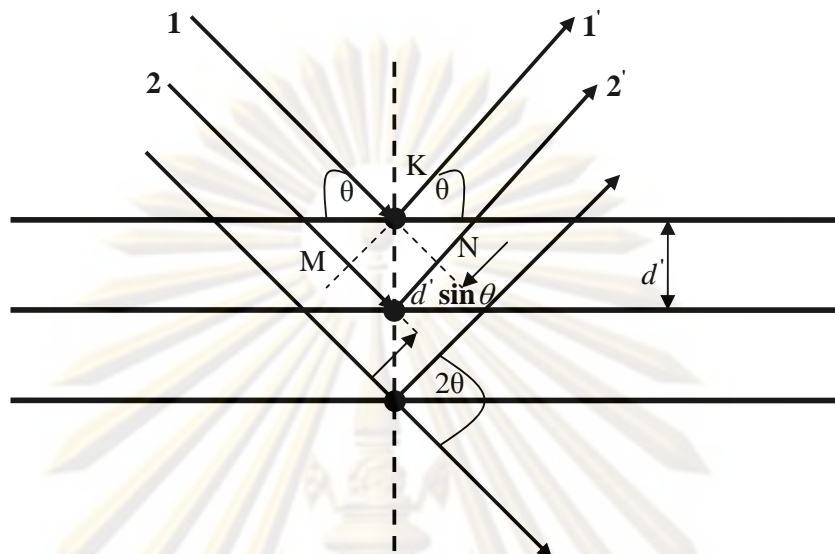
Figure 3.5: Diffraction of X-rays by crystals.

3.2 Structural Analysis

X-ray diffraction (XRD) is a technique for determining the crystal structure. The brief theory that involves this phenomenon will be discussed in this section.

3.2.1 X-Ray Diffraction (XRD)

X-ray is the electromagnetic radiation having the wavelength in the range from 0.5 Å to 2.5 Å. It is suitable for measuring the crystal structure using the diffraction effect. In Fig. 3.5, the incident beam 1 and 2 of X-ray are reflected from the crystal plane in the crystal. The angle of incidence is equal to the angle of reflection. The diffracted beam 1' and 2' are found when the reflections from parallel planes interfere constructively as shown in Fig. 3.5.

The path difference for X-ray reflected from adjacent planes is $2d'\sin\theta$. The constructive interference of the radiation occurs when the path difference is an integral number n of wavelength (λ) of X-ray, so that

$$2d'\sin\theta = n\lambda. \tag{3.17}$$

This relation was first formulated by W.L. Bragg and knows as the Bragg law.

3.2.2 Crystallite Size

The intensities of diffracted X-ray peaks at varied diffraction angles (2θ), can be used to calculate the crystallite size of sample. The crystallite size or grain size can be estimated using the Scherrer formula [21]:

$$g = \frac{0.9\lambda}{FWHM \cos\theta},$$ (3.18)

where g is the grain size, λ is the X-ray wavelength, θ is the Bragg diffraction angle in degree and $FWHM$ is the full wide at half maximum in radian of the diffracted X-ray peak.

3.3 Morphology Analysis

3.3.1 Atomic Force Analysis (AFM)

The atomic force microscopy is one type of scanned-proximity probe which is used to measure various local properties of the sample, such as height, roughness, and grain size. AFM system consists of a tube-scanner, a position-sensitive photo detector and the cantilever with a probe located at the free end. The cantilever bends in response to the interaction force between the tip and sample.

In principle, during the probe scan across the surface of the sample, a constant fore between the tip and the sample is maintained. As the cantilever deflects caused by change in the surface topography, the light from the laser is reflected onto the split photodiode. By measuring the signal difference of A-B as shown in Fig 3.6.
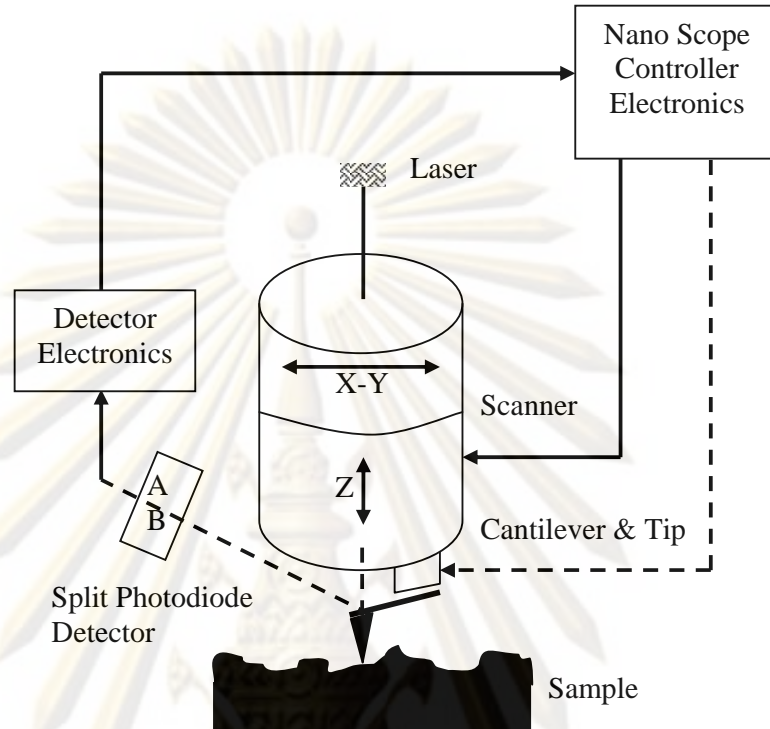
Figure 3.6: Working principle of the AFM (non contact tapping mode).

the bending of the cantilever can be measured and used to generate a map of surface topography. The surface roughness determined by the AFM is the root mean square (*rms*) roughness, Z_{rms}, which is defined as

$$Z_{rms} = \sqrt{\sum_i \frac{(z_i - \bar{z})^2}{N}},$$ (3.19)

where $\bar{z}$ is the average height of the scanned area, z is the height value of each point and N is the number of the points including the scanned area.

3.3.2 Scanning Electron Microscopic (SEM)

The surface morphology of the samples was revealed by the Scanning Electron Microscopic (SEM). The SEM was used to observe the surface of the TiO_2 layer including its cluster sizes and cross section. The SEM observations were performed on a Scanning electron microscope (JEOL JSM-6480 LV). The operating

voltage is 15 kV. The schematic diagram of the SEM equipment is shown in Fig. 3.7. Electrons thermionically emitted from tungsten filament are drawn to an anode and
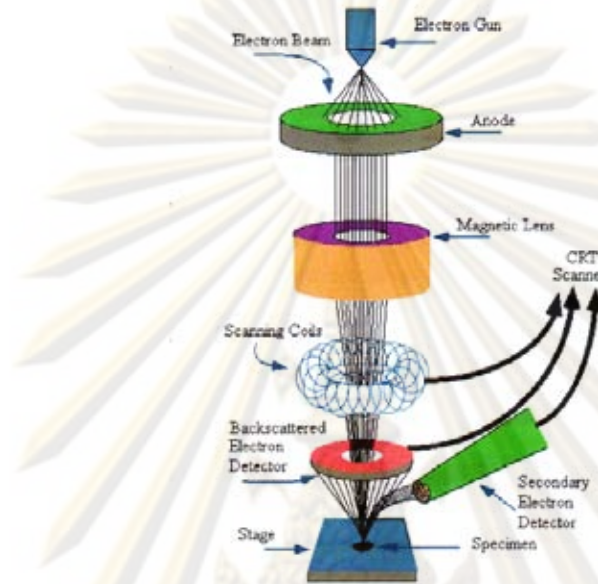
Figure 3.7: Diagram of Scanning Electron Microscope technique [22].
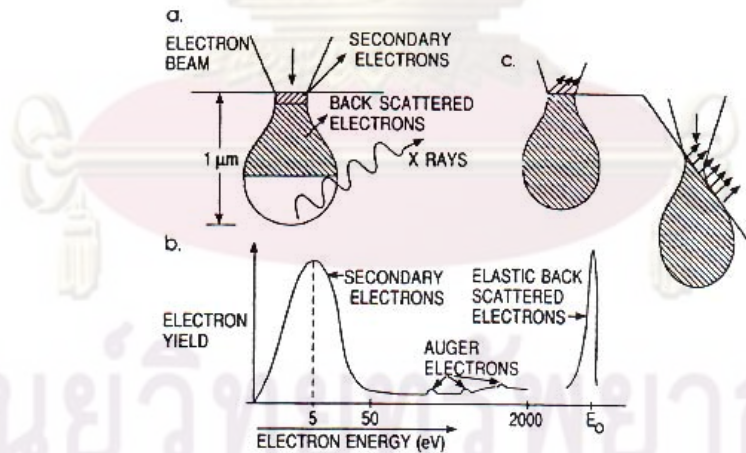
Figure 3.8 (a) Electron and photon signals emanating from tear-shaped interaction volume during electron-beam impingement on specimen surface. (b) Energy spectrum of electrons emitted from specimen surface. (c) Effect of surface topography on electron emission.

focused by two successive condenser lenses into a beam. Electron beams have energies ranging from a few keV to 30 keV.

The result is a distribution of electrons which manage to leave the specimen with an energy spectrum shown schematically in Fig. 3.8. Various SEM techniques are differentiated on the basis of what is subsequently detected and imaged. Several of these are indicated next.

3.3.2.1 Secondary Electrons

The most common imaging mode relies on detection of this very lowest portion of the emitted energy distribution. Their very low energy means they originate from a subsurface, depth of no larger than several angstroms. The signal is captured by a detector consisting of a scinitillator/photomultiplier combination and the output serves to modulate the intensity of a cathode-ray tube (CRT) which is rastered in synchronism with the raster-scanned primary beam. Image magnification is then simply given by the ratio of scan length on the CRT to that on the specimen. Resolution specifications quoted on research-quality SEMs are less than 2 nm. Great depth of focus enables images of beautiful three-dimensional quality to be obtained from non-planer surfaces. The contrast variation obtained can be understood with reference to Fig. 3.8. Sloping surfaces produce a greater secondary-electron yield because the portion of the interaction volume projected on the emission region is larger than on a horizontal surface. Similarly, edges will appear even brighter. Several secondary-electron SEM images will be shown in the chapter V.

3.4   I-V Curve Characteristic

The current-voltage (I-V) relation of typical solar cell under illumination is described by [23];

$$I = I_0[e^{\frac{q(V-R_sI)}{AkT}} - 1] + \frac{V - R_sI}{R_{SH}} - I_L, \qquad (3.20)$$

where R_s and R_{SH} are the series and shunt resistance, respectively. I_L is the light generated current. From Eq. 3.20, we can determine three important solar cell parameters that are usually used to describe the performance of the cell. The first is

the short-circuit current (I_{sc}), which represents the current flowing through cell in short circuit condition ($V=0$). The expression can be written as

$$I_{SC} = I_L - I_0[e^{\frac{qR_sI_{SC}}{AkT}} - 1] - \frac{R_S I_{SC}}{R_{SH}}.$$

(3.21)

Under normal condition, where R_s is low, R_{SH} is high and $I_L \gg I_0$, I_{sc} will be very close to I_L (e.g., $I_{sc} \approx I_L$). The second parameter is called open circuit voltage (V_{oc}) which represents the voltage across the cell in open circuit condition ($I=0$). The expression can be written as

$$V_{OC} \approx \frac{AkT}{q}\ln\left(\frac{I_L}{I_0} + 1\right).$$

(3.22)

Figure 3.9 shows the I-V characteristic of a typical solar cell under dark and illumination conditions. Therefore, we can then define some of the more important parameters in evaluating solar cells. When a finite load resistance is connected to the solar cell, the power delivered to the load is equal to the product of I and V.

In practice, a particular load resistance can be matched such that the power output is maximum power output (P_M) is defined as

$$P_M = I_M V_M,$$

(3.23)

where I_M and V_M are the corresponding current and voltage that give maximum output power (shown in Fig. 3.9).
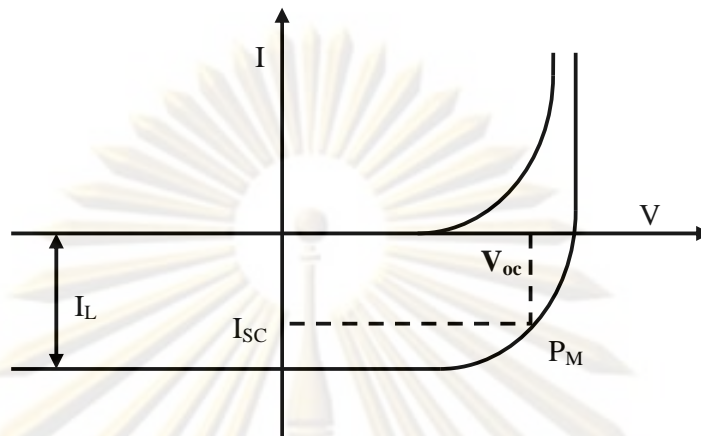
Figure 3.9: I-V characteristic curves.

The third parameter is fill factor (*FF*) which can be defined as the following,

$$FF = \frac{P_M}{I_{SC}V_{OC}} = \frac{I_M V_M}{I_{SC}V_{OC}}.$$ (3.24)

The fill factor is affected by series resistance, shunt resistance and current transport mechanism, which determined the shape of the illuminated I-V characteristics of a solar cell. Ideally, the series resistance should be very small and the shunt resistance should be high. The fill factor (FF) is a solar cell parameter which describes the junction quality. The high efficiency solar cell has a value in the range 0.7 to 0.75. Finally, the most important parameter in evaluating solar cells is the conversion efficiency (η). It is defined as the ratio of the maximum output power to the input power. The expression is given as

$$\eta = \frac{P_M}{P_{in}} = \frac{I_M V_M}{P_{in}} = \frac{FF\, I_{SC}V_{OC}}{P_{in}},$$ (3.25)

where P_{in} is the incident power of the solar radiation that reaches the surface of solar cell. Figure 3.10 shows the equivalent circuit of p-n junction of solar cells under illumination. The generation of the photocurrent I_L is represented by a current generator, in parallel with a diode that represents the p-n junction. There are two resistances shown in the figure. R_s represents the resistive loss. This resistive loss is
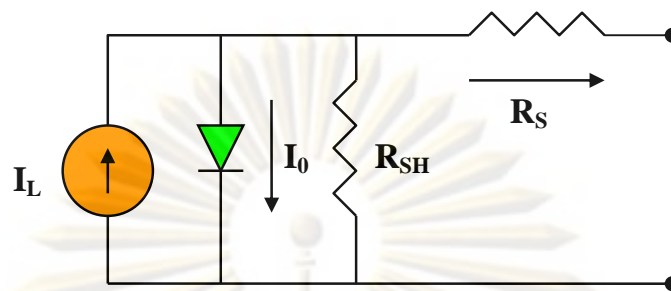
Figure 3.10: Equivalent circuit of p-n junction solar cells [23].

usually due to the sheet resistance of the window, internal resistance of absorber and contact resistance (front and black), which should ideally be zero, but always exists, in a practical solar cell. Since it represents the resistive loss outside the p-n junction, it should be minimized to deliver maximum power. The parallel (or shunt) resistance, R_{SH} represent current loss across the junction due to any parallel paths for the junction current to flow. If the junction defect density is small, R_{SH} is usually high. Ideally, such parallel path does not exist and make R_{SH} infinite. The device performances are measured under standard test condition (AM 1.5, 25ºC) using a typical solar simulator based on a single 300W-ELH lamp (tungsten-halogen light source), normalized to a light intensity of 100 mW/cm^2 as illustrated in Fig. 3.11. The device is placed on a temperature controlled stage (25±2ºC) and contacted with two-point probe configuration. A Keithley model 238 is used as current source and voltage measurement. These signals are real-time accessed to display on a PC via IEEE-488 interface card and the parameters of cells characteristics (e.g. series resistance R_s, shunt resistance R_{SH} , open-circuit voltage V_{oc}, short-circuit current density J_{sc}, fill factor FF and efficiency η), are shown.
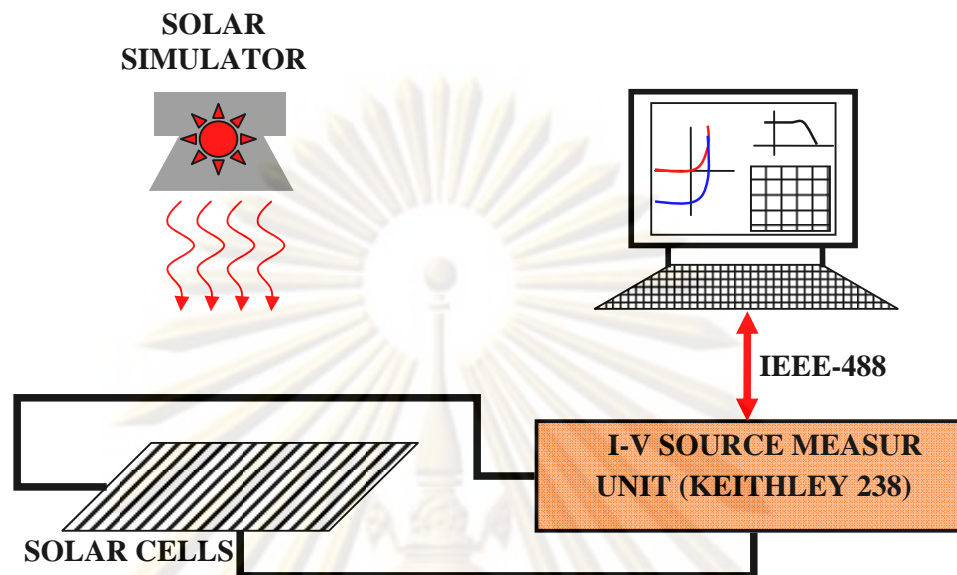
Figure 3.11: Schematic diagram of the I-V measurement system.

CHAPTER IV

EXPERIMENTAL PROCEDURES

In this chapter, I describe the experimental procedures of dye-sensitized solar cell fabrication. It consists of substrate preparation, fabrication of TiO_2 layer and TiO_2-blocking-layer as well as fabrication of Pt counters electrode and dye electrolyte. The spray coating technique of TiO_2 layer will be explained in details which involve the system and the physical parameters. In addition, the preparation of TiO_2 target for TiO_2-blocking-layer will be described.

4.1 Substrate Preparation

Soda-lime glasses (SLG) of $2.85 \text{ cm} \times 2.85 \text{ cm} \times 0.2 \text{ cm}$ in dimensions were used as substrates for the dye-sensitized solar cells (DSSCs). The substrates were first cleaned with detergent to remove coarse dust particles and then ultrasonically clean in deionize water mixed detergent at 80 ℃ for 1 hour. Next, the substrates were ultrasonically cleaned again with deionize water to remove the detergent for 1 hour. Finally the substrates were dried with flowing nitrogen gas before they were kept in a dry cabinet.

The transparent conducting oxide (TCO) i.e. $ZnO(Al)$, $In_2O_3(Sn)$ and $SnO_2(F)$ was used as front and back electrodes. $ZnO(Al)$ layer was prepared by sputtering technique. The resistivity of the film is about 1.47×10^{-3} Ω.cm. $In_2O_3(Sn)$ and $SnO_2(F)$ on SLG used in this work are a commercial grade.

4.2 Spray Coating Technique

A schematic of spray coating system is shown in Fig. 4.1. The system consists of a nozzle gun (diameter of the aperture about 0.5 mm), a spinning substrate holder, an IR lamp and a dc power supply. The speed of substrate rotation was measured by a tachometer and the speed was adjusted by varying the voltage of the power supply.

Table 4.1: The sputtering parameters of deposition for ZnO(Al) films by RF magnetron sputtering.

Base pressure	2.0×10^{-6} mbar
RF power	240 W
Argon gas pressure	3.0×10^{-3} mbar or 15 sccm
Substrate rotation	1 RPM
Substrate temperature	400 ºC
Post annealing temperature	400 ºC
Post annealing time	30 mins
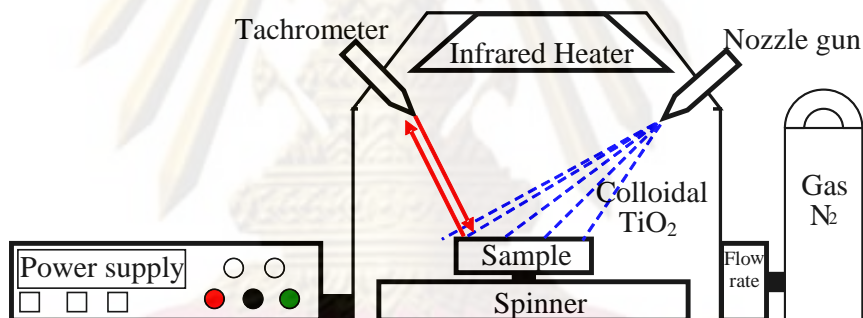
Figure 4.1: A schematic diagram of spray coating system.

The speed used in this experiment was about 1800 rpm to obtain the film uniformity. The substrate was attached on the spinning holder and can be heated up to 80ºC by the IR lamp. The TiO_2 colloidal solution was loaded into a compartment of the nozzle gun. The pressure of N_2 gas was regulated and measured for the flow rate during spray by the flow meter. The flow rate was set constant and was the physical parameter for the film fabrication.
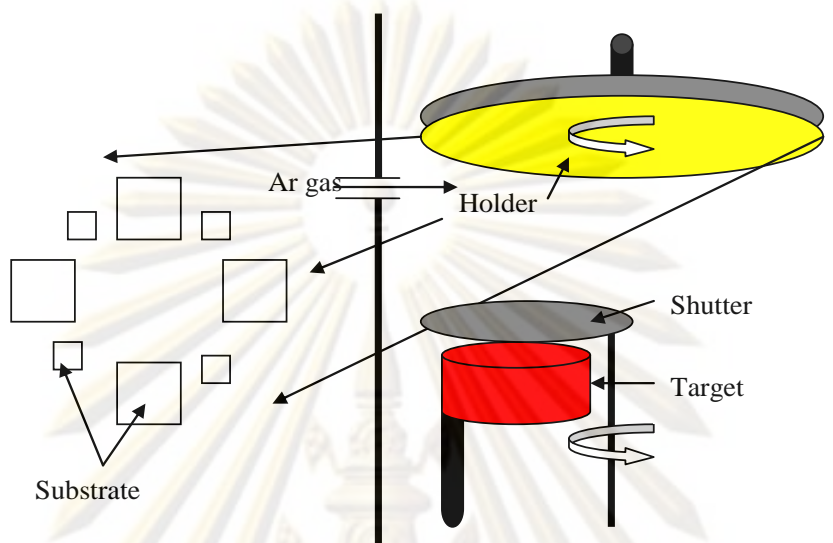
Figure 4.2: The schematic diagram of RF magnetron sputtering system.

4.3 Preparation of the ZnO(Al) Electrode

The transparent ZnO(Al) was coated on soda-lime glasses (SLG) and used as the TiO$_2$ photoelectrode. The ZnO(Al) was prepared from a ZnO(Al) target installed on the sputtering gun. Figure 4.2 shows a schematic diagram of the RF magnetron sputtering system used in this work. The substrates were parallel to the target surface with the substrate-target distance about 6.5 cm. The holder can load the substrates up to 4 pieces at a time. The shutter was placed between the target and the substrate to prohibit undesired sputtered atoms during pre-sputtering process. During the deposition, the substrate holder was rotated with the planar sputtering.

After the target and the substrates were installed in the vacuum chamber, a turbo molecular pump and a roughing pump were evacuated the chamber to obtain the high vacuum (in the order of 10^{-6} mbar). The base pressure of the system was below 2.0 x 10^{-6} mbar. First, the target surface was cleaned by sputtering with RF power of 200 W, argon gas pressure of 3.0 x 10^{-3} mbar for about 5 minutes. The substrate was heated at 400 ºC for 1 hour. The deposition parameters for the ZnO(Al) films are summarized in Table 4.1.

4.4 Preparation of TiO$_2$ Target for the TiO$_2$-blocking-layer and the TiO$_2$ Layer

The TiO$_2$ target was prepared from TiO$_2$ powder (particle size ~32 nm, Alfa Aesar, 99.9% purity). The preparation process of TiO$_2$ can be described as the followings:

(1) Humidity removal of TiO$_2$ powder

First, TiO$_2$ powder was heated to remove humidity in a furnace. The box furnace is shown in Fig. 4.3, and the profile of annealing is shown in Fig. 4.4. TiO$_2$ powder of 95.67 g was used for 4" in diameter target.

Figure 4.3: Annealing of TiO$_2$ powder in the box furnace.
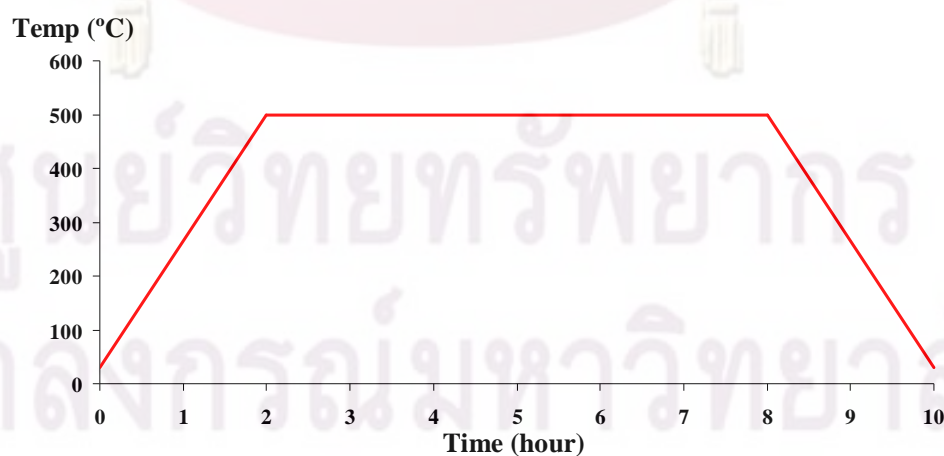
Figure 4.4: Profile of annealing of TiO$_2$ powder.

(2) Pressing the target

The TiO$_2$ target consisted of weakly aggregated powder TiO$_2$ were dispersed by grinning the powder (95.67 g) with a small amount of PVA (2% by wt., 160 ml) to agglutinant of the TiO$_2$ target. The viscous TiO$_2$ solution mixture was then put into a mold whose diameter is 4 inches. It was pressed under a pressure of 3400 psi in air at room temperature and raised up to 80ºC as shown in Figs. 4.5 and 4.6 and hold at that pressure for 1 hour as shown in Fig. 4.7. For the composition of mass mentioned in step (1), a 4-inch in diameter pellet with 5 mm thick was obtained.
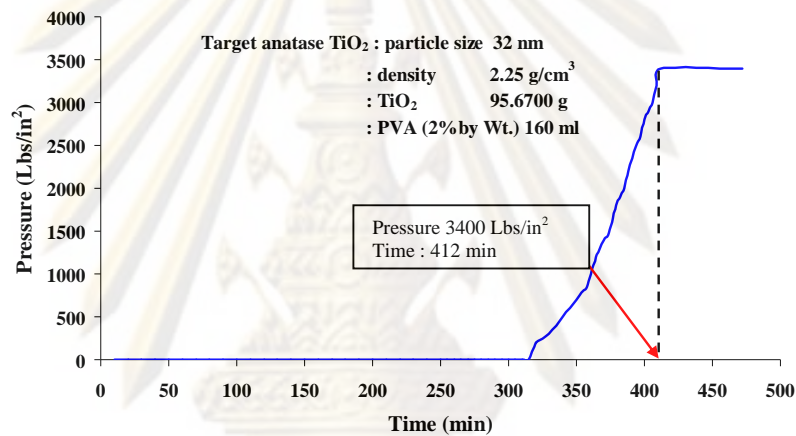
Figure 4.5: Pressure profile used for pressing TiO$_2$ target.
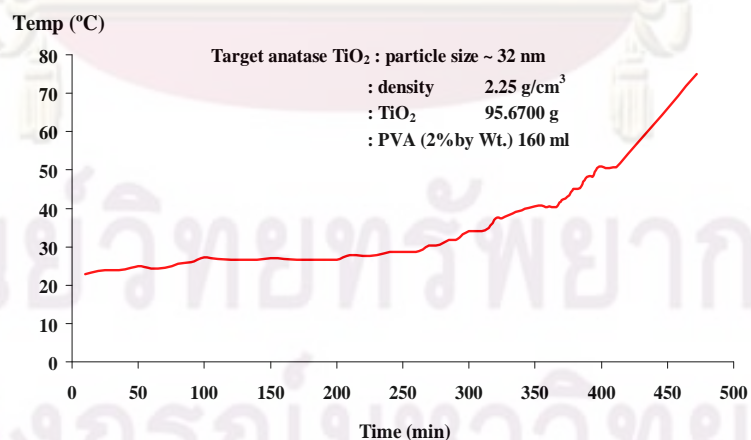
Figure 4.6: Temperature profile used during pressing TiO$_2$ target.
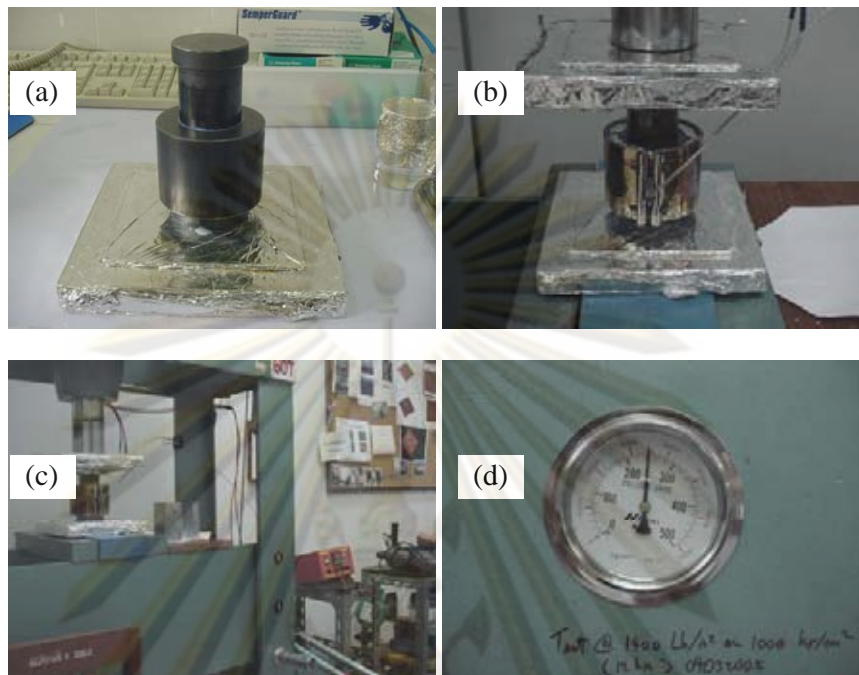
Figure 4.7: Pressing apparatus used to prepare TiO$_2$ target, (a) the viscous TiO$_2$ solution in a mold, (b)-(d) under a pressure of 3400 psi in air at room temperature to 80ºC.

Next, the target was removed from the mold and placed in the furnace under humidity control for 24 hours.

(3) Sintering the target

The TiO$_2$ pellet was heated at 80ºC about 2 hours. After that the pellet was sintered at 1200ºC for 12 hours in the atmosphere. The temperature profile during the sintering process is shown Fig. 4.8. The temperature was gradually ramped up to 1200ºC in about 12 hours and stayed at that temperature for 1 hour before the power was completely shutdown. The temperature of the furnace was freely cooled down toward the room temperature. The obtained TiO$_2$ target looks like a white ceramic target.
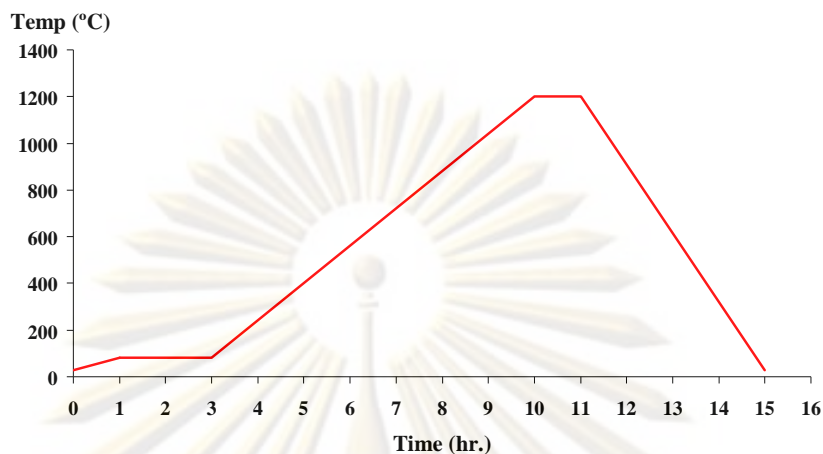
Figure 4.8: The temperature profile during sintering of TiO$_2$ target.

In order to install the target in the sputtering system, the thickness of the target must be about 5 mm thick to fit into the sputtering gun. To achieve this requirement, the target had to be polished down.

4.5 Preparation of TiO$_2$–blocking-layer by RF Sputtering Technique

The TiO$_2$ target obtained in section 4.4 was installed on the sputtering gun with silver paste applied between the target surface and the backing plate. The silver paste is used to bring the heat generated during the sputtering process out to the cooling system. The TiO$_2$-blocking-layer was deposited by RF magnetron sputtering on the ZnO(Al)/soda-lime glass (SLG) substrates. The substrates were rotated at 3 rpm. First, the surface of TiO$_2$ target was cleaned by the pre-sputtering with the power at 150 Watts, for 5 to 10 mins under pressure of approximately 4.0×10^{-3} mbar. Then, the TiO$_2$-blocking-layer was coated on the ZnO(Al)/SLG substrate by RF magnetron sputtering with the power of 225 Watts, under pressure of approximately 4.0×10^{-3} mbar with, deposition rate of approximately 0.85 nm/min for rotating substrate holder and deposition rate of approximately 1.57 nm/min for fixed substrate holder. The thickness of the TiO$_2$-blocking-layer was approximately 25, 50 and 100 nm.

4.6   Preparation of the TiO$_2$ Colloidal Solution and Spray Coating Technique for TiO$_2$ Layer

The viscous TiO$_2$ colloidal solution reported by Nazeeruddin et al. [20] was used, starting from commercial TiO$_2$ powder (particle size of 32 and 5 nm, Alfa Aesar, USA, 99.999% purity and Degussa P25, AEROXIDE). The powder consisted of weakly aggregated particles which were dispersed into separate particles by grinning the powder in a ball mill with a small amount of DI water or Polyvinylacetate (PVA), containing acetylacetone to prevent re-aggregation of the particle for 1 hour. The obtained viscous paste was then diluted by the addition of DI water or Polyvinylacetate (PVA) followed by continued grinding about 1 hour. Finally, detergent (Trinton^{TM} X-100) and DI water or Polyvinylacetate (PVA) was added [21] in order to help spreading the solution on the substrate. The concentration of TiO$_2$ colloidal solution was approximately 1% and 10% by wt., respectively. The TiO$_2$ colloidal solution was sprayed on TiO$_2$-blocking-layer/ZnO(Al)/SLG and ZnO(Al)/SLG substrates for comparison study. The specimens were annealed at 450 ºC for 1 hour in atmosphere.

The fixed parameters of the spray coating were specified with a flow rate of the colloidal TiO$_2$ solution at 1 litter/min and a rotation speed of the substrate at 1800

Table 4.2: Parameters used in the fabrication of TiO$_2$ layer by spray coating technique.

Fixed parameters	Varied parameters
Flow rate of N$_2$ gas : 1 litter/min	The TiO$_2$-blocking-layer
Substrate rotation speed : 1800 rpm	Concentration of colloidal : 1% and 10% by wt.
Diameter of nozzle gun : 0.5 mm	Types of TiO$_2$ powder : Alfa Aesar, USA, 99.9% purity and Degussa P25, AEROXIDE
Distance between nozzle gun and substrate : 22 cm	Thickness of TiO$_2$ layer : 0.1-20 μm

rpm while the varied parameters were concentration of the colloidal TiO_2 solution at 1% and 10%byWt and the thickness of TiO_2 layer at 0.1 to 20 μm, respectively, as described in Table 4.2. Finally, The TiO_2 layer on the TiO_2-blocking-layer/ZnO(Al)/SLG substrate was annealed at 450 ºC for 1 hr with the profile shown in Fig. 4.10. The deposition of the TiO_2 layer on the TiO_2-blocking-layer/ZnO(Al)/SLG substrate by spray coating technique as shown in Fig. 4.9. The TiO_2 layer was analyzed for their optical, structural, morphology properties.
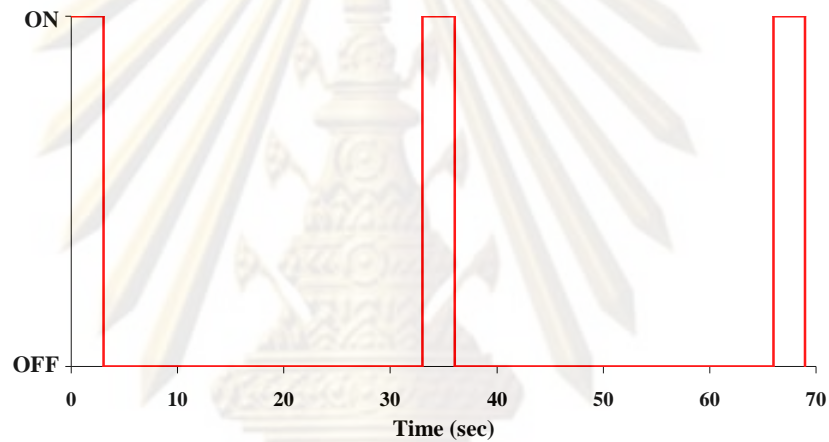
Figure 4.9: The pulse of spray coating technique for the TiO_2 layer deposited on the
TiO_2-blocking-layer/ZnO(Al)/SLG substrate.
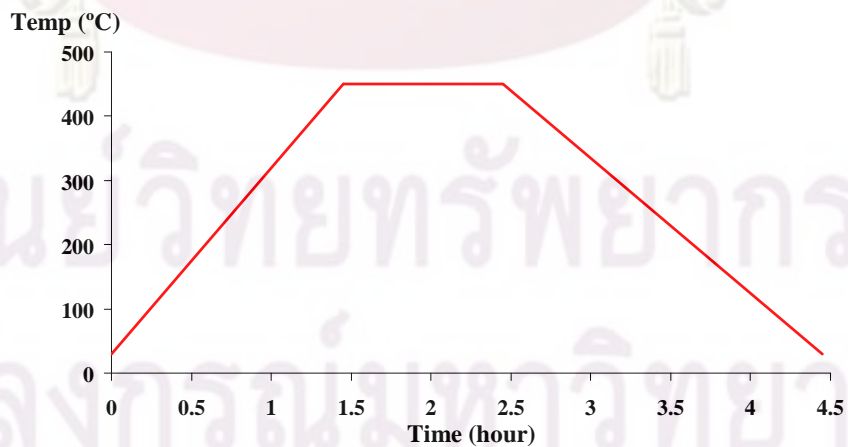
Figure 4.10: The Temp profile of annealing the TiO_2 layer on the TiO_2-blocking-
layer/ZnO(Al)/SLG substrate was annealed at 450 ºC for 1 hr.

4.7   Fabrication of Dye-Sensitized Solar Cells

4.7.1 Dye-sensitizers soaking processes

After the preparation of the TiO_2 layer on the TiO_2-blocking-layer/ZnO(Al)/SLG and ZnO(Al)/SLG substrates, the sensitizer ruthenium 535 bis-TBA dye (N719 dye) was dissolved in pure ethanol in a concentration of 25 mg of dye per 70 ml of ethanol. The TiO_2 layer on the TiO_2-blocking-layer/ZnO(Al)/SLG specimens were immersed in the sensitizer ruthenium 535 bis-TBA solution (N719 dye) face-up for 24 hours at room temperature as shown in Fig. 4.11, and then rinsed with ethanol.

4.7.2 Preparation of the Pt counter electrode by electrochemical method

The counter electrode was prepared from electrochemically platinized (0.05 g/l $PtCl_4$, 0.00156 M HCl) glass as shown in Fig. 4.12. The system consisted of a power supply (current (I) ~ 2 mA), platinum (Pt) wire and ZnO(Al)/SLG substrate. The ZnO(Al)/SLG substrate was dipped in the solution from 2 up to 10 mins. The counter Pt electrode was placed directly parallel to the ZnO(Al)/SLG substrate.

(a)   (b)
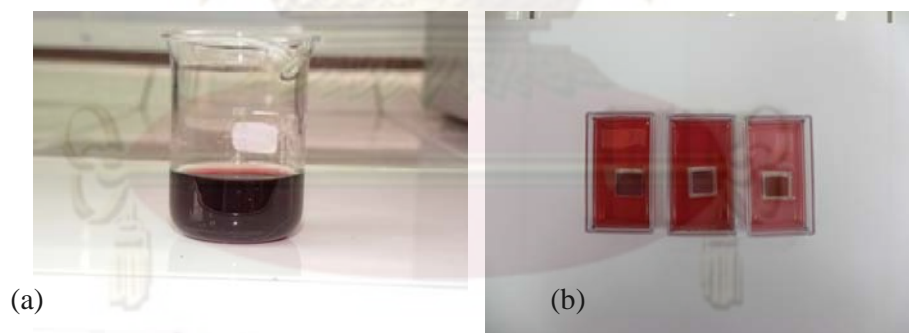
Figure 4.11: (a) the sensitizer ruthenium 535 bis-TBA solution (N719 dye) and (b) the
TiO_2/TiO_2-blocking-layer/ZnO(Al)/SLG specimens were immersed in the sensitizer
ruthenium 535 bis-TBA solution for 24 hours at room temperature.
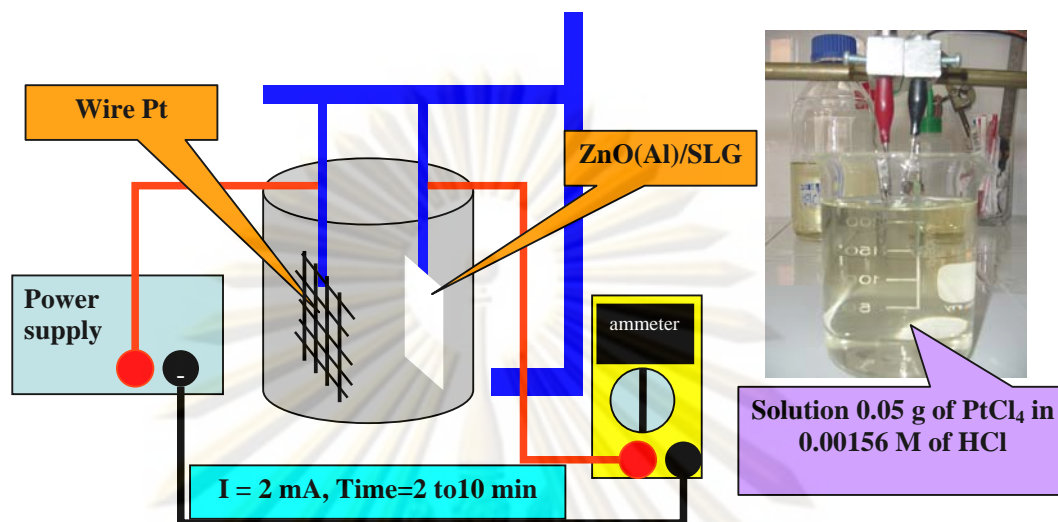
Figure 4.12: Diagram of the platinum (Pt) counter electrode by electrochemical method.

4.7.3 Cell assembly

Two sides of the cell were glued together using, for example, Parafilms, gasket SX117-60PF (SOLARONIX) or Ethylene-vinyl acetate (EVA). The seal was cut to form a frame around the glass electrodes. Heat from a hot air gun was then applied to the cells, thus forming the seal. Then, the $\left(I^-/I_3^-\right)$ electrolyte (MPN-100, SOLARONIX) was injected into the cell. The area of the cell was typically 1.25 x 1.25 cm^2 and 0.7 x 1 cm^2. Finally, the photo-to-current conversion under standard AM 1.5 radiation (100 mW/cm^2) was measured as shown in Fig 4.13.
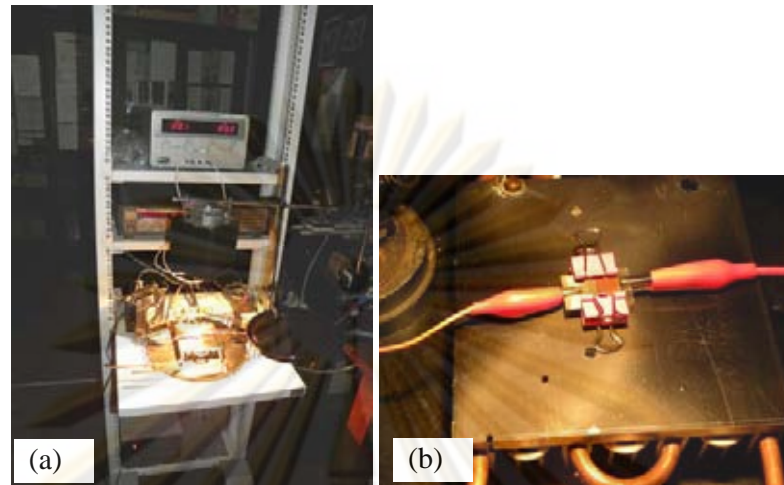
Figure 4.13: Image of the photo-to-current conversion (a) system and (b) dye-sensitized solar cell under standard AM 1.5 radiation (100 mW/cm^2) by solar simulator.
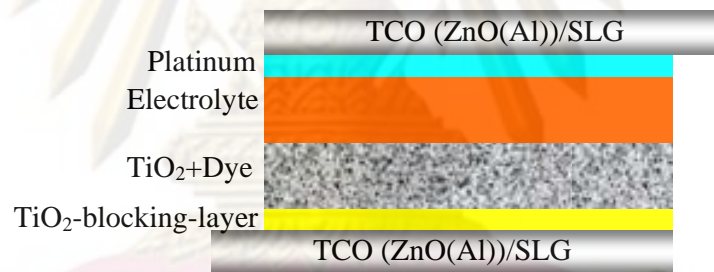
Figure 4.14: Structure of the dye-sensitized solar cells (DSSCs).

4.8 Fabrication Conditions of the Dye-sensitized Solar Cells

4.8.1 The choice of transparence conductive oxide (TCO); indium tin-oxide (ITO), ZnO(Al) and fluorine thin-oxide (FTO) electrodes

Figure 4.14 shows structure of dye-sensitized solar cells which consists of the ZnO(Al)/SLG or Indium tin oxide (ITO) or Fluorine doped tin-oxide (FTO) electrode, blocking layer, dye sit tight with TiO$_2$ layer, $\left(I^-/I_3^-\right)$ electrolyte and the Pt counter electrode.

Table 4.3: Parameters condition of the ZnO(Al)/SLG, Indium tin oxide (ITO) and Fluorine tin-oxide (FTO) electrode for the dye-sensitized solar cells

Sample	Electrode	Thickness TiO$_2$ layer (μm)
DSSC001	ZnO(Al)/SLG	1
DSSC002	ZnO(Al)/SLG	3
DSSC003	ITO/SLG	1
DSSC004	ITO/SLG	3
DSSC005	FTO/SLG	1
DSSC006	FTO/SLG	3

The transparent conductive oxides (TCO) were compared between the ZnO(Al), ITO and FTO electrodes. The colloidal TiO$_2$ solution was prepared from TiO$_2$ powder size of approximately 32 nm (Alfa Aesar, 99.9% purity) 10% by wt. The thickness TiO$_2$ layer of obtained was approximately 1 to 3 μm.

4.8.2 The TiO$_2$-blocking-layer

Figure 4.14 shows the structure of dye-sensitized solar cell which consists of the ZnO(Al)/SLG electrode, TiO$_2$ blocking-layer, dye with TiO$_2$ layer, $\left(I^- / I_3^-\right)$ electrolyte and the Pt counter electrode. The thickness of the TiO$_2$-blocking-layer was at 25, 50 and 100 nm as summarized in the Table 4.4. The fabricated cells consist of the ZnO(Al) electrode using sputtering technique, the TiO$_2$ layer using spray coating technique with the flow rate of 1 liter/min and substrate spinning rate of 1,800 rpm, N719 dye sensitizers, $\left(I^- / I_3^-\right)$ electrolyte and the Pt counter electrode using

Table 4.4: Parameters condition of the TiO$_2$ blocking-layer for the dye-sensitized solar cells

Sample	Thickness of TiO$_2$-blocking-layer (nm)	Thickness TiO$_2$ layer (μm)
DSSC007	25	1
DSSC008	50	1
DSSC009	100	-
DSSC010	50	0.5
DSSC011	-	1
DSSC012	-	2

Table 4.5: Parameters condition of the thickness of the TiO$_2$ layer and concentration of the colloidal TiO$_2$ solution for the dye-sensitized solar cells

Sample	Concentration of the colloidal TiO$_2$ solution	Thickness TiO$_2$ layer (μm)
DSSC013	10%byWt.	8
DSSC014	1%byWt.	8
DSSC015	1%byWt.	5
DSSC016	1%byWt.	2
DSSC017	1%byWt.	1

electrochemical technique. The thicknesses of TiO$_2$-blocking-layer grown by sputtering technique were varied such as 25, 50 and 100 nm. The deposition rate of TiO$_2$ layer can be increased by using TiO$_2$ powder with particle size of 5 nm (Alfa Aesar, 99.9% purity) at the same concentration.

4.8.3 The thickness of the TiO$_2$ layer by spray coating technique

The DSSCs preparation in this section is similar to preparation procedure in previous section. The thicknesses TiO$_2$ layers grown by spray coating technique were varied at 1, 2, 5 and 8 μm. The TiO$_2$ colloidal solution used in The DSSC011 and DSSC012 are varied to 10%by wt. and 1%by wt., respectively. The conditions of the other cell are summarized in the Table. 4.5.

4.8.4 Type of TiO$_2$ powder between Alfa Aesar (99.9% purity) and Degussa P25

Type of the TiO$_2$ layer was compared between powder size of approximately 5 and 32 nm (Alfa Aesar, 99.9% purity) and Degussa P25 TiO$_2$ (AEROXIDE) by spray coating technique which the DSSCs preparation is similar to preparation in preview section. Therefore, comparison the cells prepared from the TiO$_2$ colloidal solution (non-polyvinylacetate (PVA)) and the cells the TiO$_2$ colloidal solution (PVA (2% by wt.)) as shown in the Table 4.6.

Table 4.6: Type of TiO$_2$ powder for preparation of TiO$_2$ layer for the dye-sensitized solar cells

Sample	The TiO$_2$ colloidal solution	Type of TiO$_2$ powder
DSSC018	Non- polyvinlacetate (PVA)	Alfa Aesar, 32 nm (8 μm)
DSSC019	Non-polyvinlacetate (PVA)	Alfa Aesar, 5 nm (8 μm)
DSSC020	Non-polyvinlacetate (PVA)	Degussa P25 (8 μm)
DSSC021	Polyvinlacetate (PVA)	Degussa P25 (13 μm)
DSSC022	Polyvinlacetate (PVA)	Degussa P25 (20 μm)

ศูนย์วิทยทรัพยากร

จุฬาลงกรณ์มหาวิทยาลัย

CHAPTER V

RESULTS AND DISCUSSIONS

This chapter presents the experimental results and discussions. Firstly, on the preparation of soda-lime glass substrates, fabrication of spray coating system for the preparation of the TiO_2 layer, preparation of the ZnO(Al) electrode by sputtering method, preparation of the TiO_2 target for the TiO_2-blocking-layer by sputtering method, preparation of the TiO_2 colloidal solution for the TiO_2 layer by spray coating and sputtering technique will be described. The measurement and analysis will be discussed. In the second part, the results and discussions on the fabrication of the dye-sensitized solar cells are reported. Finally, the efficiency of the dye-sensitized solar cells characterized by the I-V curve will be discussed.

5.1   Soda-lime Glasses (SLG)

The photograph of a soda-lime glass (SLG) substrate along with its optical transmission spectrum are shown in Figs. 5.1 and 5.2, respectively. The surface morphology of the soda-lime glass (SLG) substrate measured by an atomic force microscope (AFM) is shown in Fig. 5.3, with the rms roughness ~ 7.7 nm corresponding to the flat surface.

Figure 5.1: The soda-lime glass (SLG) substrates with the size 2.85 x 2.85 cm².
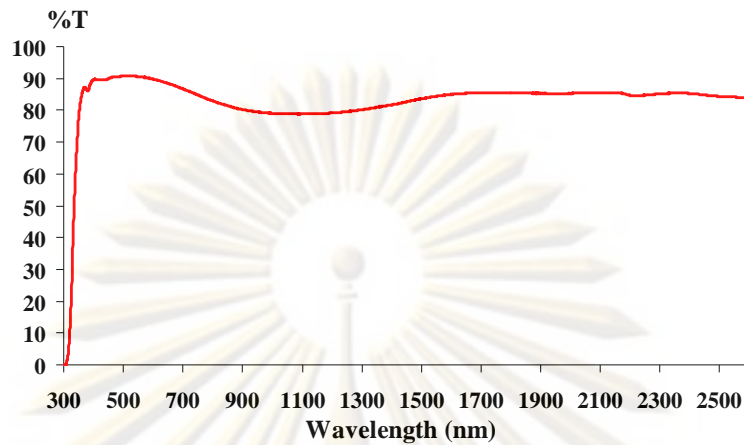
Figure 5.2: The spectra transmittance of the soda-lime (SLG) substrate.
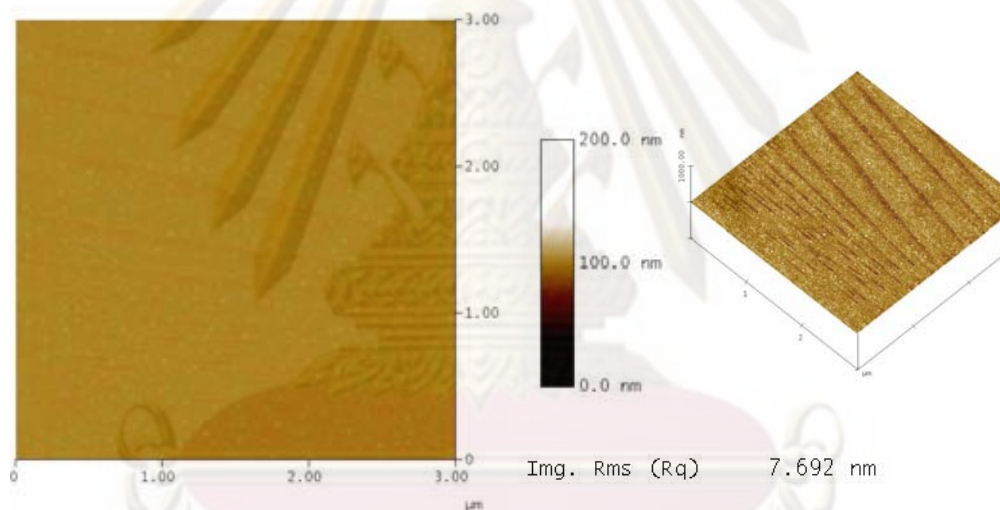
Figure 5.3: The surface morphology of the soda-lime glass (SLG) substrate.

5.2 Fabrication of a Spray Coating System

The spray coating system in Figs. 4.1 and 5.4 (a) consists of the first part, a nozzle gun for injection of the TiO_2 colloidal solution under N_2 gas controlled by a regulator, the second part, the rotating substrate holder with power supply as shown in Fig. 5.4 (b). The speed of substrate rotation was measured by the tachometer. The substrate rotation speed was adjusted using the calibration curve shown in Fig. 5.5.
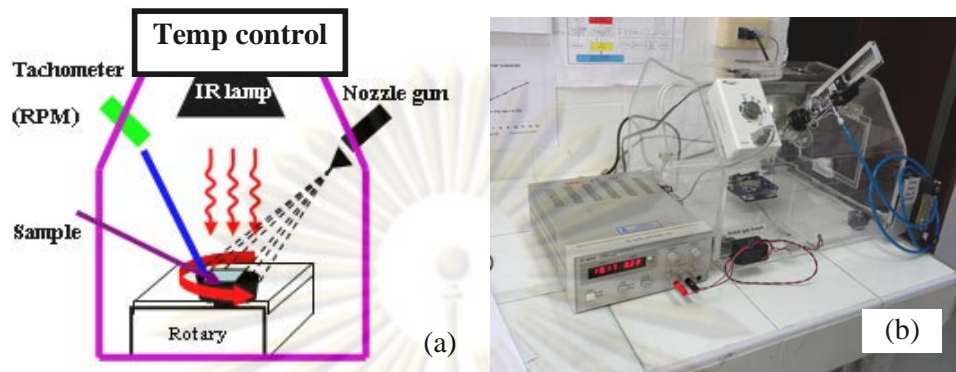
Figure 5.4: The spray coating system for the TiO$_2$ colloidal solution spray coating.
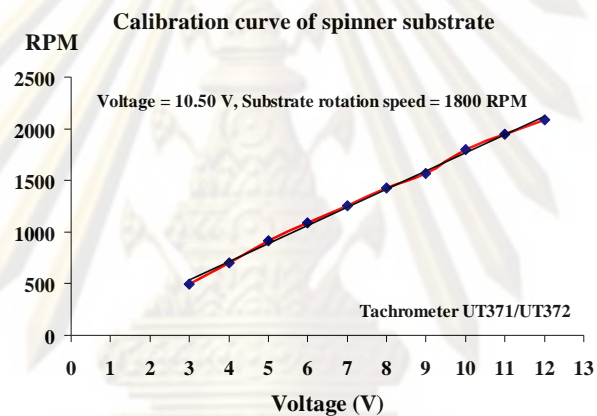
Figure 5.5: The calibration curve of spinning substrate which controlled by a power supply.

Typically, the substrate rotation speed used in this work is 1800 rpm (I=0.09 A, V=10 Volts). The substrate can be heat up to 80ºC for 5 mins (V=220 Volts) by the IR lamp.

5.3   The ZnO(Al) Electrode

The ZnO(Al) electrode were prepared on a 2.85 x 2.85 cm^2 soda-lime glass by RF sputtering technique with the thickness of about 1 μm. The ZnO(Al) electrode has high transparency in the region of visible light and near infrared (NIR), as seen in the transmission (%T) spectrum shown in Figs. 5.6 and 5.7. The cut-off at 375 nm in the transmission spectrum is the optical band gap of the ZnO(Al) film (~3.3 eV).
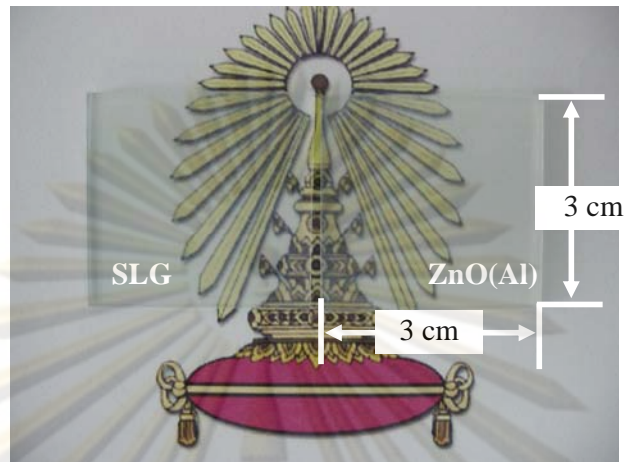
Figure 5.6: The photograph of the ZnO(Al) electrode on the SLG substrate.
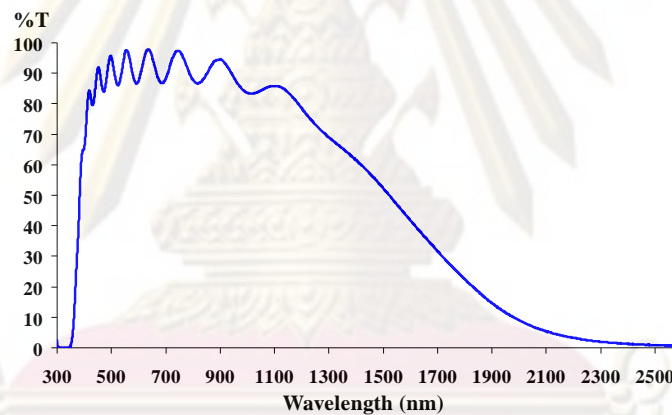
Figure 5.7: The transmission spectrum of the ZnO(Al) electrode on the SLG
substrate.

In addition to the dramatic reduction in the transmission at long wavelength (>1100 nm) is solely due to the nature of the ZnO(Al).

The structural properties of the ZnO(Al) electrode obtained by X-ray diffraction (XRD) (Bruker, D8) is shown in Fig. 5.8. It can be seen from the XRD pattern that the film has crystalline quality. A well-defined peak of ZnO(Al) (002) at $2\theta = 34.36°$ is observed. The average crystallite size obtained from the ZnO(Al) (002) peak is ~ 54 nm.
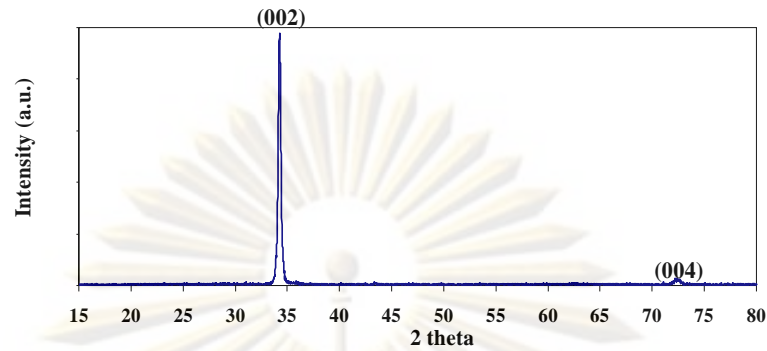
Figure 5.8: X-ray diffraction pattern of the ZnO(Al) electrode deposited on the SLG substrate.

Img. Rms (Rq)   4.289 nm
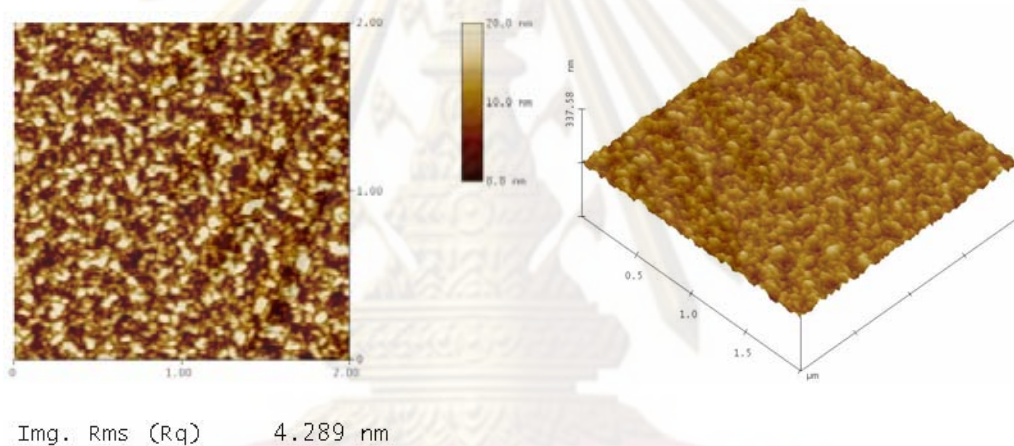
Figure 5.9: Surface morphology of the ZnO(Al) electrode deposited on the SLG substrate.

The morphology properties of the ZnO(Al) film were measured with the atomic force microscope (AFM) (Veeco Digital Instrument Dimension, 3100) over 2 x 2 μm^2. Figure 5.9 shows the images ZnO(Al) film grown on the SLG substrate with the root mean square (rms) roughness of about 4.3 nm. A closely packed spherical shape of the ZnO(Al) particles can be observed.

5.4   The TiO$_2$-blocking-layer by RF Sputtering Technique

5.4.1 The TiO$_2$ target

The TiO$_2$ target shown in Figs. 5.10 (a) and (b) looks like a coin. Its diameter and thickness are 10 cm and 5 mm, respectively.
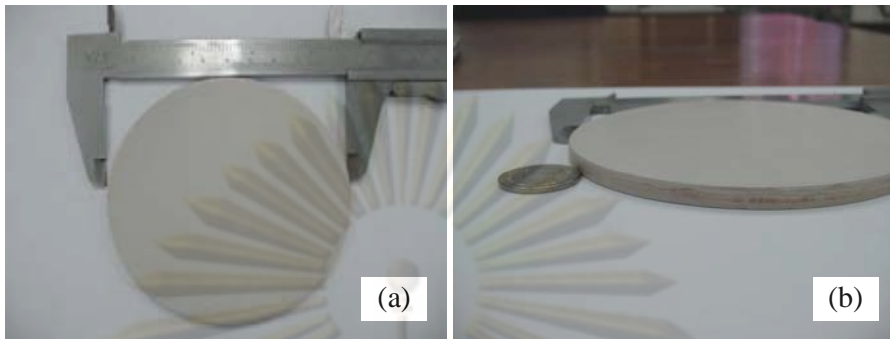
Figure 5.10: The image of the TiO$_2$ target, 10.16 cm in diameter and thickness of approximately 5 mm.
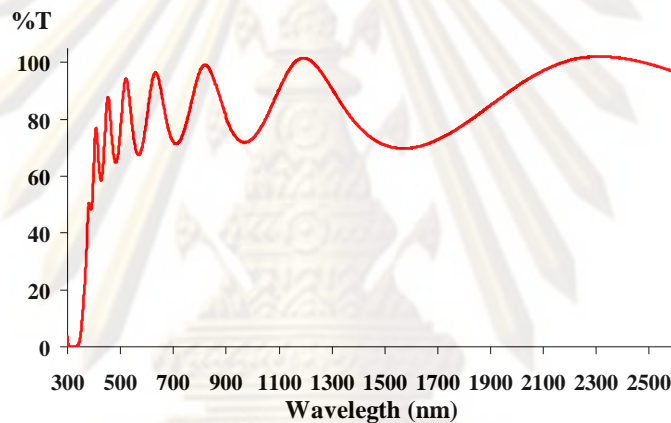
Figure 5.11: The optical transmission spectra of the TiO$_2$-blocking-layer deposited on the SLG substrate.

Next, the TiO$_2$ target was loaded into the sputtering chamber. Then, the TiO$_2$-blocking-layers were grown by sputtering technique.

5.4.2 The TiO$_2$-blocking-layer

The thickness of the TiO$_2$-blocking-layer can be calculated by transmittance (%T) spectra as shown in Fig. 5.11. Then, deposition rate at 0.85 nm/min are obtained. The thicknesses of TiO$_2$-blocking-layer grown on ZnO(Al)/SLG substrates were varied such as 25, 50 and 100 nm. From Fig. 5.12, the optical transmittance of TiO$_2$ exhibits the cut-off wavelength at 330 nm corresponding to the optical band gap (E_g) of about 3.6 eV. The TiO$_2$-blocking-layer prepared thickness at 25, 50 and 100 nm was measured resistance of approximately 50, 300 and 50 x 10^9 Ω.cm,
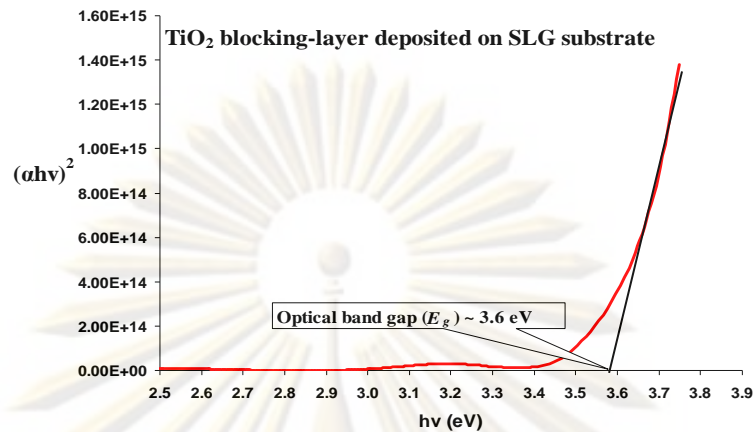
Figure 5.12: The optical energy band gap of the TiO$_2$-blocking-layer deposited on the SLG substrate.

respectively. The increase of thickness leads to the increase of series resistant (R_s). This also leads to the decrease of cell efficiency. As a result, the TiO$_2$-blocking-layer with the thickness of approximately 25 nm can be the suitable for this DSSCs fabrication.

In addition, the structural properties of the TiO$_2$-blocking-layer were determined from X-ray diffraction (XRD) measurements (Bruker, D8). Figure 5.13 shows the XRD spectra of TiO$_2$-blocking-layer deposited by sputtering technique on SLG substrate. The XRD patterns of the TiO$_2$-blocking-layer and SLG look like amorphous with none of TiO$_2$ peaks. This may due to the low crystalline quality and the very thin layer.
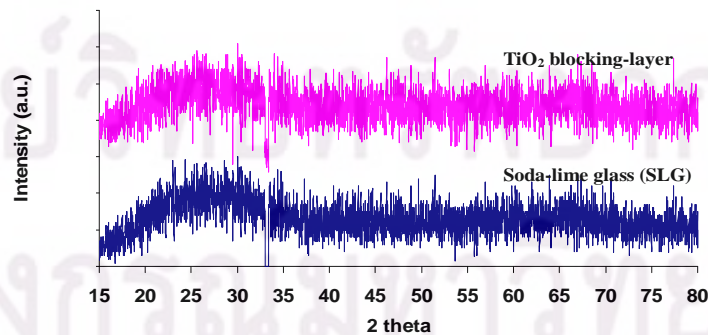
Figure 5.13: X-ray diffraction patterns of TiO$_2$-blocking-layer deposited on the SLG and SLG substrate.

Img. Rms (Rq)   19.122 nm
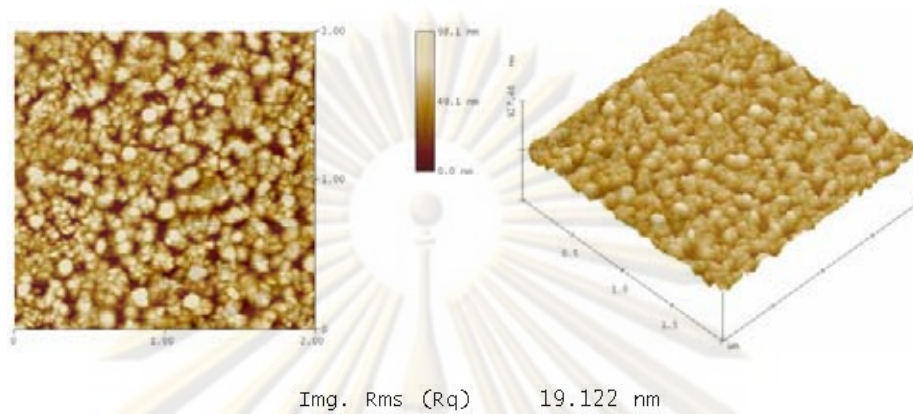
Figure 5.14: Surface morphology of the TiO$_2$-blocking-layer deposited on the SLG.

Finally, the morphology of TiO$_2$-blocking-layer was measured by the atomic force microscopic (AFM) (Veeco Digital Instrument Dimension, 3100) over 2 x 2 μm^2. Figure 5.14 shows the image of TiO$_2$-blocking-layer grown on the SLG substrate with the root mean square (rms) roughness of about 19.12 nm. The AFM image of TiO$_2$-blocking-layer revealed a closely packed rounded shape of the TiO$_2$ particles.

5.5   The TiO$_2$ Layer by Spray Coating Technique

5.5.1 The image of TiO$_2$ layer

The TiO$_2$ layers were grown on SLG, ZnO(Al)/SLG and TiO$_2$-blocking-layer/ZnO(Al)/SLG substrates. The TiO$_2$ layer is more uniform on TiO$_2$-blocking-layer/ZnO(Al)/SLG substrate. This is due to the surface of TiO$_2$-blocking-layer substrate rougher than those of the ZnO(Al) and SLG substrates. Thus, the uniformity of TiO$_2$ layer depends on the surface of the substrate.
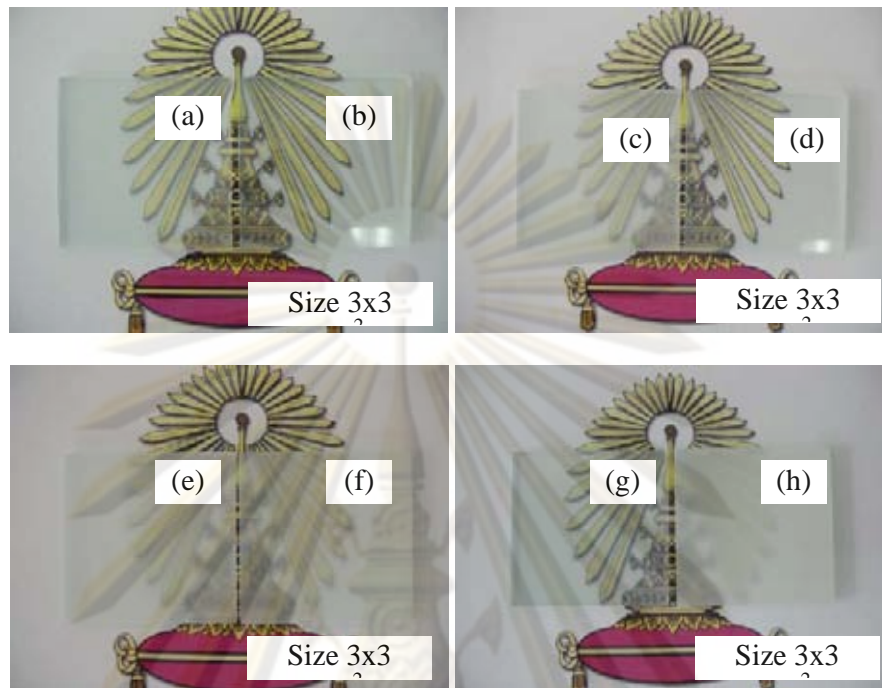
Figure 5.15: The photographs of TiO₂ layer on the SLG substrate for spraying duration (a),(c), (f) and (h) at 3, 9,15 and 18 seconds with the substrate at room temperature. (b),(d), (e) and (g) at 3, 9,15 and 18 seconds with the substrate at 80ºC.
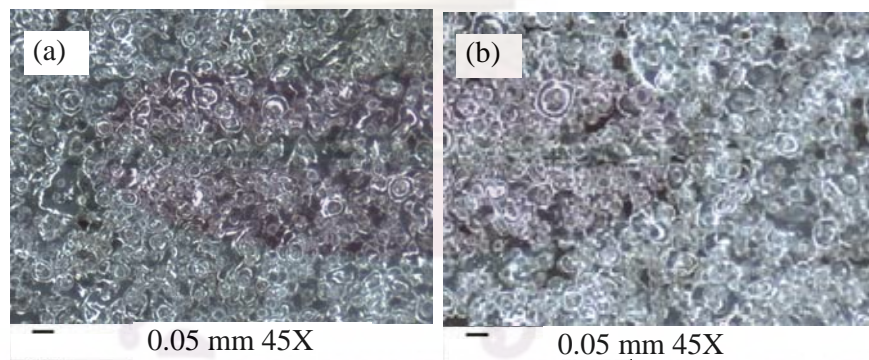
Figure 5.16: The optical image of TiO₂ films on the TiO₂-blocking-layer/ZnO(Al)/ SLG substrate for spraying duration (a) and (b) at 24 and 30 seconds from particle size ~32 nm (Alfa Aesar, USA) with the substrate at room temperature.
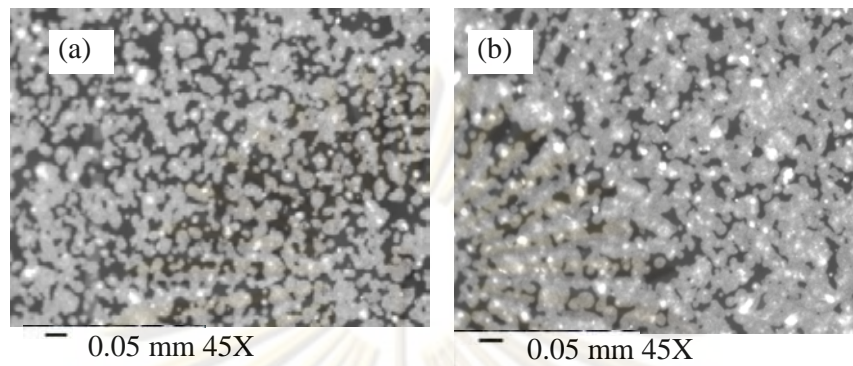
Figure 5.17: The image of TiO$_2$ films on the TiO$_2$-blocking-layer/ZnO(Al)/SLG substrate for spraying duration (a)and (b) at 3 and 6 seconds from particle size ~5 nm (Alfa Aesar, USA) with the substrate at room temperature.
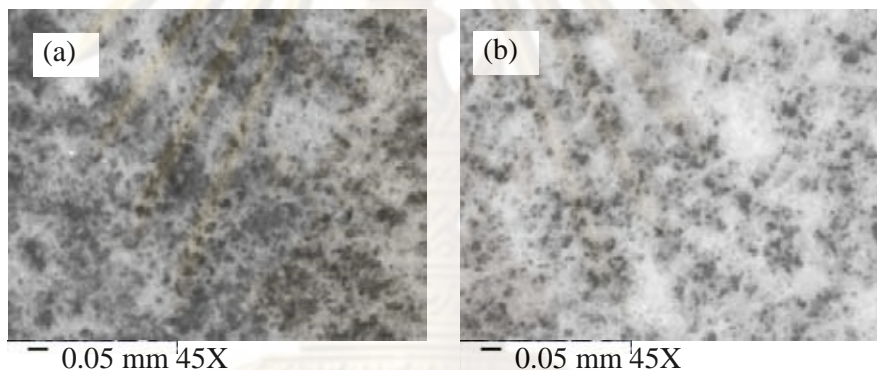
Figure 5.18: The image of TiO$_2$ layers deposited on the TiO$_2$-blocking-layer/ZnO(Al)/SLG substrate for spraying duration (a)and (b) at 60 and 150 seconds from Degussa P25 with the substrate at room temperature.

The optical images of TiO$_2$ layer (at magnification power of 45x) grown on TiO$_2$-blocking-layer/ZnO(Al)/SLG substrate exhibits the overlapped cluster. Thus, the surface area decreases. Otherwise, TiO$_2$ layer fabricated from TiO$_2$ powder with particle size of 5 mm exhibits rounded shape cluster. This leads to the increase of surface area.

Finally, Fig. 5.18 shows the optical images of TiO$_2$ layer using TiO$_2$ Degussa P25 (AEROXIDE) grown on TiO$_2$-blocking-layer/ZnO(Al)/SLG substrate. It exhibits the coral-reef-like cluster corresponding to more porousity or surface area than those of the others.

5.5.2 The optical properties of TiO$_2$ layer

The optical transmission of the TiO$_2$ layer grown on soda-lime substrates for the spraying durations of 3, 6, 9, 12, 15, and 18 seconds was observed with decreasing of the transmission spectrum when times increased as shown in Figs. 5.19 and 5.20 for non-heated and heated substrates, respectively.
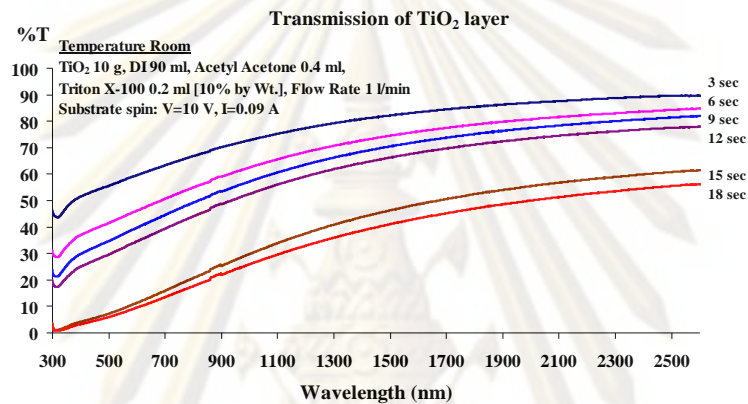
Figure 5.19: The optical transmission spectra of TiO$_2$ layer deposited on the SLG substrate for spraying duration of 3, 6, 9, 12, 15 and 18 seconds with the substrate at room temperature.
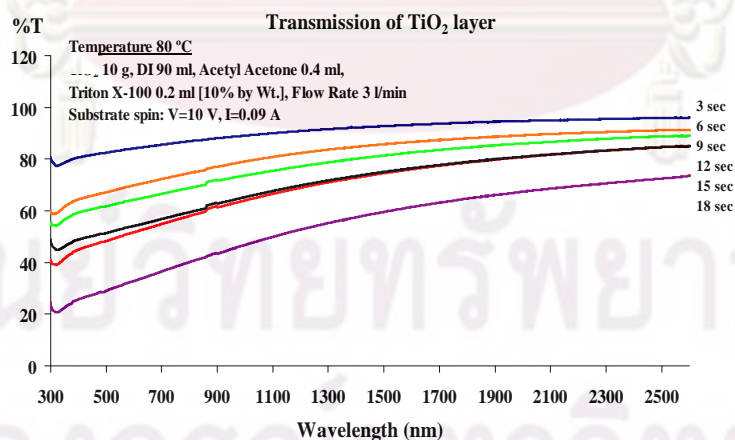
Figure 5.20: The optical transmission spectra of TiO$_2$ films deposited on the SLG substrate for spraying duration of 3, 6, 9, 12, 15 and 18 seconds with the substrate at 80ºC.
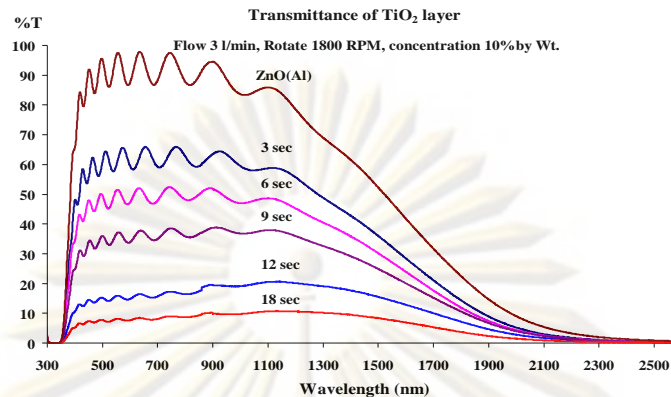
Figure 5.21: The optical transmission spectra of TiO₂ films deposited on the ZnO(Al)/SLG substrate for spraying duration of 3, 6, 9, 12, 15 and 18 seconds with the substrate at room temperature.

The optical transmission of the TiO_2 layer sprayed on the ZnO(Al)/SLG substrates are shown in Fig. 5.21. The fringes are due the multiple reflections in the ZnO(Al) layer.

The cut-off at 375 nm in the transmission spectrum is the optical band gap of the ZnO(Al) film (~3.3 eV). In addition, the dramatic reduction in the transmission at long wavelength (>1100 nm) is solely due to the nature of the ZnO(Al). It was observed that the transmission spectrum of the TiO_2 layers on the ZnO(Al)/SLG substrate is increased at 80ºC. However, the TiO_2 cluster of the heated substrates has vacancy in layer which corresponding to increasing of the series resistant (R_s) of the DSSCs. The TiO_2 layer useful for the dye-sensitized solar cells applications prepared from the non-heated or room temperature substrate.

5.5.3 Structural properties of TiO₂ layer

The structural properties of the spray coating TiO_2 layer obtained by X-ray diffraction (XRD) (Bruker, D8) is shown in Fig. 5.22.
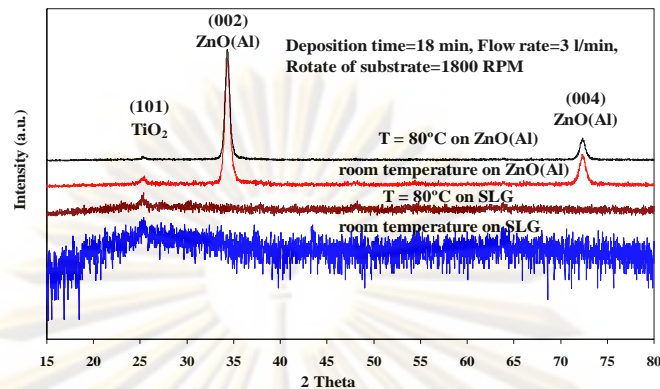
Figure 5.22: X-ray diffraction patterns of TiO$_2$ layer deposited on TiO$_2$-blocking-layer/ZnO(Al)SLG, ZnO(Al)/SLG and SLG substrate by spray coating technique which the substrates was varied substrate temperature.

The XRD spectra of the heated TiO$_2$-blocking-layer/ZnO(Al)/SLG at 80ºC substrate and non-heated TiO$_2$-blocking-layer/ZnO(Al)/SLG substrate are shown in Fig.5.22. A well-defined peak of TiO$_2$ (101) at $2\theta = 25.36º$ corresponds to the anatase phase [22] and a peak of ZnO(Al) (002) at $2\theta = 34.36º$ is seen with much stronger intensity as expected. The average crystallite size calculated from the (101) plane of TiO$_2$ using Scherrer's formula is about 10 nm which is approximately the starting particle size of TiO$_2$ powder.

Thickness of TiO $_2$ layer (32 nm) by spray coating techinque

Thickness of TiO$_2$ layer (5 nm) by spray coating technique

Thickness of TiO$_2$ layer (P25) by spray coating technique
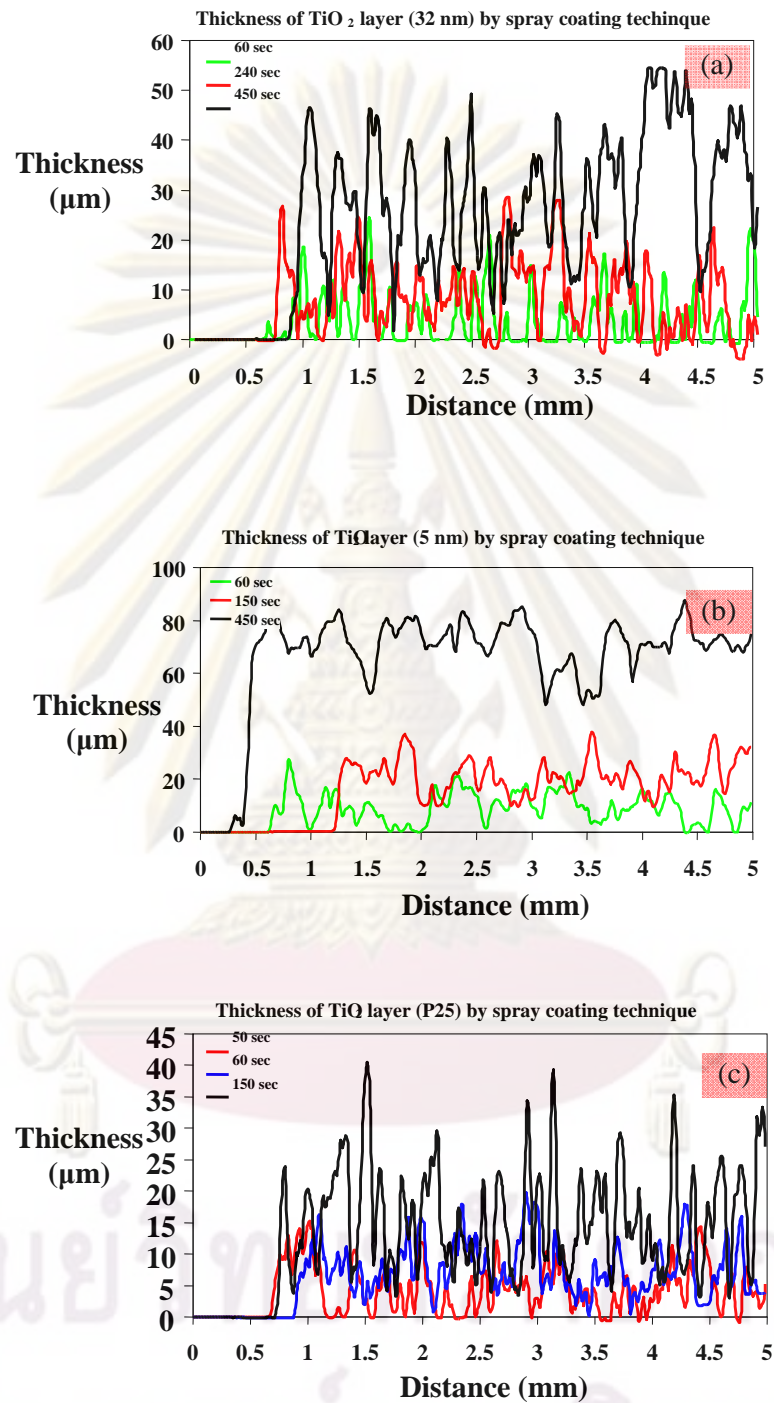
Figure 5.23: The thickness spectra of TiO$_2$ layer by spray coating technique

(measurement distance of approximately 5 mm).
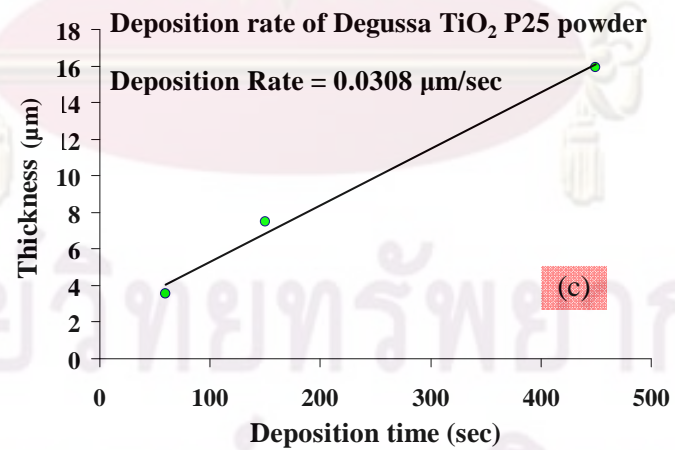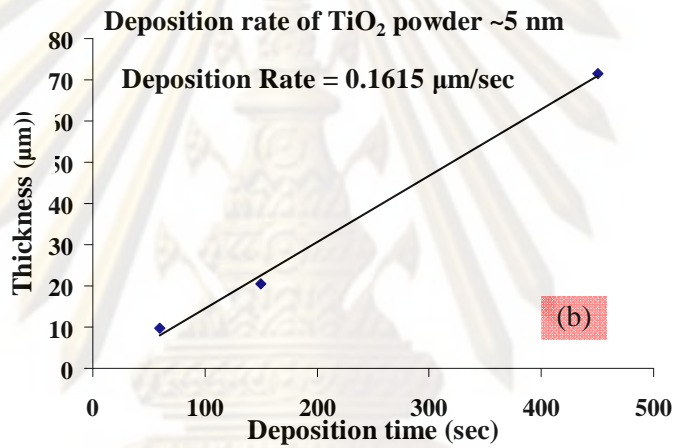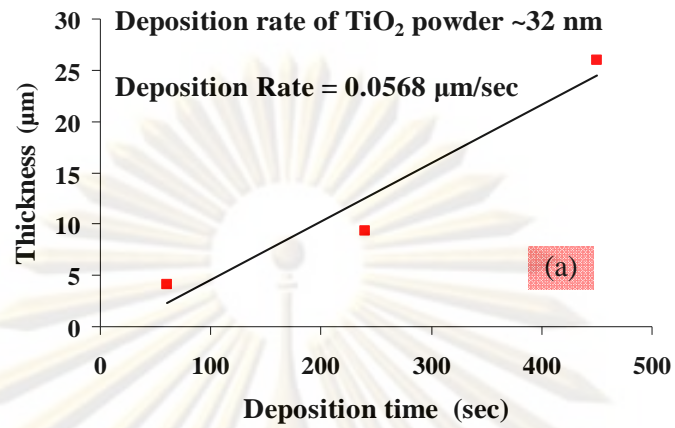
Figure 5.24: The calibration of deposition rate of the colloidal TiO₂ solution by spray coating technique (a) particle size 32 nm, (b) particle size 5 nm and (c) Degussa P25.
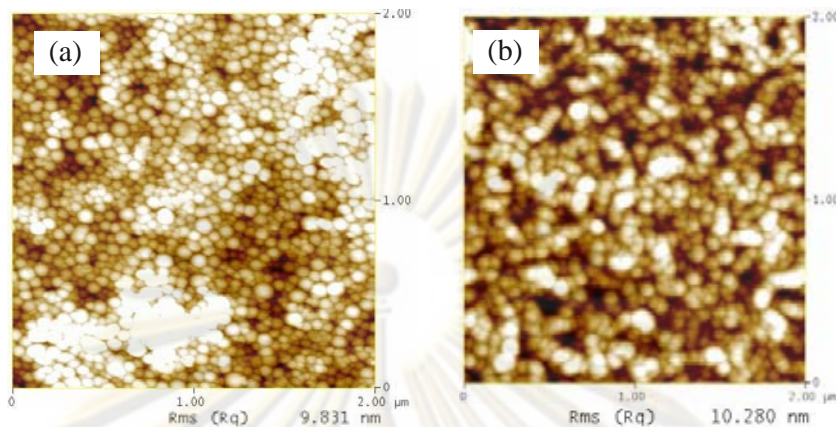
Figure 5.25: Surface morphology of the TiO$_2$ layer (a) particle size 32 nm, (b) particle size 5 nm, deposited on theTiO$_2$-blocikg-layer/ZnO(Al)/SLG substrate size 2 x 2 μm^2 by spray coating technique.

5.5.4 Thickness calculation of TiO$_2$ layer by spray coating technique

The thickness of TiO$_2$ layers was measured by a surface profiler as shown in Fig. 5.23. Then, the deposition rate can be calculated. The TiO$_2$ layers exhibited the random TiO$_2$ cluster during spray coating. The deposition rate of the TiO$_2$ layer grown by using 32 nm particle size TiO$_2$ is about 0.0568 μm/sec which is less than that grown by using 5 nm particle size TiO$_2$ (about 0.1615 μm/sec). This is probably due to smaller particle size. Finally, the deposition rate of that grown by using Degussa P25 is about 0.0308 μm/sec. The thickness of TiO$_2$ layer can be controlled by using deposition rate and time as shown in Fig. 5.24.

5.5.5 Surface morphology properties of TiO$_2$ layer

Figures 5.25 (a) and (b) compare the atomic force microscopic (AFM) images, (over 2 x 2 μm^2 area) of TiO$_2$ layers grown on TiO$_2$-blocking-layer/ZnO(Al)/SLG substrate between particle size 32 and 5 nm from Alfa Aesar (99.9% purity) with the root mean square (rms) roughness of approximately 10 nm. A closely packed round shape of TiO$_2$ particles was observed in both samples, but the TiO$_2$ particle size of 5 nm was larger porousity than particle size of 32 nm.
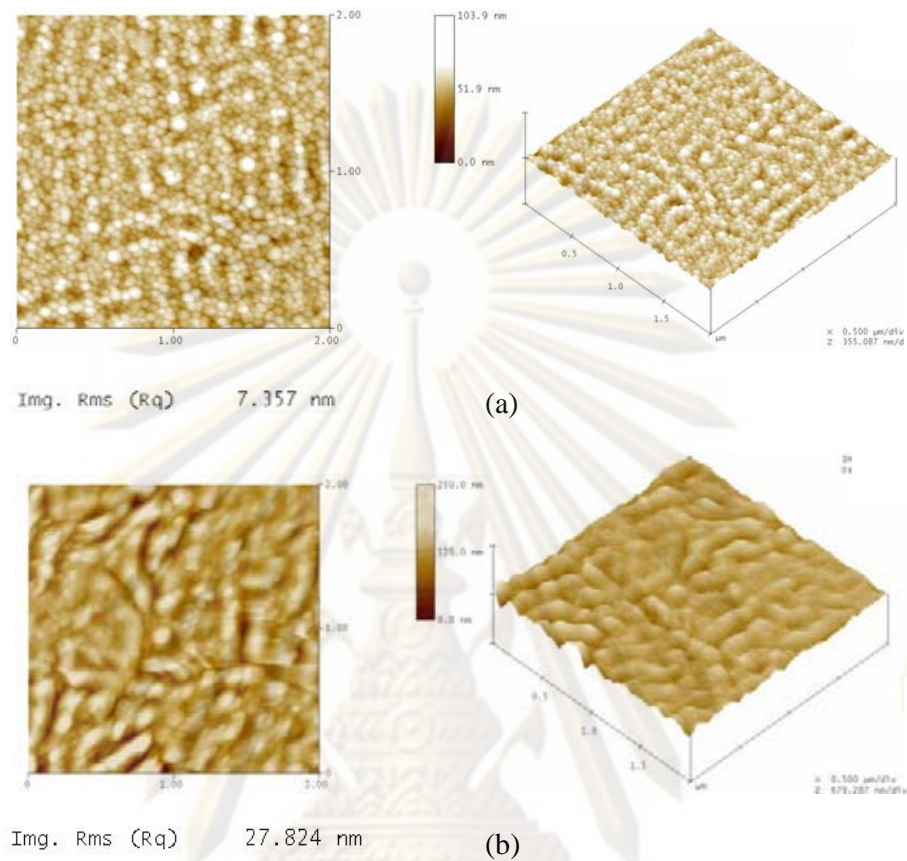
Figure 5.26: Surface morphology of the TiO$_2$ layer deposited on (a) SLG and (b) theTiO$_2$-blocikg-layer/ZnO(Al)/SLG substrate size 2 x 2 μm^2.

     The TiO$_2$ layer deposited on TiO$_2$-blocking-layer/ZnO(Al)/SLG substrate can observe rough surface more than surface of the SLG substrate with the root mean square (rms) roughness of approximately 27.8 nm as shown in Figs. 5.26 (a) and (b). Hence, the pack TiO$_2$ particle useful for preparation of the blocking layer by sputtering technique.
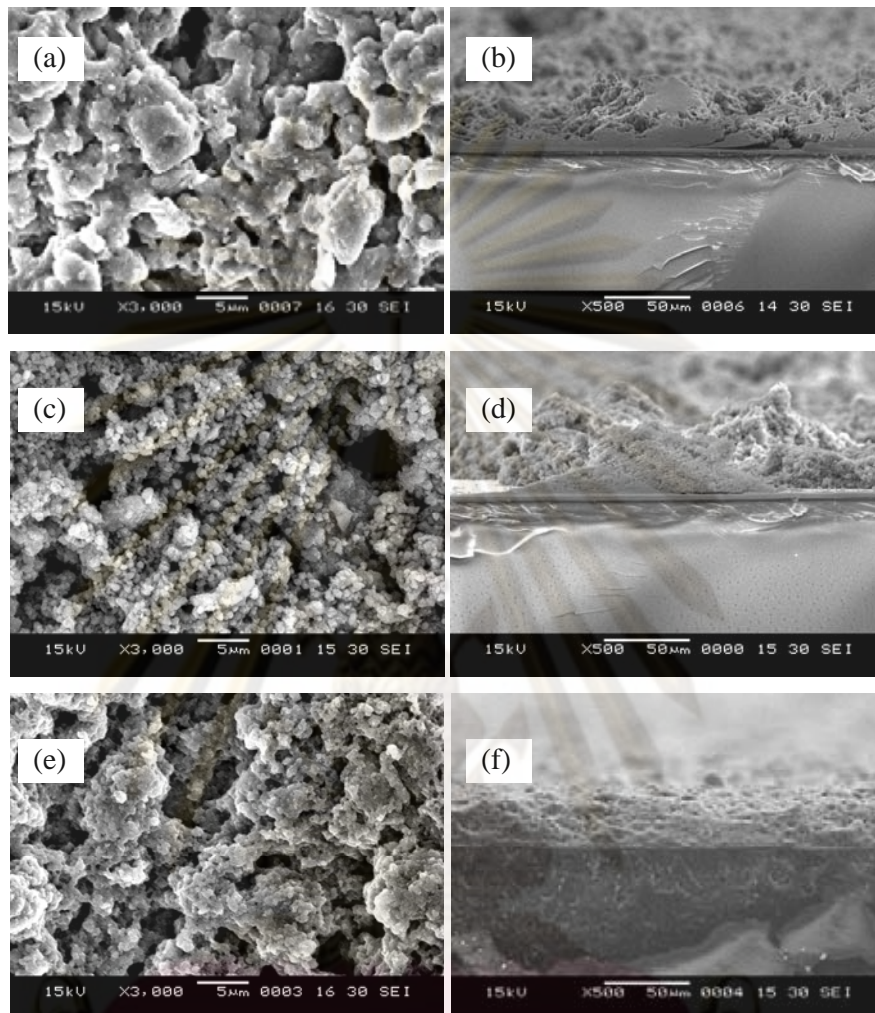
Figure 5.27: SEM image of surface TiO$_2$ layer deposited on theTiO$_2$-blocikg-layer/ZnO(Al)/SLG substrate in the area of 2 x 2 μm^2 by spray coating technique (a) and (b) particle size 32 nm, (c) and (d) particle size 5 nm (Alfa Aesar),(e) and (f) Degussa P25 (AEROXIDE) top view and cross section, respectively.
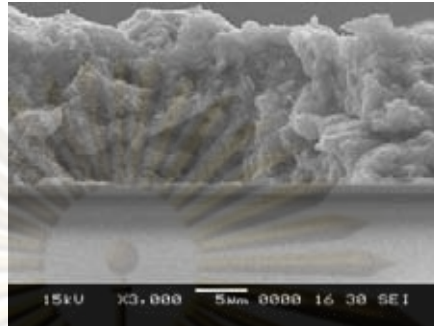
Figure 5.28: SEM image of surface TiO₂ layer deposited on theTiO₂

blocking-layer/ZnO(Al)/SLG substrate by spray coating technique (15 µm thick)

The images scanning electrons microscope (SEM) of the TiO_2 layer grown on TiO_2-blocking-layer/ZnO(Al)/SLG substrate is shown in Fig. 5.27. The first layer, ZnO(Al) film prepared by sputtering technique has thickness of approximately 1 μm. The ZnO(Al) film exhibits the smooth surface and high crystalline quality. The next layer, TiO_2-blocking-layer prepared by sputtering technique has very thin thickness at 25 nm which cannot be observed. The top layer as shown in Figs. 5.27 (a) and (b), the TiO_2 layer prepared by spray coating technique from particle size 32 nm (Alfa Aesar, 99.9% purity) has highest density of TiO_2 clusters corresponding to lower nanoporous. The TiO_2 layer prepared from particle size 5 nm (Alfa Aesar, 99.9% purity) can observe fixing of spherical particle cause nanoporous on surface as shown in Figs. 5.27 (c) and (d). The TiO_2 layer prepared from Degussa P25 (AEROXIDE) exhibits the fixing of the particle cluster like coral reef which corresponding to many nanoporous on the surface as shown in Fig. 5.27 (e). The deposition rate of the TiO_2 layer from section 5.5.4 can be useful for the thickness calculation. Thus, we obtain the estimated 15 µm TiO_2 layer using spray coating technique as shown in Fig. 5.28.

5.6 Fabrication of Dye-sensitized Solar Cells

5.6.1 Dye-sensitizers (N719 dye)

The TiO_2 layer specimens were immersed in the sensitizer ruthenium 535 bis-TBA solution (N719 dye) for 24 hours at room temperature as shown in Fig. 4.11 (b). The porous TiO_2 was infiltrated by the sensitizer dye (N719 dye) as shown in Fig.

5.29. Difference of color depends on the thickness of the TiO_2 layer and porous amount of the TiO_2 layer due to dye absorber.

5.6.2 The Pt counter electrode by electrochemical

The Pt counter electrode prepared from electrochemically platinized as shown in Fig. 5.30. The photograph focuses on uniform the Pt counter electrode. However, the thickness of the Pt counter electrode does not impact to the catalyst electrons.
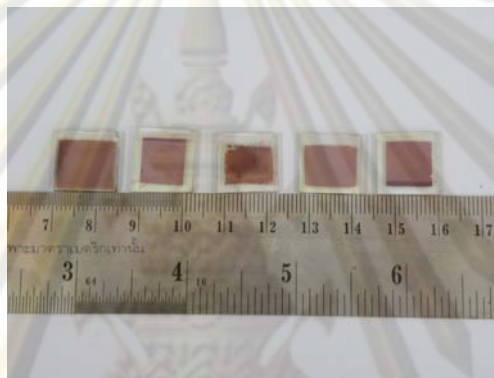
Figure 5.29: The TiO$_2$ layer on the TiO$_2$-blocking-layer/ZnO(Al)/SLG substrate absorbed by the sensitizer ruthenium 535 bis-TBA solution (N719 dye) solution for 24 hrs.
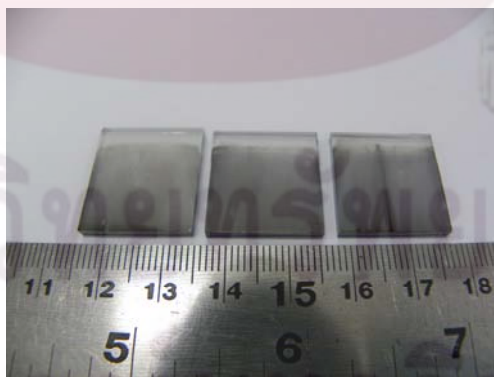
Figure 5.30: The platinum (Pt) counter electrode was deposited on ZnO(Al)/SLG substrate by electrochemical method.
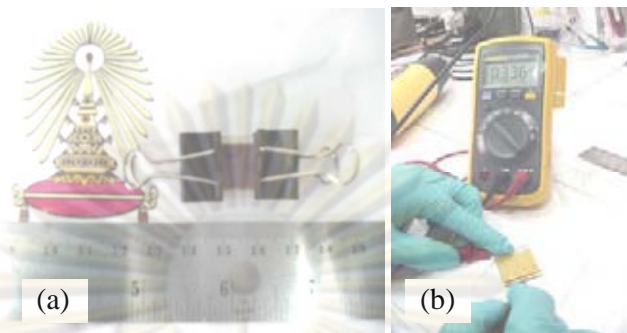
Figure 5.31: The sealing two side between the working electrode and the platinum (Pt) counter electrode by EVA or SX711-60PF.

5.6.3 Sealing two side between the working electrode and the counter electrode

Figure 5.31 shows two sides sealing between the working electrodes composed of N719 dye in the TiO$_2$ layer and the Pt counter electrode. The complete fabrication of dye-sensitized solar cells is shown in Fig. 5.31. Finally, the cell response to the light is checked by using voltmeter as shown in Fig. 5.31 (b).

5.7 The Efficiency of Dye-sensitized Solar Cells by *I-V* Curve Characterization

5.7.1 The choice of transparence conductive oxide (TCO), ZnO(Al), indium tin-oxide (ITO) and FTO electrode

Figure 5.32 shows the *I-V* curve characteristic of the DSSC001, DSSC003 and DSSC005 cells. Their short circuit current density (J_{sc}) are 0.063, 0.079 and 0.095 mA/cm^2, respectively. Due to the very thin thickness of the TiO$_2$ layer, their values are quite low. However, the cells prepared from the FTO substrate can generate the current more than ITO and ZnO(Al) substrates. FTO and ITO substrates as shown in Figs. 5.33 (a) and (c) exhibit large grain size which effect the current generation of the cells. The DSSC002, DSSC004 and DSSC006 cells have the increased value of the short circuit current density (J_{sc}) of approximately 0.155, 0.240 and 0.26 mA/cm^2 due to the increased TiO$_2$ layer thickness as shown in Table. 5.1.
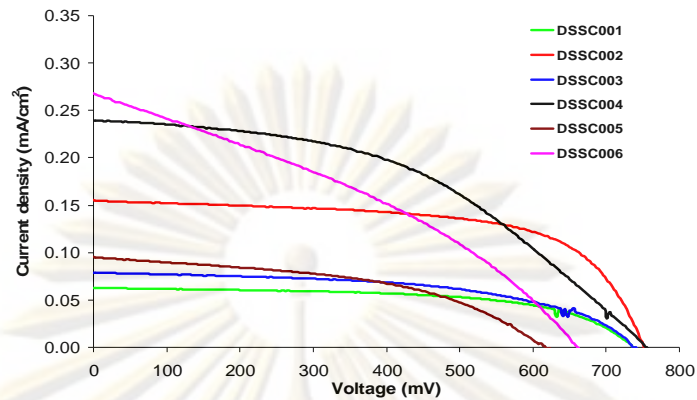
Figure 5.32: The photocurrent-voltage curve of the dye-sensitized solar cells.

The open-circuit voltage (V_{oc}) varies from 617 mV to 755 mV and a Fill Factor (*FF*) varies from 0.46 to 0.63. The cells grown on ITO and FTO substrate show the cell efficiency (η) about 0.083% and 0.084%, respectively.

Table 5.1: The solar cell parameters of the efficiency for the electrode choices.

Sample	Electrodes	Area (cm^2)	J_{sc} (mA/cm^2)	V_{oc} (mV)	*FF*	η (%)
DSSC001	ZnO(Al)	2.25	0.063	737	0.59	0.027
DSSC002	ZnO(Al)	2.25	0.155	755	0.63	0.073
DSSC003	ITO	2.25	0.079	737	0.53	0.030
DSSC004	ITO	2.25	0.240	755	0.46	0.083
DSSC005	FTO	2.25	0.095	617	0.46	0.026
DSSC006	FTO	2.25	0.266	659	0.48	0.084
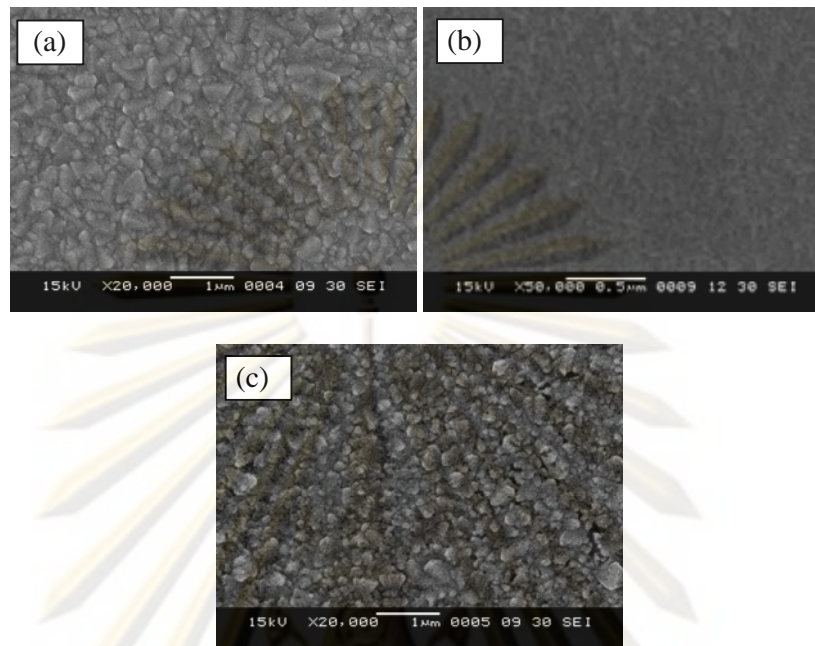
Figure 5.33: SEM image of surface (a) Indium tin oxide (ITO), (b) ZnO(Al) and (c)
FTO electrodes deposited on SLG substrate by sputtering technique.

5.7.2 The TiO$_2$-blocking-layer impact the efficiency of DSSCs

The solar cell parameter of the DSSC007 cell was achieved with the short circuit current density (J_{sc}) of approximately 0.083 mA/cm^2 as shown in Table 5.2. The efficiency of the DSSC007 cell was achieved higher than the other cells due to the thin TiO$_2$-blocking-layer. The TiO$_2$-blocking-layer plays an important role in protecting short circuit cells. However, the thickness of the TiO$_2$-blocking-layer increase or non- TiO$_2$-blocking-layer such as the DSSC008, DSSC009, DSSC010, DSSC011 and DSSC012 cells was achieved with a low Fill Factor (*FF*) and the less current generation as shown in Fig. 5.34 and Table 5.2. So, increasing of the thickness of the TiO$_2$-blocking-layer affected the high series resistance (R_s) which is not suitable for fabrication of the dye-sensitized solar cells.
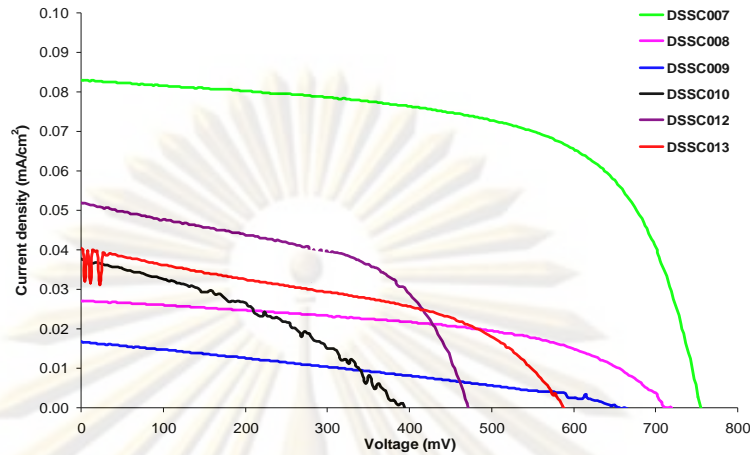
Figure 5.34: The photocurrent-voltage curve of the dye-sensitized solar cells.

Table 5.2: Effect of the blocking layer to the solar parameters of the efficiency of dye-sensitized solar cells.

Sample	Thickness of blocking layer (nm)	Area (cm^2)	J_{sc} (mA/cm^2)	V_{oc} (mV)	FF	η (%)
DSSC007	25	2.25	0.083	755	0.64	0.040
DSSC008	50	2.25	0.027	713	0.51	0.009
DSSC009	100	2.25	0.040	656	0.29	0.007
DSSC010	50	2.25	0.038	392	0.38	0.005
DSSC011	-	2.25	0.052	473	0.52	0.012
DSSC012	-	2.25	0.039	587	0.44	0.010

5.7.3 The thickness of TiO_2 layer impact on the efficiency of DSSCs

The discrepant concentration of the colloidal TiO_2 solution (10%by wt. and 1%by wt.), shows in the Table 4.5, was used to prepare TiO_2 layer. Figure 5.35 shows that the efficiency of the DSSC013 and DSSC014 cells is similar from the *I-V* curve characteristic observation. So, the concentration of the colloidal TiO_2 solution is not significant to the physical properties of the TiO_2 layer.
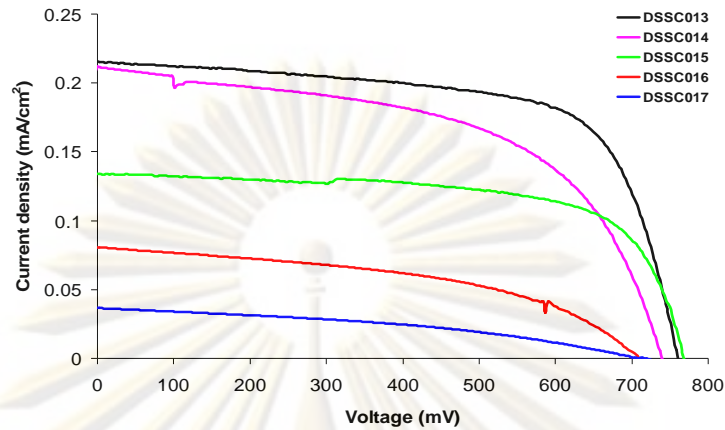
Figure 5.35: The photocurrent-voltage curve of the dye-sensitized solar cells.

Therefore, increasing the thickness of the TiO_2 layer such as the DSSC013 and DSSC014 can be achieved the higher efficiencies than the other cells as shown in the Table 5.3.

Table 5.3: Effect of the thickness of TiO_2 layer to the solar parameters of the efficiency of dye-sensitized solar cells

Sample	Thickness of TiO_2 layer (µm)	Active area (cm^2)	J_{sc} (mA/cm^2)	V_{oc} (mV)	*FF*	η (%)
DSSC013	8	2.25	0.220	761	0.67	0.112
DSSC014	8	2.25	0.211	740	0.59	0.092
DSSC015	5	2.25	0.134	770	0.67	0.069
DSSC016	2	2.25	0.080	713	0.46	0.026
DSSC017	1	2.25	0.036	719	0.38	0.010
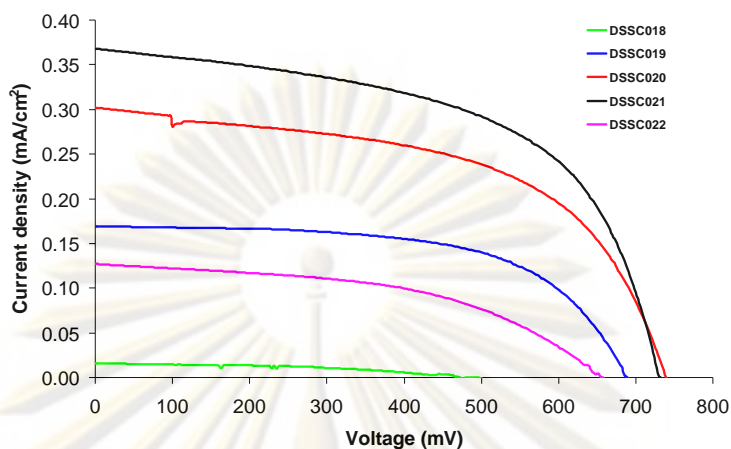
Figure 5.36: The I-V curve of the dye-sensitized solar cells.

Table 5.4: Effect of type of TiO$_2$ powder to the solar parameters of the efficiency of the dye-sensitized solar cells

Sample	Type of TiO$_2$ powder	Active area (cm^2)	J_{sc} (mA/cm^2)	V_{oc} (mV)	FF	η (%)
DSSC018	Alfa Aesar, 32 nm (8 μm)	0.70	0.016	496	0.46	0.004
DSSC019	Alfa Aesar, 5 nm (8 μm)	0.70	0.170	688	0.71	0.083
DSSC020	Degussa P25 (8 μm)	0.70	0.302	739	0.59	0.131
DSSC021	Degussa P25 (13 μm)	0.70	0.368	730	0.59	0.158
DSSC022	Degussa P25 (20 μm)	0.70	0.127	658	0.49	0.041

5.7.4 Type of TiO$_2$ powder between Alfa Aesar and Degussa P25

Starting materials in preparation process of the TiO$_2$ layer for the dye-sensitized solar cells (DSSCs) between the TiO$_2$ powder purity 99.9% (Alfa Aesar, particle size 5 and 32 nm) and Degussa P25 are compared. The solar cell parameters of the DSSC018, DSSC019 and DSSC020 cells are shown in Table 5.4. The size of

TiO_2 particle affects the efficiency of cells as the I-V curve shown in Fig. 5.36. The DSSC021 cell prepared form the TiO_2 Degussa P25 type exhibits the highest efficiency of 0.158%. The coral-reef-like cluster of the TiO_2 layer prepared by spray coating technique (using Degussa P25) is suitable for the dye-sensitized solar cells applications. In addition, the polyvinylacetate (PVA) mixed in the colloidal TiO_2 solution help binder of the TiO_2 clusters. However, the increase of the thickness of TiO_2 layer (the DSSC022 cell) (beyond some limit) leads to the lower efficiency of the cell. This is due to the short lifetime of electrons. Thus, the TiO_2 layer prepared from the TiO_2 Degussa P25 type leads to the large surface area which is useful for the dye-sensitized solar cells applications.

CHAPTER VI

CONCLUSIONS

Many parameters including: (i) the preparation of the TiO_2 absorber layer by spray coating and sputtering techniques, (ii) effects of the ZnO(Al), ITO and FTO substrates, (iii) effects of the TiO_2-blocking-layer and (iv) the type of TiO_2 powder affect the efficiencies of dye-sensitized solar cells.

I compare the TiO_2 preparation consisting of spray coating and sputtering techniques. Advantages of spray coating technique are: (1) thickness, (2) uniform of TiO_2 cluster can be controlled and (3) save more TiO_2 material. Furthermore, everybody having no knowledge about DSSCs can fabricate the good DSSCs. Then, the obtained TiO_2 layer with the good physical properties is suitable for DSSCs fabrication. The sputtered TiO_2 layer with closely packed particles leads to the less surface area. So, the suitable technique is spray coating.

Then, the conditions are varied as following: (i) the choices ZnO(Al), ITO and FTO electrodes, (ii) the TiO_2 layer deposited on TiO_2-blocking-layer and non TiO_2-blocking-layer substrate, (iii) optimal thickness of the TiO_2 layer and (iv) concentration of the colloidal TiO_2 solution (1% and 10% by wt.) and type of TiO_2 powder (Purity 99.9%, particle size 32, 5 nm and Degussa P25). The first part, the ZnO(Al), ITO and FTO electrode effect to the efficiency (η) of solar cells. The cells prepared from the FTO substrate can generate the current more than those prepared from ITO and ZnO(Al) substrates. FTO and ITO substrates exhibit large grain size which effects the current generation of the cells. However, the ZnO(Al) electrode is the good electrode due to the low resistivity which is useful for DSSCs applications. The second part, the TiO_2-blocking-layer deposited on the ZnO(Al) film by sputtering technique plays an important role in preventing the short circuit of the DSSCs. The series resistance (R_s) of cell increases with the increase of TiO_2 layer thickness. So, increasing of the thickness of the TiO_2-blocking-layer affected the high series resistance (R_s) which is not suitable for fabrication of the DSSCs. As a result, optimal

thickness of the TiO_2-blocking-layer is about 25 nm. Morphology of the TiO_2-blocking-layer is a round shape. This layer protects the short circuit in the cell. The third part, optimal thickness of the TiO_2 layer prepared from spray coating technique can be analyzed by I-V characteristic. The optimal thickness of TiO_2 layer of about 13 µm prepared from Degussa P25 TiO_2 type was achieved the highest efficiency. These can be specified by the following parameters: (i) the short circuit current density (J_{sc}) of 0.368 mA/cm^2, (ii) the open-circuit voltage (V_{oc}) of 730 mV, (iii) a fill factor (FF) of 0.59 and (iv) efficiency (η) about 0.158%. However, increasing of the thickness (more than 20 µm) such as the DSSC020 cell affects the decreasing of the efficiency since the electric filed intensity between two side electrodes is decreasing. Finally, different starting materials, the DSSC018 and DSSC020 cells, with the same thickness show the difference parameters: (i) the circuit current density (J_{sc}) of 0.016 and 0.302 mA/cm^2, (ii) the open-circuit voltage (V_{oc}) of 496 and 739 mV, (iii) a fill factor (FF) of 0.46 and 0.59 and (iv) efficiency (η) of 0.004 and 0.131%, respectively. The large surface area of the TiO_2 layer can be obtained using the TiO_2 Degussa P25 powder. The particle cluster is similar to coral reef which corresponds to a lot of nanoporous on the surface. As a result, it is useful for the dye-sensitized solar cells applications. The efficiencies of DSSCs of my work are concluded in Table 6.1.

Table 6.1 Summary of the efficiency of the dye-sensitized solar cells.

Condition	J_{sc} (mA/cm^2)	V_{oc} (mV)	*FF*	η (%)
Purity 99.9%, Alfa Aesar 32 nm Concentration 10% by wt. (1 μm thick) The ZnO(Al) electrode Thickness of blocking layer 25 nm	0.083	755	0.64	0.040
Purity 99.9%, Alfa Aesar 5 nm Concentration 10% by wt. (3 μm thick) The ITO and FTO electrodes Thickness of blocking layer 25 nm	0.240, 0.266	755, 659	0.46, 0.48	0.083, 0.084
Purity 99.9%, Alfa Aesar 5 nm Concentration 10% by wt. (8 μm thick) The ZnO(Al) electrode Thickness of blocking layer 25 nm	0.220	761	0.67	0.112
Purity 99.9%, Alfa Aesar 5 nm Concentration 1% by wt. (8 μm thick) The ZnO(Al) electrode Thickness of blocking layer 25 nm	0.211	740	0.59	0.092
Purity 99.9%, Alfa Aesar 32 nm Concentration 1% by wt. (8 μm thick) The ZnO(Al) electrode Thickness of blocking layer 25 nm	0.016	496	0.46	0.004
Purity 99.9%, Alfa Aesar 5 nm Concentration 1% by wt. (8 μm thick) The ZnO(Al) electrode Thickness of blocking layer 25 nm	0.170	688	0.71	0.083
Degussa P25 Concentration 1% by wt. (8 μm thick) The ZnO(Al) electrode Thickness of blocking layer 25 nm	0.302	739	0.59	0.131
Degussa P25 Concentration 1% by wt. (13 μm thick) The ZnO(Al) electrode Thickness of blocking layer 25 nm	0.368	730	0.59	0.158

References

[1]   Hagfeldt, A., and others. Verification of high efficiencies for the Grätzel-cell. A 7% efficient solar cell based on dye-sensitized colloidal TiO$_2$ films. *Solar Energy Materials and Solar Cells* 31 (July 1994): 481-488.

[2]   Tributsch, H. ,and Willig, F. Rate Constants of Interfacial Electron Transfer Reaction: Current Flow in nm-structured TiO$_2$ Electrode. *Solar Energy Materials and Solar Cells* 38 (August 1995): 355 – 366.

[3]   O'Regan, B. ,and Grätzel, M. The photoelectrochemical properties of Nb doped TiO$_2$ semiconducting ceramic membrane. *Journal of Electroanalytical Chemistry* 309 (July 1991): 91-101.

[4]   Nazeeruddin, K. ,and others. Synthesis and photophysical characterization of highly luminescent complexes of Ru(II) containing 4,4′-di-(*p*-carboxyphenyl)-2,2′-bipyridine. *Inorganica Chimica Acta* 198-200 (August – October 1992): 831 -839.

[5]   Nazeeruddin, K., Klein, C., Liska, P. and Grätzel, M. Synthesis of novel ruthenium sensitizers and their application in dye-sensitized solar cells. *Coordination Chemistry Reviews* 249 (February 2005): 1460 – 1467.

[6]   Nazeerunddin, K., and Grätzel, M. Separation of linkage isomers of trithiocyanato (4,4_,4__-tricarboxy-2,2_,6,2__-terpyridine) ruthenium(II) by pH-titration method and their application in nanocrystalline TiO$_2$-based solar cells. *Journal of Photochemistry and Photobiology A: Chemistry* 145 (July 2001): 79 – 86.

[7]   Wirat Jarernboon, *Fabrication of Nano-TiO$_2$ Based Liquid and Solid State Nanocrystalline Dye-sensitized solar cells,* Thesis, Department of Physics Faculty of Science Khon Kean University, 2009.

[8]   Nozik, A. Quantum Structured Solar Cells. *Nanostructured Materials for Solar Energy Conversion* (October 2006): 485 – 516.

[9]   Dwayne Miller, R., McLendon, G., Nozik, A.J., Schmickler, W.,
        and Wiling, F. Surface Electron Transfer Processes. *New York: VCH
        Publishers, Inc*, 1995.

[10]   Haiying, W., Dye-sensitized solar cells. *Chemistry: The University of
        Alabama*, 2004.

[11]   Tachibana, Y., and others. High-rate deposition of SiO_2 by modulated DC
        reactive sputtering in the transition mode without a feedback system.
        Thin Solid Films 281 – 282 (August 1996): 213 – 217.

[12]   Hannappel, T., Burfeindt, B., Storck, W., and Willig, F., Dye-sensitized solar
        cells. *J. Phys. Chem*. B 101 (May 1997): 9342-9351.

[13]   Murakoshi, K., Yanagida, S., Capel, M., Castner, Jr.E., and Moskovits, M.Ed.
        Interfacial Electron Transfer Dynamics of Photosensitized Zinc Oxide
        Nanoclusters. *American Chemical Society*. pp.221-238. Washington
        DC, 1997.

[14]   Kohjiro, H., and Hironori, A. Dye-sensitized solar cells. Handbook of
        Photovoltaic Science and Engineering. John Willey & Sons, 2003.

[15]   Rutheniumdyes/ruthenium535bis TBA. [online] (2010). Available from:
        http://www.solaronix.com/products/rutheniumdyes/ruthenium535bistb
        a/

[16]   Materials Science > Organic and Printed Electronics > Ruthenium-based dyes
        for Dye Solar Cells. [online] (2010). Available from: http://www.
        sigmaaldrich.com/materials-science/organic-electronics/dye-solar-
        cells.html

[17]   Huibers, P. and Shah, D. Multispectral determination of soap film
        thickness. *Langmuir* 13 (August 1997): 5995-5998.

[18]   Sze, S. M. *Semiconductor Devices Physics and Technology*. New Jersey: John
        Wiley & Son, 1985.

[19]   Pankove, J. *Optical Processes in Semiconductors*. New York: Dover
        Publications, 1971.

[20]   Schroder, D. *Semiconductor Material and Device Characterization*.
        Singapore: John Wiley & Son, 1990.

[21]   Cullity, B. *Elements of X-Ray Diffraction*. Massachusetts: Addison-Wesley
         Publishing Company, 1956.

[22]   Schweitzer J. Scanning Electron Microscope (SEM) [Online] (2006) [cited
         2009 Feb 03]. Available from:
         http://www.purdue.edu/REM/rs/sem.htm.

[23]   Panita Chinvetkitvanich. *Electrical Characterization of
         ZnO/CdS/Cu(In,Ga)Se₂ Thin Film Solar Cells*. Master's Thesis,
         Department of Physics Faculty of Science Chulalongkorn University,
         2001.
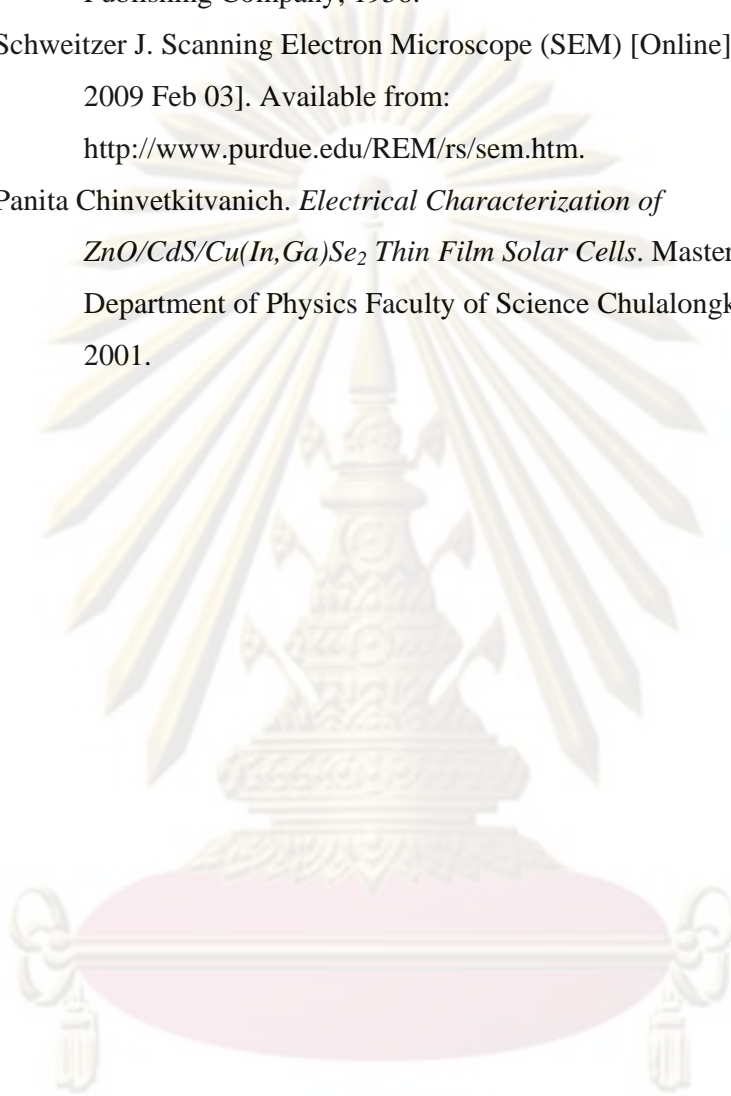
APPENDIX

APPENDIX A

Preparation of TiO$_2$ Thin Films Using Spray Coating Technique
การเตรียมฟิล์มบางไทเทเนียมไดออกไซด์โดยใช้วิธีการพ่นเคลือบ

Tanachai Ponken (ธนชัย พลเคน) *   Dr. Chanwit Chityuttakan (ดร.ชาญวิทย์ จิตยุทธการ) **
Dr. Sojiphong Chatraphorn (ดร. โสจิพงศ์ ฉัตราภรณ์) ***

ABSTRACT

TiO$_2$ thin films were prepared by spray coating technique on 3x3 cm^2 soda-lime glass (SLG) and SLG/ZnO(Al) substrates. The colloidal TiO$_2$ solution was prepared by mixing grounded TiO$_2$ powder in acetylacetone and de-ionized (DI) water. The substrates were heated up to 80°C by IR lamp and the colloidal TiO$_2$ solution was sprayed at a flow rate of approximately 3 liters/min and at a spinning speed of 1800 rpm. The optical transmission of TiO$_2$ films decreased as the spray durations increased. The sharp cut-off wavelength at approximately 375 nm (3.3 eV) was observed on the SLG/ZnO(Al) substrates corresponding to the energy gap of the ZnO(Al). The morphology of TiO$_2$ thin films have the root-mean-square roughness of approximately 10 to 12 nm. It was found that the shapes of the cluster of particles depended upon the type of substrate and substrate temperature. The films become more uniform when coating on the SLG/ZnO(Al) substrate. The surface area of the TiO$_2$ layer significantly increases owing to spherical shape of particle cluster obtained which is suitable for adsorption of dye used for solar cell applications.

บทคัดย่อ

ฟิล์มบางไทเทเนียมไดออกไซด์ถูกเตรียมด้วยเทคนิคการพ่นเคลือบลงบนแผ่นรองรับกระจกและซิงค์ออกไซด์เจือด้วยอะลูมินัมบนกระจก ขนาด 3x3 ตารางเซนติเมตร สารแขวนลอยไทเทเนียมไดออกไซด์ถูกเตรียมโดยการผสมผง ไทเทเนียมไดออกไซด์ในอะซิทิวอะซิโตนและน้ำปราศจากไอออน และทำการให้ความร้อนแก่แผ่นรองรับที่อุณหภูมิ 80 องศาเซลเซียสด้วยหลอดอินฟราเรดและพ่นเคลือบสารแขวนลอยไทเทเนียมไดออกไซด์ด้วยอัตราการไหลประมาณ 3 ลิตรต่อนาที แผ่นรองรับถูกหมุนด้วยความเร็วรอบ 1800 รอบต่อนาที จากสเปกตรัมการส่องผ่านแสงของฟิล์มบาง ไทเทเนียมไดออกไซด์จะลดลงเมื่อช่วงเวลาของการพ่นเพิ่มขึ้น และพบความยาวคลื่น cut-off ที่ประมาณ 375 นาโน เมตร (3.3 อิเลกตรอนโวลต์) บนแผ่นรองรับซิงค์ออกไซด์เจือด้วยอะลูมินัมบนกระจก ซึ่งตรงกับค่าแถบพลังงานของ ซิงค์ออกไซด์เจือด้วยอะลูมินัม ลักษณะพื้นผิวของฟิล์มบางไทเทเนียมไดออกไซด์มีความขรุขระประมาณ 10 ถึง 12 นา โนเมตร และพบว่ารูปร่างของกลุ่มอนุภาคจะขึ้นอยู่กับชนิดของแผ่นรองรับและอุณหภูมิแผ่นรองรับ ความสม่ำเสมอ ของฟิล์มที่เตรียมได้จะดีกว่าเมื่อเคลือบลงบนแผ่นรองรับซิงค์ออกไซด์เจือด้วยอะลูมินัม ด้วยความที่เป็นรูปทรงกลม ของกลุ่มอนุภาคที่เตรียมได้จะเป็นการเพิ่มพื้นที่ผิวภายในชั้นไทเทเนียมไดออกไซด์ซึ่งเหมาะสมสำหรับการดูดซับสาร สีย้อมสำหรับการประยุกต์ใช้กับเซลล์แสงอาทิตย์

Key Words : TiO$_2$, spray coating, Dye-sensitized solar cells
คำสำคัญ : ไทเนียมไดออกไซด์ การพ่นเคลือบ เซลแสงอาทิตย์ชนิดไวสีย้อม

* M.Sc. in Physics, Faculty of Science, Chulalongkorn University, Bangkok, Thailand

** Dr., Department of Physics, Faculty of Science, Chulalongkorn University, Bangkok, Thailand

*** Assis. Prof., Department of Physics, Faculty of Science, Chulalongkorn University, Bangkok, Thailand
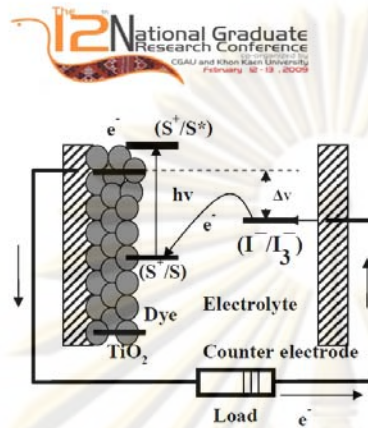
Figure 1 Principle of dye-sensitized solar cells.

Materials and Methods

1. Preparation of TiO₂ layer

The viscous colloidal TiO_2 solution was produced, as described by Nazeeruddin et al. (Nazeeruddin et al., 2004), starting from commercial TiO_2 powder (99.999% purity) consisting of weakly aggregated particles. The aggregated were dispersed into separate particles by grinding the powder (10 g) in a ball mill with a small amount of DI water (4 ml), containing acetylacetone (0.4 ml) to prevent reaggregation of the particles. The obtained viscous paste was then diluted by slow addition of DI water (96 ml) followed by continued grinding about 2 hours. Finally, a detergent (0.2 ml Trinton™ X-100) was added (Hagfeldt et al., 1994) in order to help spreading of the solution on the substrate. The colloidal TiO_2 solution was sprayed over SLG and SLG/ZnO(Al) substrates for comparisons. We note here that in our plan for DSSC structure, SLG/ZnO(Al) will be used as a substrate for TiO_2 layer since ZnO(Al) can provide good transparency as well as good electrical conduction.

PMO52-3

Subsequently, the colloidal film was annealed at 450ºC for 1 hour. The thickness of the TiO_2 layer depends on the spraying durations. In addition, with this technique, we found that the solution could be stored for over two weeks in a closed container at room temperature without any significant degradation.

2. Schematic setup of spray coating technique

A schematic of spray coating technique is shown in Fig. 2. The system consists of a nozzle gun (diameter of the aperture about 0.5 mm), a spinning substrate holder, an IR lamp, a tachometer for measuring the speed of substrate rotation, a power supply for a spinner, N_2 gas and a flow regulator. The substrate was attached on the spinning holder that can be heated to 80ºC by the IR lamp. When the surface temperature of the substrate reached the desired temperature, it was then spun at 1,800 rpm measured by the tachometer. The colloidal TiO_2 solution was loaded in a compartment of the nozzle gun. The pressure of N_2 was regulated and the flow rate was set constant and controlled by the flow meter during spraying.
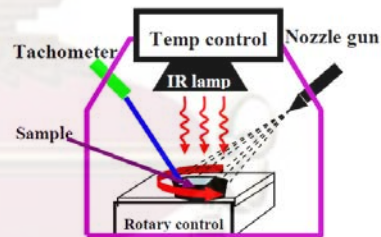

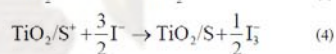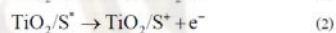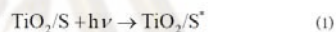Figure 2 Schematic of spray coating system.

Introduction

Dye-sensitized solar cell (DSSC) is the latest revolution in solar energy conversion device after 40 years of the invention of silicon solar cell (Papageorgiou et al., 1996). The working mechanisms of DSSC are based on photo electrochemical reactions (Smestad Greg P., 1998). The DSSCs consist of TiO_2 layer, electrolyte, dye and counter electrode. The charge carriers are separated by the electric field which builds up (without any additional doping process being necessary) at the semiconductor/electrolyte interface across the thin dye layer. The electrons are injected into the semiconductor, the ionized dye molecule is reduced by an iodine ion from the electrolyte as shown in Fig.1 (Grätzel, 2004). The best efficiencies were shown to be as high as those obtained from amorphous silicon solar cells (> 10%). The advantage of using TiO_2 is such that the nanoporousity on its surface can increase the effective surface area to about 1000 times and still shows high transparency. There were many techniques used in coating TiO_2 layer reported such as sputtering, sol-gel and screen-printing techniques. In this work, we are interesting in coating TiO_2 layers on SLG and SLG/ZnO(Al) substrates by spray coating technique because it has a potential for applications in a larger scale at lower cost. For real usage, the TiO_2 must be deposited on the transparent conducting electrode in order to transfer charges out to the external load. Here, ZnO(Al) was chosen due its excellent optical transparency as well as electrical conductivity.

Principle of Dye-sensitized solar cells

The operating principle of the DSSCs is shown in Fig. 1. Attached to the surface of the nanocrystalline TiO_2 layer is a monolayer of the charge transferring dye that they separate the function of light absorption from charge carrier transport. The injection of an electron from a photo-excited state of the sensitizer dye into the conduction band of the nanocrystalline semiconductor (TiO_2 is by far the most employed oxide semiconductor). Then, the original state of the dye is subsequently restored by electron donation from the electrolyte, usually containing redox system such as the iodide/tri-iodide couple. The regeneration of the sensitizer by the iodide intercepts the recapture of the conduction band electron by the oxidized dye. The iodide is regenerated in turn by the reduction of tri-iodide at the platinized counter electrode. Regeneration of iodide ions, which are oxidized in this reaction to tri-iodide, is achieved at a platinized counter electrode described by Eqs.(1)-(6):

$$TiO_2/S + h\nu \rightarrow TiO_2/S^* \tag{1}$$

$$TiO_2/S^* \rightarrow TiO_2/S^+ + e^- \tag{2}$$

$$TiO_2/S^+ + e^- \rightarrow TiO_2/S \tag{3}$$

$$TiO_2/S^+ + \frac{3}{2}I^- \rightarrow TiO_2/S + \frac{1}{2}I_3^- \tag{4}$$

$$\frac{1}{2}I_3^- + e^- \rightarrow \frac{3}{2}I^- \tag{5}$$

$$I_3^- + 2e^- \rightarrow 3I^- \tag{6}$$

where $h\Box$ is the photon energy and S represents the dye sensitizer.

The circuit is completed via electron migration through the external load. Overall, the device generates electric power from light without suffering any permanent chemical transformation.

The fixed parameters of the spray coating were specified with a concentration of the colloidal TiO_2 at 10% by wt., a flow rate of the colloidal TiO_2 solution at 3 liters/min and a rotation speed of the substrate at 1800 rpm while the varied parameters were the time of spraying durations at 3, 6, 9, 12, 15 and 18 seconds. The results of the TiO_2 layer obtained from the heated and non-heated substrates were compared.

Results and Discussions

1. Optical properties of TiO_2 films

The optical transmission (Perkin Elmer, Lambda 900) of the TiO_2 films grown on SLG substrates for the spraying durations of 3, 6, 9, 12, 15 and 18 seconds were found to have the transmission of light decreased when the duration times increased as expected and shown in Figs. 3 and 4 for both non-heated and heated substrates, respectively. It is worth noting that the overall transmission of TiO_2 films on the heated substrates at 80°C increase significantly as shown in Fig. 4.
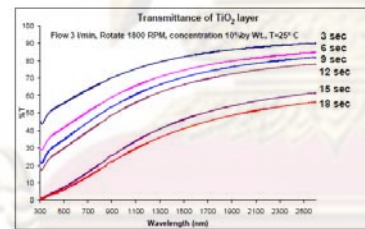

Figure 3 The optical transmission spectra of TiO_2 films on the SLG substrate for spraying durations of 3, 6, 9, 12, 15 and 18 seconds with the substrate at room temperature.
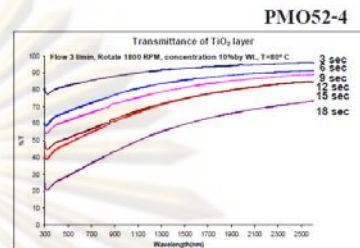
PMO52-4

Figure 4 The optical transmission spectra of TiO_2 films on SLG substrate for spraying durations of 3, 6, 9, 12, 15 and 18 seconds with the substrate at 80°C.

The optical transmission of the TiO_2 films sprayed on the SLG/ZnO(Al) substrates are shown in Fig. 5. The fringes are due the multiple reflections in the ZnO(Al) layer. It can be seen that the TiO_2 layer causes the reduction in the transmission significantly. The cut-off at 375 nm in the transmission spectrum is due to energy gap of the ZnO(Al) film (~ 3.3 eV). In addition, the dramatic reduction in the transmission at long wavelength (> 1100 nm) is solely due to the nature of the ZnO(Al).
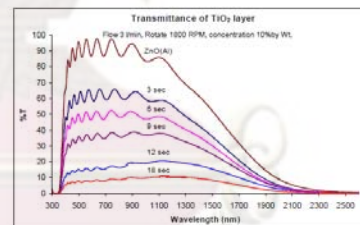

Figure 5 The optical transmission of the TiO_2 on the SLG/ZnO(Al) substrate for spraying durations of 3, 6, 9, 12, 15 and 18 seconds with the substrate at room temperature.

We note that the transmission of the TiO$_2$ films on the 80°C heated SLG/ZnO(Al) substrates increased with the similar manner to those on the 80°C heated SLG substrates.

In addition, from the optical images (Olympus, SZ61), it can be seen that the TiO$_2$ particle clustering became more uniform on SLG/ZnO(Al) substrate due to the fact that the surface of ZnO(Al) is rougher than that of the SLG as shown in Fig. 7 (a) – (d). Thus the particles are easier to stick on. In other words, the shapes of the cluster of particles depend upon the surface of the substrate.
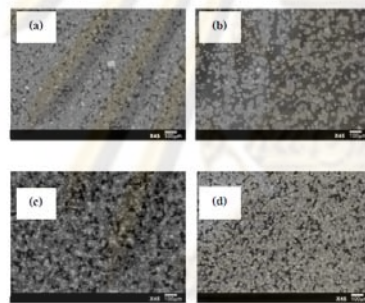

Figure 7 Optical images of TiO$_2$ film deposited on (a) SLG substrate at room temperature, (b) SLG substrate at 80°C, (c) SLG/ZnO(Al) substrate at room temperature and (d) SLG/ZnO(Al) substrate at 80°C after anneal at 450 °C for 1 hr.

2. Structural properties of TiO$_2$ films

The structural properties of the TiO$_2$ films were determined from the XRD measurements (Bruker, D8).

Figure 8 shows the XRD spectra of all TiO$_2$ films deposited by spray coating technique on the SLG and the SLG/ZnO(Al) substrates under various substrate temperatures. It can be seen from the XRD spectra that the TiO$_2$ films on the 80°C heated SLG, SLG/ZnO(Al) and non-heated SLG/ZnO(Al) substrates show better crystalline quality than that on the non-heated bare SLG substrate. A well-defined peak of TiO$_2$(101) at $2\theta=25.36°$ corresponding to the anatase phase (Yoshitak et al., 2008) and a peak of ZnO(Al) at $2\theta=34.36°$ were observed as expected. The average crystallite size obtained from the characteristic of TiO$_2$(101) peak is ~10.2 nm. The average crystallite size obtained from the TiO$_2$(101) peak is ~10 nm which was approximately the starting particle size of TiO$_2$ powder used in the experiment.
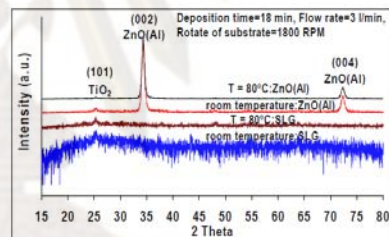

Figure 8 X-ray diffraction patterns of TiO$_2$ films deposited on SLG and SLG/ZnO(Al) substrates by spray coating technique.

3. Surface morphology of TiO$_2$ films

Figures 9 (a) and (b) compare the AFM images (Veeco Digital Instrument Dimension, 3100), (over 2

□m x 2 □m area) of the TiO$_2$ films grown on the 80ºC heated substrate and the non-heated substrate with the rms roughness of about 12 nm and 10 nm, respectively. A closely packed spherical shape of TiO$_2$ particles was observed in both heated and non-heated substrates. It suggests that packing of the particles in the microscopic scales are not significantly different. Owing to the spherical shape of the TiO$_2$ in the cluster, the surface area can be dramatically increased.
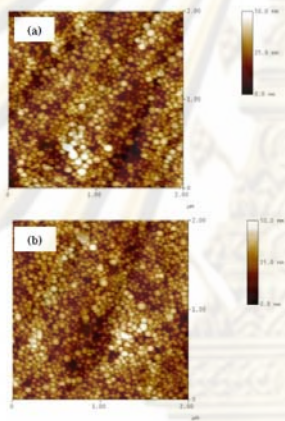

Figure 9 Surface morphology of TiO$_2$ films sprayed on SLG substrate, (a) heated up to 80ºC and (b) at room temperature.

Conclusions

TiO$_2$ films were successfully deposited on SLG and SLG/ZnO(Al) substrates by spray coating technique with both the substrates heated up to 80ºC and at room temperature. The TiO$_2$ films on the heated substrates yielded higher optical transmission than the ones on the substrates at room temperature. The TiO$_2$ films deposited on SLG/ZnO(Al) substrates showed the sharp cut-off in the transmission spectra due to energy gap of the ZnO(Al) at the wavelength of approximately 375 nm corresponding to 3.3 eV. The average crystallite size of about 10 nm was obtained and that was nearly the same as the size of the starting TiO$_2$ powder. The microscopic features of the TiO$_2$ films obtained from the AFM images were not significantly different. The TiO$_2$ films became more uniform when coating on SLG/ZnO(Al) substrate and at higher substrate temperature. Owing to the closely packed of the particle clusters with spherical shape, the surface area could be increased significantly and thus useful for DSSC applications.

References

Grätze, M. 2004. Conversion of sunlinght to electric power by nanocrystalline dye-sensitized solar cells. Journal of Photochemistry and Photobiology A: Chemistry. 164:3-14.

PMO52-7

Hagfeldt, A., Didriksson, B., Palmqvist, T., Lindström, H., Södergren, S., Rensmo H. and Lindquist, S. E. 1994. Verification of high efficiencies for the Grätzel-cell a 7% efficient solar cell based on dye-sensitized colloidal TiO₂ films. Solar Energy Materials and Solar Cells. 31:418-488.

Nazeeruddin, MdK., and Grätzel, M. 2004. Conversion and strorage of solar energy using dye-sensitized nanocrystalline TiO₂ cells. Comprehensive Coordination Chemistry II. 9.16:719-758.

Papageorgiou, N., and Grätzel, M., 1996. On the relevance of mass transport in thin layer nanocrystalline photoelectrochemical solar cells. Solar Energy Materials and Solae Cells. 44:405-438.

Smestad Greg, P. 1998. Education and solar conversion: Demonstrating electron transfer. Solar Energy Materials and Solar cells. 55:157-178.

Yoshitake, M., and Kazumi, K. 2008. Anatase TiO₂ films crystallized on SnO₂:F substrates in an aqueous solution. Thin Solid Films. 516:2547-2552.

Vitae

Mr. Tanachai Ponken was born on October 17th, 1983 in Khonkean Thailand. He received her Bachelor degree of Science in Physics from Khon Kean University in 2006.

Conference Presentations:

2008   T. Ponken, C. Chityuttakan and S. Chattraphorn., "Spray Coating of TiO$_2$ Layer for Dye-sensitized Solar Cells", 34th Congress on Science and Technology of Thailand, Queen Sirikit National Convention Center, Thailand, November 31 – December 1, (2008)

2009   T. Ponken, C. Chityuttakan and S. Chattraphorn., "Spray Coating of TiO$_2$ for Dye-sensitized Solar Cells", The 12th National Graduate Research Conference, Khon Kean University, Thailand, February 12 – 13, (2009)

2009   T. Ponken, C. Chityuttakan and S. Chattraphorn, "Spray Coating of TiO$_2$ for Dye-sensitized Solar Cells", The 4th Siam Physics Congress, Greenery Resort KhoaYai, Nakhorn Ratchasima , Thailand, March 21-22, (2009)

Permanent Address:

169/4 Dong Muang Am,

khoasounkwang, Khon Kean,

40280, Thailand.